LONDON'S GLOBAL UNIVERSITY

UCL

Time-resolved *operando* x-ray absorption spectroscopy study on dynamics of metal redox for heterogeneous catalysis

Hao Gu

[redacted]

A dissertation submitted for the degree of

Doctor of Philosophy

of

University College London

Department of Chemical Engineering

University College London

30th April, 2024

Declaration

I, Hao Gu confirm that the work presented in this thesis is my own. Where information has been derived from other sources, I confirm that this has been indicated in the thesis.

I confirm that:

1. Results and conclusions from others' published work are cited
2. Parts of this thesis have been published or submitted to open access pre-publication sources:

- **Gu H**, Yokoya T, Kang L, Marlow S, Su X, Gong M, et al. Oxygen vacancy formation as the rate-determining step in the Mars-van Krevelen mechanism. ChemRxiv. 2024; doi:10.26434/chemrxiv-2024-nbzhr This content is a preprint and has not been peer-reviewed.

- 1. Li J-Y, Lai X-M, **Gu H**, Wang C-X, Fu X-P, Wang W-W, et al. Overcoming the Strong Metal-support Interaction in Ni Clusters/TiO2 Catalyst for Selective CO2 Hydrogenation. ChemRxiv. 2023; doi:10.26434/chemrxiv-2023-bm0gl This content is a preprint and has not been peer-reviewed.

- Zhang X, Weng W, **Gu H**, et al. Versatile preparation of mesoporous single-layered transition-metal sulfide/carbon composites for enhanced sodium storage[J]. Advanced Materials, 2022, 34(2): 2104427.

- Xu K, Ma C, Yan H, **Gu H** et al. Catalytically efficient Ni-NiO x-Y2O3 interface for medium temperature water-gas shift reaction[J]. Nature Communications, 2022, 13(1): 2443.

3. All the main sources of help for this thesis have been acknowledged.

Table of content

Acknowledgements

First and foremost, I would like to give my supervisor Prof. Dr. Feng Ryan Wang my deepest appreciation for his careful guidance and encouragement, selfless dedication and help. He serves as the principal figure in directing my academic pursuits within the realm of research, providing invaluable guidance and insight that not only shapes my scholarly endeavours but also influences the trajectory of my personal journey towards self-discovery and growth.

I would like to express my sincere gratitude to all supervisors who provided invaluable guidance and support throughout my PhD studies: Prof. Andrew Beale in UCL Department of Chemistry and Prof. Matteo Salvalaglio in UCL Department of Chemical Engineering, Prof. Jianfang Wang in CUHK Department of Physics, Prof. Yuzheng Guo in Wuhan University the Institute of Technological Science and Prof. Dong Gu in Wuhan University the Institute of Advanced Studies, Prof. Zhangxiang Hao in Hubei University of Technology School of Science, Prof. Zhonghui Gao in Tianjin University School of Materials Science and Engineering, Prof. Chunjiang Jia in Shandong University. Prof. Kyung-Ryang Wee in Korea University Department of advanced Materials Chemistry.

I am deeply thankful to technicians and beam line scientists: Dr. Gabriel Karras, Dr. Stuart Barlett, Dr. Diego Gianolio, Dr. Luke Keenan, Dr. Shu Hayama, Dr. Georg Held, Dr. Matthijs Van Spronsen, Dr. Pilar Ferrer in Diamond Light Source. Mr. Kazou Kato, Mr. Misaki Katayama in SPring-8 Light Source. Dr. Tetsuo Katayama in SACLA XFEL. Dr. Sang Han Park and Dr. Soonnam Kwon in Puhang Accelerator Laboratory XFEL.

I also want to show my grateful to all my collaborators: Dr. Xin Zhang, Dr. Yuanteng, Zhang, Miss Mingyue Xie, in Wuhan University the Institute of Advanced Studies. Dr. Kai Xu, Dr. Haoxin Liu in Shandong University. Dr. Takuro Yokoya and Mr. Hirohito Hirata in Advanced Material Engineering Div. Toyota Motor Corporation. Dr. Hiroyuki Asakura in Faculty of Science and Engineering, Kindai University.

The group members of the Materials and Catalysis Laboratory at UCL Chemical Engineering: Dr. Junrun Feng in Hubei University of Technology School of Science, Dr. Lin Sheng, Dr. Yiyun Liu, Dr. Qiming Wang, Dr. Xuze Guan, Dr. Sushila Marlow, Mr. Zhipeng Wang, Mr. Lun Zhang, Miss. Manxi Gong, Miss. Yifei Ren, Miss. Zhangyi Yao, Mr. Jay Hon Cheung Yan, Mr. Xinlian Su, Mr. Daniel Wan and Mr. Guanghan Zhu, I express my gratitude for your comprehension and camaraderie, and I humbly ask for your forgiveness if there have been instances where I may have reacted abruptly towards you in a manner that was not in line with my usual demeanour.

I want to especially thank Dr. Liqun Kang and Dr. Bolun Wang in Max-Planck Institution, Dr. Ruoyu Xu in HuaWei Corporation. Thank you for your Consistently providing assistance, offering guidance, imparting pertinent knowledge and study strategies, and teaching me on the mindset of a proficient PhD student, including approaches to conducting experiments, addressing obstacles and adversities with a composed demeanour.

Last but not least, I would like to express my deepest love and appreciation to my parents Mrs. Aiwu Zhu and Mr. Zhenfeng Gu. My only and true love, my perfect wife, Mrs. Xiangrong Cai, I love you every femtosecond.

Abstract

The primary focus of traveling lies not in reaching the destination, but in appreciating the scenery encountered throughout the journey. Which is the same for the research of heterogeneous catalysis. In most of the studies on catalysts or catalysis reactions, massive efforts were made for steady-state investigation, which is like the research on starting and ending points. However, what happened during the journey actually determines catalytic pathways and catalytic kinetics which are the most important parts for understanding the mechanism of catalysis reactions. With the evolution of characterization techniques, high temporal resolution can be achieved for capturing the fast or even ultra-fast process during reactions. X-ray Absorption Spectroscopy (XAS) as its elementally selective and lenient testing requirements is becoming a crucial tool for electronic and local structure investigations. Different time resolution can be meet for different dynamics study. From half and full catalysis reaction kinetics (s), to intermediates capturing (μs to ns) and even dynamics charge transfer (ps to fs), time-resolved XAS plays an indispensable role with different experimental set-up and light source facilities.

In this thesis, techniques with time-resolved XAS are introduced including the operation mechanism and principles, experimental set-up and related researches. Brilliant studies using different temporal resolution XAS investigating different processes are also reviewed to show the importance of such characterization technique for rational designing and catalysis engineering.

There are three main projects concluded using time-resolved XAS in this thesis, studying the kinetics of half and full catalysis reaction, intermediates during metal catalysts synthesis, and dynamics of charge transfer between metals and supports. In the first project, we obtained the V_O formation and conversion kinetics by measuring the rate of the Ce^{4+} reduction and oxidation *via operando* energy dispersive Extended X-ray Absorption Fine Structure (EDE). The key findings are: 1) The rate of VO formation is 10 times faster than VO conversion; 2) VO formation rates are similar to CO oxidation rates, making it the crucial step in CO oxidation; 3) Pd and Cu act as catalysts for VO formation, enhancing its rate by 50 times at 250 °C by weakening metal-O bonding strength, resulting in reduced activation energies of 58.4 kJ/mol and 36.5 kJ/mol, respectively. Our approach to measuring and analyzing partial reaction rates during turnover is essential for chemical reactions.

The second project is encouraged by the XFEL to study the charge transfer dynamics. With soft XFEL in Pohang Accelerator Laboratory, we employ ultra-rapid X-ray Absorption Spectroscopy XAS at the Cu L3-edge and Ce M5-edge to observe changes in the electronic structure caused by the photo-induced movement of electrons between

Ce and Cu through the Ce-O-Cu bond. The time frame for this charge transfer process is approximately 200-300 femtoseconds. When comparing the time scales of intraband excitation (1-2 picoseconds) and charge transfer, only a fraction of the excited electrons migrate to Cu. Nonetheless, this minor electron migration significantly modifies the temporary electronic configuration of the Cu atoms dispersed on the surface. This alteration provides an extra catalytic push for the reactants attached to the Cu sites.

The third project focuses on presenting a combination of *in situ* X-ray absorption fine structure (XAFS) and *in situ* small angle X-ray scattering (SAXS) data during Pd nanoparticle formation to monitor chemical and physical changes simultaneously and determine intermediate Pd^0 species with a time resolution of 500 milliseconds. Distinct stages of reduction, nucleation, growth, and reoxidation were observed in the growth profile of CTAC-capped porous Pd nanospheres, with Pd^0-Cl identified as the growth species reaching peak concentrations of around 6.72 mM. Introduction of Pd seeds altered the growth dynamics, resulting in a peak Pd^0-Cl concentration of 5.73 mM without a distinct nucleation stage, showing temperature-dependent formation rates and an activation energy of 22.59 kJ/mol for Pd nucleation in a population-balanced precipitated growth model. The use of in situ XAFS and SAXS could be extended to other transition metal systems for studying growth kinetics and designing nanoparticles effectively.

Impact statement

Time-resolved X-ray absorption spectroscopy with elementally selective and ability for monitoring fast chemical processes is now becoming one of the most essential characterization techniques to study the heterogenous catalysis. The past decade witnessed the enormous development and technological evolution of synchrotron light source and experimental set-up encouraging the studies on kinetics of partial reactions and dynamics of fast chemical processes. The PhD projects are focused on the fundamental insights into time-resolved XAS and experimental study for kinetics of partial reaction, capturing intermediates and the dynamics of charge transfer process based on different temporal resolution. With these studies, insightful and inspiring understanding of elementary reactions as well as rational design can be provided. The highlights of these projects are as follows:

1. Based on the X-ray absorption spectroscopy, diverse experimental techniques for achieving different temporal resolution were demonstrated: Energy Dispersive X-ray Fine Structure Spectroscopy (EDE) with s to ms time resolution and X-ray Free Electron Laser pump probe experiments with ps to fs time resolution. These techniques not only provide the needed time scale for measuring but also encourage different physical chemistry processes studies including thermodynamics, kinetics and photo-induced electron excitation and migration.

2. The kinetics study of rate determine partial reaction for catalysis reaction based on Mar-van Krevelen mechanism is rarely mentioned within countless kinetics research. With Energy Dispersive EXAFS, the kinetics of lattice O releasing and storage can be monitored. Compared with full CO Oxidation reaction by CZ catalysts, the rate determine step is confirmed as the lattice O releasing step. And compared with pure CZ samples, metal loaded CZ was improved significantly both in catalysis properties and dynamics performance.

3. With ultra-fast XAS in XFEL, the dynamics of charge transfer in metal support interaction can be studied. The duration of the charge transfer process is around 200-300 femtoseconds, after the intraband excitation (1-2 picoseconds), resulting in a minor migration of excited electrons to Cu atoms on the surface, which alters the electronic configuration and enhances the catalytic activity of the attached reactants.、

4. Nanoparticles' crystallization and growth is the key of metal catalysts synthesis. With time-resolves XAS, the whole process from reduction of precursors,

nucleation to growth can be monitored. Pd^0-Cl as intermediate during such process was captured. The introduction of Pd seeds changed the growth dynamics, leading to a maximum Pd0-Cl concentration of 5.73 mM with no clear nucleation phase, displaying temperature-dependent rates of formation and an activation energy of 22.59 kJ/mol for Pd nucleation in a population-balanced precipitated growth model.

Chapter 1

Introduction

1.1 Research Background

Metals and metal oxides play an indispensable role as key components of heterogeneous catalysts in everyday production and life[1-3]. Metals in catalysts act as active sites in catalysis, providing adsorption sites for reactants to undergo reactions[4-7]. The redox of metals often accompanies this process, which is usually transient and can be challenging to capture in a steady-state detection environment[8-11]. Meanwhile, the synthesis of catalysts is typically associated with the redox of metals[12,13]. Precursors undergo reduction by reductants, re-oxidation by oxidising environments, calcination, and crystallisation to form new compounds. As synthetic methods and formulations continue to evolve, catalysts can be produced through complex synthetic processes[14-17]. A broad range of intermediates are produced during the synthesis process[18,19]. Capturing these intermediates, particularly the transient ones, is crucial to the design and synthesis of catalysts. Today's catalysts usually have multiple functions to deal with complex reaction conditions in real life. It is barely impossible to achieve this by single metal or metal oxide. The addition of another metal or metals to form bimetallic or polymetallic catalysts during the synthesis process is the main method of obtaining rational functionality, in which the single long-range ordered M_1-O-M_1 bond will be replaced by a M_1-O-M_2 bond[20-22]. This leads to more a complicated situation in redox reaction: electron transfer from one metal to another will significantly affect the performance of catalysts, especially the kinetics of catalysis reaction.

With the development of heterogeneous catalysts, techniques for characterising are also evolving. Synchrotron radiation facilities were built and upgraded for X-ray with higher energy and massive flux to obtain higher possibility to observe subtle changes that were previously uncharacterized. Among all the X-ray spectroscopy techniques, X-ray absorption spectroscopy (XAS) is an especially attractive spectroscopic technique as it provides a comprehensive picture of the system under investigation, providing not only the local electronic information but also the local geometry detection for target element[23-25]. With XANES providing 3D arrangement; local symmetry and electronic and magnetic structure, and EXAFS revealing coordination number of atoms per shell and the distance between shells (in most cases it can be interpreted as a bond length), XAS is know as a powerful technique for characterizing catalysts with greatest flexibility in terms of both samples themselves and measurements environment[24,26]. *Operando* or in-situ set up makes measurement under real life reaction conditions become possible[27-29]. Time-resolved XAS was developed for monitoring the selected element changing during reaction[28,30-32]. With different time resolution, different

information can be achieved for real time detection for even the simplest reaction, elementary reaction (Fig.1).

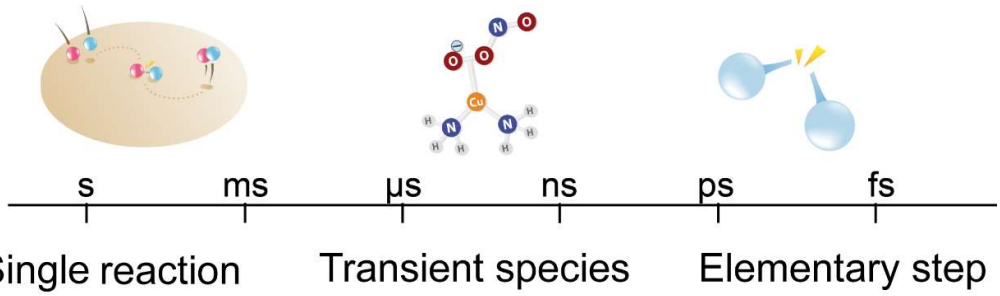

Figure 1. Different information based on different time resolution detection.

With time-resolved XAS, metal redox can be monitored simultaneously in real time, both during synthesis and during the reaction[33]. With second to milli-second Quick XAS and Energy Dispersive EXAFS (EDE), the kinetics of metal redox under *operando* environment can be studied. Transient species can be detected by micro-second to nano-second Energy Dispersive EXAFS (EDE). And recently, ultrafast XAS with X-ray Free Electron Laser (XFEL) is now the next generation of spectroscopy characterization for pico-second and even femto-second detection to reveal the real world of chemistry: dynamics of electron transfer[32-34].

1.2 Motivations and Objective

Heterogeneous catalysis plays a pivotal role in industrial processes, enabling efficient chemical transformations that are crucial to produce fuels, chemicals, and materials. This type of catalysis is essential due to its ease of separation and potential for reuse, offering significant environmental and economic benefits[19,35]. Metal redox processes are at the heart of catalytic activity, influencing both the efficiency and specificity of reactions. The oxidation state changes of metal centres in catalysts directly affect their electronic structure and, consequently, their reactivity. The most recognized model for the role of metal redox in heterogeneous catalysis is Mars-van Krevelen (MvK) mechanism, in which Metals in catalysts will react with the reactants[11]. As an example, the CO oxidation on Fe_2O_3 is described as shown in equations following:

$$CO + xFe_2O_3 \rightarrow CO_2 + xFe_2O_{(3-1)/x} \qquad 1.2.1$$

$$1/2O_2 + xFe_2O_{(3-1)/x} \rightarrow xFe_2O_3 \qquad 1.2.2$$

In this reaction, CO is oxidized by the lattice O from Fe_2O_3, which is also along with the partial reduction of Fe. With O2 adsorbed, the vacancy of O will again be refilled. Usually the first step is much slower than the second step, making the equation 1.2.1 the rate determining step. According to MvK mechanism, the metal is involved in the reaction with reduction and reoxidation. To fully understand the kinetics of similar catalysis reaction, it is mandatory to study the kinetics of metal redox in real reaction conditions. However, traditional characterization techniques often fail to capture the fast, transient changes in catalysts under real reaction conditions. This limitation hinders a deeper understanding of the fundamental mechanisms driving catalytic reactions, thus affecting the development of more effective catalysts.

The advent of operando X-ray absorption spectroscopy has revolutionized the study of catalysts by allowing scientists to observe catalysts in action, in real time, under actual working conditions. Time-resolved XAS, in particular, has emerged as a critical tool for tracking fast changes in the electronic structure and coordination environment of catalysts. This is a powerful tool for monitoring the metal redox behaviour based on MvK mechanism. Despite advancements, there remains a substantial gap in continuously tracking the dynamic redox processes of metals during catalytic reactions, particularly under industrial-relevant conditions. The reduction and re-oxidation of metals can be seen as the half reaction of the complete system. How to study them separately is challenging, especially for those under real conditions. New set-up and experiments design are needed for addressing this gap is crucial for the rational design of next-generation catalysts that are both highly active and selective.

Not only in the catalysis performance, the dynamics of metal redox and crystallization also play a decisive role in the synthesis of catalysts. For the design of high-performance materials for catalytic applications, a mechanistic understanding of metal cation reduction with controlled nanoparticle morphology is crucial. Detailed experimental evidence is needed to verify and further observe the nucleation and growth processes, in addition to the extensive theoretical literature on nanoparticle synthesis. In particular, the formation of transient species is often proposed but rarely measured experimentally. This short-life transient intermediates will need high time resolution techniques to capture, and it is better element selective.

Time-resolved XAS now for catalysis research is well built and developed. However, its temporal resolution only reaches up to the ns scale, which is sufficient for the capture of elemental changes and intermediates, but higher time resolution is needed to study the electron migration processes involved. The essence of a chemical reaction is the creation and breaking of chemical bonds, in which the process of electron migration is the physical kernel of the chemical phenomenon. X-ray Free Electron Laser is now the newest generation of synchrotron light source for ultra-fast dynamics study. With this, XAS with fs resolution can be measured for studying the catalysts.

As a conclusion, from synthesis to catalysis reaction, from chemical reaction to physical insights, time-resolved XAS can be used to reveal the relationships between time and catalytic performance for catalysts with different time resolution. This study will focus on several key catalytic systems where metal redox plays a crucial role. By applying time-resolved operando XAS, the research aims to provide unprecedented insights into the rapid changes in metal oxidation states during catalytic reactions, detailing the kinetics and mechanisms involved. Through detailed spectroscopy analysis, the study will link observable changes in metal sites to variations in catalytic activity and selectivity. This correlation will help in understanding how subtle changes in metal oxidation states affect overall catalytic processes, enabling the tuning of catalyst properties for desired reactions. Using the data obtained from time-resolved operando XAS studies, the study will construct a predictive model of metal redox dynamics. This model will incorporate various factors influencing catalytic activity and will be designed to help in predicting outcomes based on metal site characteristics and reaction conditions.

1.3 Report Outline

This graduation thesis is focused on operando time-resolved XAS study for dynamics of metal redox in heterogeneous catalysis. It starts with a brief introduction of the research background and the motivation of this work. Objective is also included in Chapter 1 to show what have done by this work. Followed by the first part, Chapter 2 reviewed existing research on time-resolved XAS on relevant research with a general introduction of synchrotron light source and X-ray spectroscopies, as well as the XFEL. Chapter 3 presents the Kinetics of oxygen release from Mars-van Krevelen mechanism for Ce based catalysts via operando energy dispersive X-ray spectroscopy. After that, in-situ XAFS observation of transient ligand-coordinated Pd^0 complex for Pd nucleation is discussed in Chapter 4. Chapter 5 contains ultra time-resolved XAS study for electron transfer between metal and support by shared O in Cu-CeO_2 catalysts. At

last, Chapter 6 concludes the remarks of all researches and gives further potentials of dynamics study with time-resolved X-ray spectroscopy for heterogeneous catalysis.

1.4 references

1 Noyori, R. Synthesizing our future. *Nature chemistry* **1**, 5-6 (2009).

2 Trost, B. M. The atom economy—a search for synthetic efficiency. *Science* **254**, 1471-1477 (1991).

3 Ertl, G., Knözinger, H. & Weitkamp, J. *Handbook of heterogeneous catalysis*. Vol. 2 (VCH Weinheim, 1997).

4 Tauster, S., Fung, S., Baker, R. & Horsley, J. Strong interactions in supported-metal catalysts. *Science* **211**, 1121-1125 (1981).

5 Auer, E., Freund, A., Pietsch, J. & Tacke, T. Carbons as supports for industrial precious metal catalysts. *Applied Catalysis A: General* **173**, 259-271 (1998).

6 Liu, L. & Corma, A. Metal catalysts for heterogeneous catalysis: from single atoms to nanoclusters and nanoparticles. *Chemical reviews* **118**, 4981-5079 (2018).

7 Boudart, M. Heterogeneous catalysis by metals. *Journal of molecular catalysis* **30**, 27-38 (1985).

8 Praneeth, V. K., Ringenberg, M. R. & Ward, T. R. Redox-active ligands in catalysis. *Angewandte Chemie International Edition* **51**, 10228-10234 (2012).

9 Yu, K., Lou, L. L., Liu, S. & Zhou, W. Asymmetric oxygen vacancies: the intrinsic redox active sites in metal oxide catalysts. *Advanced Science* **7**, 1901970 (2020).

10 Yamazaki, S., Matsui, T., Ohashi, T. & Arita, Y. Defect structures in doped CeO2 studied by using XAFS spectrometry. *Solid State Ionics* **136**, 913-920 (2000).

11 Mars, P. & Van Krevelen, D. W. Oxidations carried out by means of vanadium oxide catalysts. *Chemical Engineering Science* **3**, 41-59 (1954).

12 Gates, B. Supported metal clusters: synthesis, structure, and catalysis. *Chemical reviews* **95**, 511-522 (1995).

13 D'Souza, D. M. & Mueller, T. J. Multi-component syntheses of heterocycles by transition-metal catalysis. *Chemical Society Reviews* **36**, 1095-1108 (2007).

14 Trowbridge, A., Walton, S. M. & Gaunt, M. J. New strategies for the transition-metal catalyzed synthesis of aliphatic amines. *Chemical reviews* **120**, 2613-2692 (2020).

15 Astruc, D. Vol. 120 461-463 (ACS Publications, 2020).

16 Maurer, F. *et al.* Tracking the formation, fate and consequence for catalytic activity of Pt single sites on CeO2. *Nature Catalysis* **3**, 824-833 (2020).

17 Chen, J., Herricks, T. & Xia, Y. Polyol synthesis of platinum nanostructures: control of morphology through the manipulation of reduction kinetics. *Angewandte Chemie International Edition* **44**, 2589-2592 (2005).

18 Ji, S. *et al.* Chemical synthesis of single atomic site catalysts. *Chemical reviews* **120**, 11900-11955 (2020).

19 Fechete, I., Wang, Y. & Védrine, J. C. The past, present and future of heterogeneous catalysis. *Catalysis Today* **189**, 2-27 (2012).

20 Paier, J., Penschke, C. & Sauer, J. Oxygen defects and surface chemistry of ceria: quantum chemical studies compared to experiment. *Chemical reviews* **113**, 3949-3985 (2013).

21 Li, P., Chen, I. W. & Penner-Hahn, J. E. Effect of dopants on zirconia stabilization—an x-ray absorption study: II, tetravalent dopants. *Journal of the American Ceramic Society* **77**, 1281-1288 (1994).

22 Li, G., Blake, G. R. & Palstra, T. T. Vacancies in functional materials for clean energy storage and harvesting: the perfect imperfection. *Chemical Society Reviews* **46**, 1693-1706 (2017).

23 Zimmermann, P. *et al.* Modern X-ray spectroscopy: XAS and XES in the laboratory. *Coordination Chemistry Reviews* **423**, 213466 (2020).

24 Cutsail Iii, G. E. & DeBeer, S. Challenges and Opportunities for Applications of Advanced X-ray Spectroscopy in Catalysis Research. *ACS Catalysis* **12**, 5864-5886 (2022). https://doi.org:10.1021/acscatal.2c01016

25 Karim, A. M. *et al.* Synthesis of 1 nm Pd Nanoparticles in a Microfluidic Reactor: Insights from in Situ X-ray Absorption Fine Structure Spectroscopy and Small-Angle X-ray Scattering. *The Journal of Physical Chemistry C* **119**, 13257-13267 (2015). https://doi.org:10.1021/acs.jpcc.5b01681

26 Guo, T. More power to X-rays: New developments in X-ray spectroscopy. *LASER & PHOTONICS REVIEWS* **3**, 591-622 (2009). https://doi.org:10.1002/lpor.200810028

27 Timoshenko, J. & Roldan Cuenya, B. In situ/operando electrocatalyst characterization by X-ray absorption spectroscopy. *Chemical reviews* **121**, 882-961 (2020).

28 Lin, S.-C. *et al.* Operando time-resolved X-ray absorption spectroscopy reveals the chemical nature enabling highly selective CO2 reduction. *Nature Communications* **11**, 3525 (2020).

29 Chang, C.-J. *et al.* In situ X-ray diffraction and X-ray absorption spectroscopy of electrocatalysts for energy conversion reactions. *Journal of Materials Chemistry A* **8**, 19079-19112 (2020).

30 Hu, Y. *et al.* Tracking mechanistic pathway of photocatalytic CO2 reaction at Ni sites using operando, time-resolved spectroscopy. *Journal of the American Chemical Society* **142**, 5618-5626 (2020).

31 Chergui, M. Time-resolved X-ray spectroscopies of chemical systems: New perspectives. *Structural Dynamics* **3** (2016).

32 Budarz, J. *et al.* Time-resolved element-selective probing of charge carriers in solar materials. *Chimia* **71**, 768-768 (2017).

33 Milne, C. J., Penfold, T. J. & Chergui, M. Recent experimental and theoretical developments in time-resolved X-ray spectroscopies. *COORDINATION CHEMISTRY REVIEWS* **277**, 44-68 (2014). https://doi.org:10.1016/j.ccr.2014.02.013

34 Santomauro, F. G. *et al.* Femtosecond X-ray absorption study of electron localization in photoexcited anatase TiO2. *Scientific reports* **5**, 14834 (2015).

35 Boreskov, G. K. *Heterogeneous catalysis*. (Nova Publishers, 2003).

Chapter 2

Literature review

2.1 Synchrotron spectroscopy and time-resolved XAS

2.1.1 Synchrotron spectroscopy

The development and application of synchrotron radiation have significantly influenced the field of materials science and engineering, marking substantial advancements in understanding and analysing the properties and behaviours of various materials. The synchrotron facilities has brought about a new era in X-ray spectroscopy, providing researchers deeper insights into the structural and electronic configurations of materials under different conditions. One of the key strengths of synchrotron radiation lies in its ability to offer detailed characterizations of materials through techniques such as diffraction, scattering methods, direct imaging, and tomography[1-5]. These methods have been instrumental in advancing the field of engineering materials science, bridging fundamental research with practical applications. Furthermore, the advent of real time and real condition detection makes it possible to capture the transient changes of the materials, which is particularly important for the study of heterogeneous catalysis. The history of synchrotron radiation research facilities and insertion devices reflects a journey of continuous innovation and expansion. From the early days of realizing the potential of synchrotron light source to the development of sophisticated storage rings and insertion devices, the field has undergone tremendous growth[6,7]. This evolution has not only enhanced the capabilities of existing techniques but has also led to the emergence of new methods tailored for specific research needs and applications, illustrating the dynamic nature of the field[8]. The narrative of synchrotron radiation as a transformative tool in science and technology further unfolds with the examination of it's journey of innovation. The tale begins with its serendipitous discovery and stretches into the modern era, marked by the development of x-ray free electron lasers (XFEL)[9-11]. This progression highlights not only the technological advances but also the expanding scope of synchrotron radiation applications, from fundamental physics to research in chemistry and materials. The evolution of synchrotron light sources, characterized by the construction of third-generation synchrotron facilities around the world, underscores the global recognition of their value in pushing the boundaries of materials science. The journey of synchrotron radiation from its conceptual beginnings to a cornerstone of modern scientific research reflects a remarkable trajectory of technological and methodological advancements[2,3].

Typical synchrotron facilities has the similar construction shown in Fig 2-1. Within the light source, the electron beam generated from the electron gun undergoes acceleration through the linear accelerator (LINAC) and booster, reaching velocities close to the speed of light. Following this acceleration process, the electron beam is directed into the storage ring of the light source with the help of the injector, where it is then

organized into bunches. As the bunched beam circulates within the storage ring, the synchrotron radiation (SR) light is emitted when the beam passes through the bending magnets. Ultimately, the SR light is directed towards the beamlines, specialized areas where experiments pertaining to fundamental scientific research are carried out utilizing the synchrotron radiation. This intricate process involving electron acceleration, storage ring manipulation, and SR light emission plays a crucial role in enabling researchers to conduct a wide range of experiments and studies using the powerful SR light.

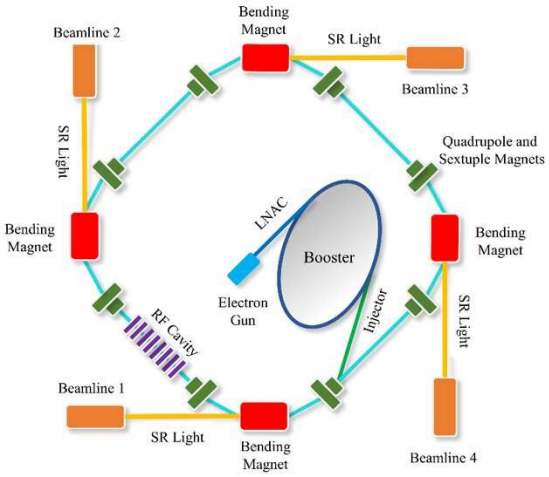

Figure 2-1. The layout of typical synchrotron radiation light source[12].

2.1.2 Time-resolved XAS

The utilization of X-ray absorption spectroscopy (XAS) has gained significant attention in recent years, especially in the field of heterogeneous catalysis. This is largely due to its ability to provide detailed insights into the structural and electronic environments of materials under investigation. A comprehensive understanding of the principles, conditions, and applications of XAS is essential for its effective use in material science research, particularly in studying the structures and mechanisms of heterogeneous catalysts. The fundamental principles of XAS, including the distinction between X-ray Absorption Near-edge Structure (XANES) and Extended X-ray Absorption Fine Structure (EXAFS), provide the basis for this technique's analytical power. Grünert and Klementiev highlight the comprehensive analytical potential derived from the physical basis of XAFS, emphasizing its role in the structural analysis of materials[13]. This foundational understanding is crucial for leveraging XAS in the exploration of complex systems, such as heterogeneous catalysts, where the technique contributes significantly to the understanding of catalytic behaviour at the atomic scale. Advancements in XAS

experimental setups, such as dedicated beamlines at synchrotron facilities, enable researchers to conduct high-quality measurements under varying conditions. The development of the beamline P65 at PETRA III, for instance, significantly improves the capacity for standard EXAFS measurements, catering to both ex-situ and in-situ investigations of materials[14]. Such facilities are instrumental in advancing the field of XAS by making it accessible and adaptable to a wide range of experimental conditions, thereby expanding its application range. In-situ and operando spectroscopy have proven to be especially valuable in the field of heterogeneous catalysis, where understanding how catalysts operate under realistic conditions is critical. A specific focus on the use of XAS in studying catalysts reveals its strength in providing detailed structural information about highly disperse and disordered systems. These capabilities are indispensable in the examination of catalysts, particularly in understanding the local environments and changes in electronic structures during catalytic reactions[13]. By applying XAS, researchers can gain invaluable insights into the mechanisms of action within heterogeneous catalysts, aiding in the refinement of catalyst designs to improve their efficiency and selectivity. Furthermore, the adaptability of XAS to specified conditions, including temperature and pressure, enables a comprehensive investigation of catalytic materials under conditions that closely mimic real-world industrial processes. This adaptability is reflected in the development of specialized reaction cells that allow for in-situ XAS and RIXS measurements under heterogeneous catalysis conditions, further expanding the possibilities of real-time monitoring and analysis of catalytic processes[15]. In conclusion, X-ray absorption spectroscopy has emerged as a potent tool in the study of heterogeneous catalysts, offering unparalleled insights into their structural and electronic properties under various conditions. The advancement in experimental techniques and the development of synchrotron facilities have significantly contributed to the utility of XAS in material science research. Through in-situ and operando studies, XAS opens new vistas for understanding the dynamic nature of catalytic reactions, guiding the design and optimization of novel catalysts with enhanced performance. The integration of XAS with other spectroscopic methods promises a more experimental understanding of materials, paving the way for the next generation of technological advancements in catalysis and beyond.

Even for most in-situ or operando XAS measurements, regardless of how close to real reactive environmental conditions, we are still testing material variations under steady-state conditions. This is due to the fact that the temporal resolution of the test is not sufficient to capture transient products or dynamic changes. Time-resolved XAS was needed to solve this problem. Weckhuysen discusses the various in-situ spectroscopic techniques, including XAS, and their role in providing real-time insights into the active sites and mechanisms of catalysis[16]. This real-time monitoring capability of XAS is

essential for revealing the dynamic processes that govern catalytic behaviour, thereby accelerating the development of more efficient and robust catalytic systems.

Previously, the predominant practice among quick-scanning beamlines involved the accumulation of a thorough extended x-ray absorption fine structure (EXAFS) spectra within a short time (from minutes to micro-seconds), accomplished through the movement of the monochromator from a low energy level to a high one, followed by the repetition of this sequential procedure (Figure 2-2 a). This process was typically completed at a rapid pace, enabling efficient data collection and analysis[17-19]. Another method for quick EXAFS is Energy Dispersive EXAFS (EDE) (Figure 2-2 b)[19,20]. The polychromatic beam is directed towards the sample and subsequently spreads out towards a position-sensitive detector where the beam's position is linked to its energy level[21]. The dispersive setup of X-ray Absorption Spectroscopy (XAS) offers two key benefits that enhance its scientific appeal. Initially, the entire x-ray absorption spectrum is captured concurrently, thereby rendering the technique particularly valuable for investigating rapid processes. Moreover, the focused beam's size at the sample location remains compact and consistent because no adjustments to optical components are needed for gathering spectral information. This feature ensures stable and precise measurements during data collection. The simultaneous collection of the complete absorption spectrum allows for a comprehensive analysis of the sample's behaviour over a wide range of energy levels. Additionally, the consistent and small size of the focused beam guarantees accurate and reproducible results, making EDE an indispensable tool in studying various materials and their properties[22]. And now with the development of newest generation of synchrotron light source, the time resolution for XAS can be extremely high. Pump probe experiments with laser pulse as pump and XFEL as probe can measure XAS with fs temporal resolution. Transient electronic structure can only be detected by this ultra-fast X-ray spectroscopy. The sources under consideration comprise a high-energy electron bunch with a magnitude in the GeV range that is introduced into a sequence of undulators spanning hundreds of meters in length. The motion of the electrons within the initial segment of the undulators leads to the emission of radiation, akin to what occurs in a 3rd-generation storage ring. Concurrently, as the radiation and electrons travel together, the radiation field undergoes amplification and the electrons commence interacting with the radiation, giving rise to the formation of a microbunch structure characterized by the wavelength of the radiation[23,24]. A visual depiction of this phenomenon can be found in Figure 2-3, illustrating the intricate dynamics at play. The said micro-bunch structure emits coherent X-ray photons, the intensity of which experiences an exponential increase through a phenomenon known as self-amplified spontaneous emission (SASE) until it reaches a point of saturation. At this stage, the system achieves a state where further amplification is no longer feasible.

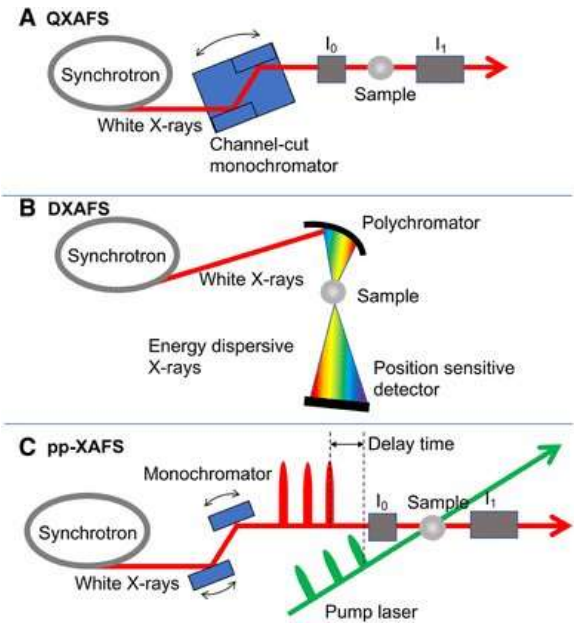

Figure 2-2 Schematic diagram of **a)** quick-XAFS (QXAFS), **b)** energy-dispersive XAFS (DXAFS), and **c)** pump–probe XAFS (pp-XAFS)[20,22].

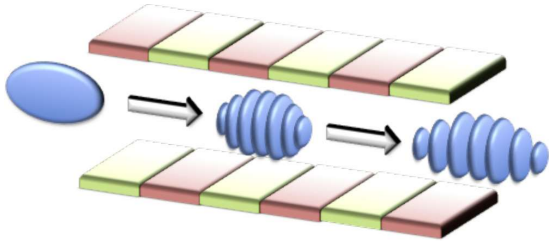

Figure 2-3 Schematic diagram of the electron bunch traverses the undulator[25]

Time-resolved XAS with temporal resolution from minutes to fs can be used to study different dynamics for different systems: from active intermediates monitoring to reaction kinetics; from the migration of lattice vacancy to electron transfer between metal and ligand. Both XANES and EXAFS can be used for better understanding the catalysts behaviour and reaction mechanism. Steady-state measurements can only show the start and the destination. Without the understanding of the dynamical processes, the pathway and intermediates will be neglected. Moreover, it is crucial to note that the ongoing developments in pump probe XAS indicate the emergence of a hierarchical structure of computational strategies aimed at addressing core hole excitations. This evolution encompasses a diverse array of methods that strike a delicate balance between precision and computational cost, thereby enabling the exploration and resolution of a broad spectrum of chemically significant issues[25,26].

2.2 XANES and time-resolved XANES characterization for heterogeneous catalysts

In previous studies, faster test speeds often meant that the signal-to-noise ratio of the spectrum was relatively poor, so in many studies researchers have usually used XANES as the main object of study. Putting focus on XANES part also enables further higher temporal resolution. X-ray absorption spectroscopy is the element selective and liberal in terms of test and sample requirements, which can be used to identify the metal speciation in environmental samples. XANES spectroscopy is also sensitive to changes in oxidation state, and in a single system, the position of the absorption edge of the XANES reflects to the change in oxidation state of the target element. Most researchers used time-resolved XANES to study the oxidation state changing under certain conditions especially *operando* conditions. In addition to these, the electronic structure also affects the XANES spectrum. With higher energy resolution, pre-edge signals, which were blurred in past tests, are now also clearly visible. Combined with the changing of white line peak and the followed oscillation, researchers using time-resolved XANES can know more about the electronic structure of the target element in their system. In this part, we will discuss the previous studies on time-resolved XANES characterization for identification of element speciation; monitoring oxidation state changing and understanding the electronic structure.

2.2.1 Identification of element speciation

Time-resolved X-ray absorption near-edge structure (XANES) represents a robust and influential technique employed for the identification of element and metal speciation within chemical systems. By examining the alterations in XANES spectra over a period, researchers can gain profound insights into a myriad of chemical processes and reactions involving an array of elements and metals. JF Gaillard [27] developed a new method with Q-XAS to investigate metal speciation in environmental materials. They were using Q-XAS with 7 seconds temporal resolution to test an environmental sample collected from the sediments of Lake DePue. The determination of the composition of mixtures was achieved through the process of spectral decomposition, which involved utilizing a quadratic linear programming (QLP) fit to analyze the XANES signals present in the samples and compare them to established standards in order to accurately identify the components within the mixtures. This methodological approach allowed for a systematic and rigorous examination of the spectroscopy data, enabling a detailed assessment of the chemical composition of the mixtures through a mathematical optimization process. The research conducted by Zitolo et al. [28] delved deeply into the exploration of catalytic sites for oxygen reduction within iron- and nitrogen-doped graphene materials through the application of XANES. The authors effectively

demonstrated the critical significance of the physico-chemical characteristics of the support material in dictating the turnover frequency of Fe-centred moieties, revealing intricate details about catalytic mechanisms. Furthermore, Bacquart et al.[29] provided a detailed account of their research on subcellular speciation analysis of trace element oxidation states using synchrotron radiation micro-XANES. This particular study placed emphasis on the remarkable spatial resolution and detection limits achieved through the utilisation of a micro-XANES setup predicated on Kirkpatrick-Baez X-ray focusing optics, underscoring the precision of the analytical approach. Furthermore, an investigation by Reitz et al. focused on the utilisation of time-resolved XANES in the examination of CuO/ZnO catalysts during methanol reforming reactions[30]. Through their research endeavours, the scholars observed the dynamic fluctuations in copper species and their catalytic activities under varying reaction conditions, thereby demonstrating the immense potential of time-resolved XANES in elucidating the intricacies of catalytic processes. Furthermore, the contribution by Shapovalova et al. delved into the domain of temperature- and time-resolved X-ray absorption near-edge spectroscopy (XANES) studies involving a novel valence tautomeric cobalt complex[31]. This research initiative exemplified the practical application of time-resolved XANES in elucidating the underlying electron transfer mechanisms within unique model systems, thereby illuminating fundamental processes at the molecular level.

Collectively, the combination of time-resolved XANES with a diverse range of experimental setups and sample systems, as exemplified in the mentioned studies, offers significant potential for advancing our understanding of element and metal speciation in a wide range of chemical and catalytic processes. This approach could facilitate enhanced scientific understanding and technological advancements in the field.

2.2.2 Monitoring of the metal oxidation state

Operando X-ray Absorption Spectroscopy (XAS) has emerged as a crucial tool for investigating the dynamic alterations in the oxidation state of metals under in situ conditions. This technique enables researchers to observe in real-time the progression of metal oxides transforming into metallic states during different catalytic reactions. The research conducted by Oezaslan et al. was studying on elucidating the process of Cu oxide transitioning to a metallic state under CO2 reduction circumstances using operando Quick-XAS[32]. Their findings illustrated the precedence of Cu oxide reduction to metallic states before the generation of hydrocarbons in the CO2 reduction process. Similarly, the exploration carried out by Kremneva et al. scrutinized the breakdown of bimetallic electrocatalysts through in situ XAS, uncovering insights into the behaviour of Pt concerning oxide creation or dissolution[33]. Additionally, the investigation by

Browne et al. examined alterations in the local structure of bimetallic Mn/Ru oxides during the oxygen evolution reaction, demonstrating the influence of Mn content on the oxidation state and coordination environment of Ru sites[34]. X-ray photochemistry revealed that the redox process of Prussian blue in paper support is controlled by the substrate content, structure, photosensitivity, and interaction with the oxygen environment. Exposure to X-ray beam led to a shift in the absorption edge towards lower energies, indicating a reduction of Fe^{3+} to Fe^{2+} in Prussian blue, accompanied by pigment discoloration[35]. Another research on Study of the redox processes involved upon cycling of the Li-rich layered oxide takes full advantage of quick-XAS. By *operando* quick-XAS, Ni, Co and Mn was measured simultaneously upon cycling[36]. Ni and Co are oxidized during the first charge, while Mn remains stable at Mn^{4+} oxidation state (Fig.2-4). Oxygen participates in redox reactions along with Ni and Co, as indicated by XANES spectra shifts and metal-oxygen distances. Mn does not significantly participate in redox processes, remaining at Mn^{4+} oxidation state. The involvement of oxygen in reversible redox reactions is crucial, with oxide ions being oxidized during the plateau and reversibly reduced in subsequent discharges.

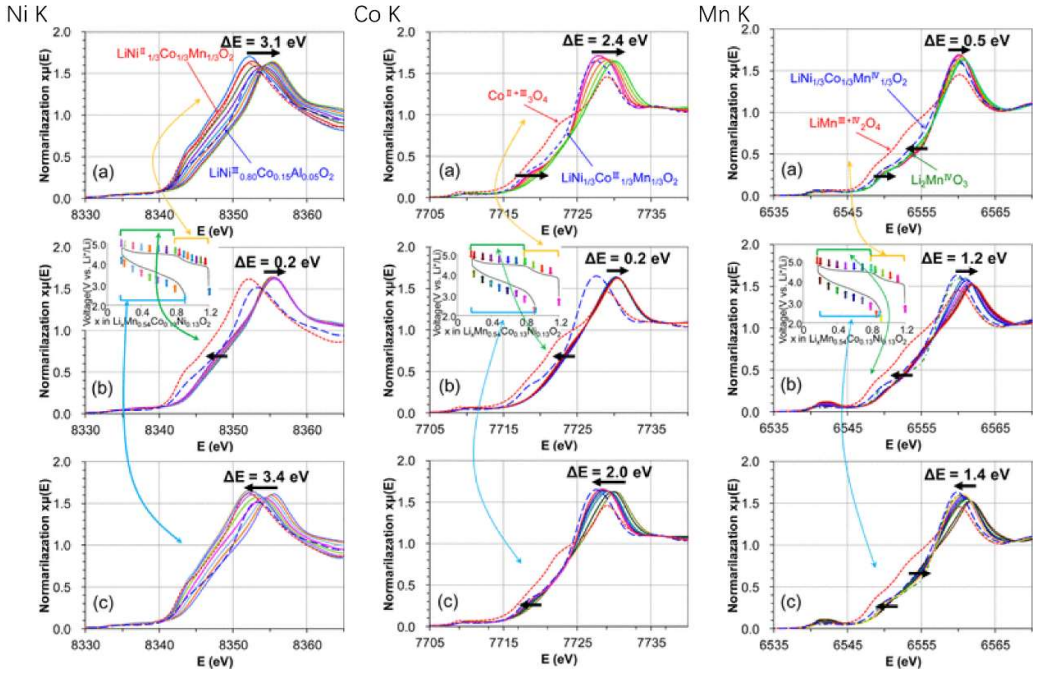

Figure 2-4. Normalized representative XANES spectra at the Ni K-edge (left), Co K-edge (middle) and Mn K-edge (right) for $Li_{1.20}Mn_{0.54}Co_{0.13}Ni_{0.13}O_2$ during the first charge before the plateau. **a).** The first charge during the plateau up to 4.8 V vs Li^+/Li. **b).** The first discharge after the plateau **c).** The spectra for $LiNi^{II}_{1/3}Co_{1/3}Mn_{1/3}O_2$ and $LiNi^{III}_{0.80}Co_{0.15}Al_{0.05}O_2$ are given as references. [36]

Liqun and Bolun were using Energy dispersive XAS to investigate the redox behaviour of CuO-CeO_2, a phenomenon is observed where there is an additional transfer of electrons from metallic copper to surface carbon species (Fig. 2-5). This observation is made possible through a combination of techniques including operando X-ray absorption spectroscopy, synchrotron X-ray powder diffraction, near ambient pressure near edge X-ray absorption fine structure spectroscopy, and diffuse reflectance infrared Fourier transform spectroscopy. A theoretical framework known as electronic metal–support–carbon interaction (EMSCI) is put forward to elucidate the mechanism by which carbon monoxide oxidation takes place[37].

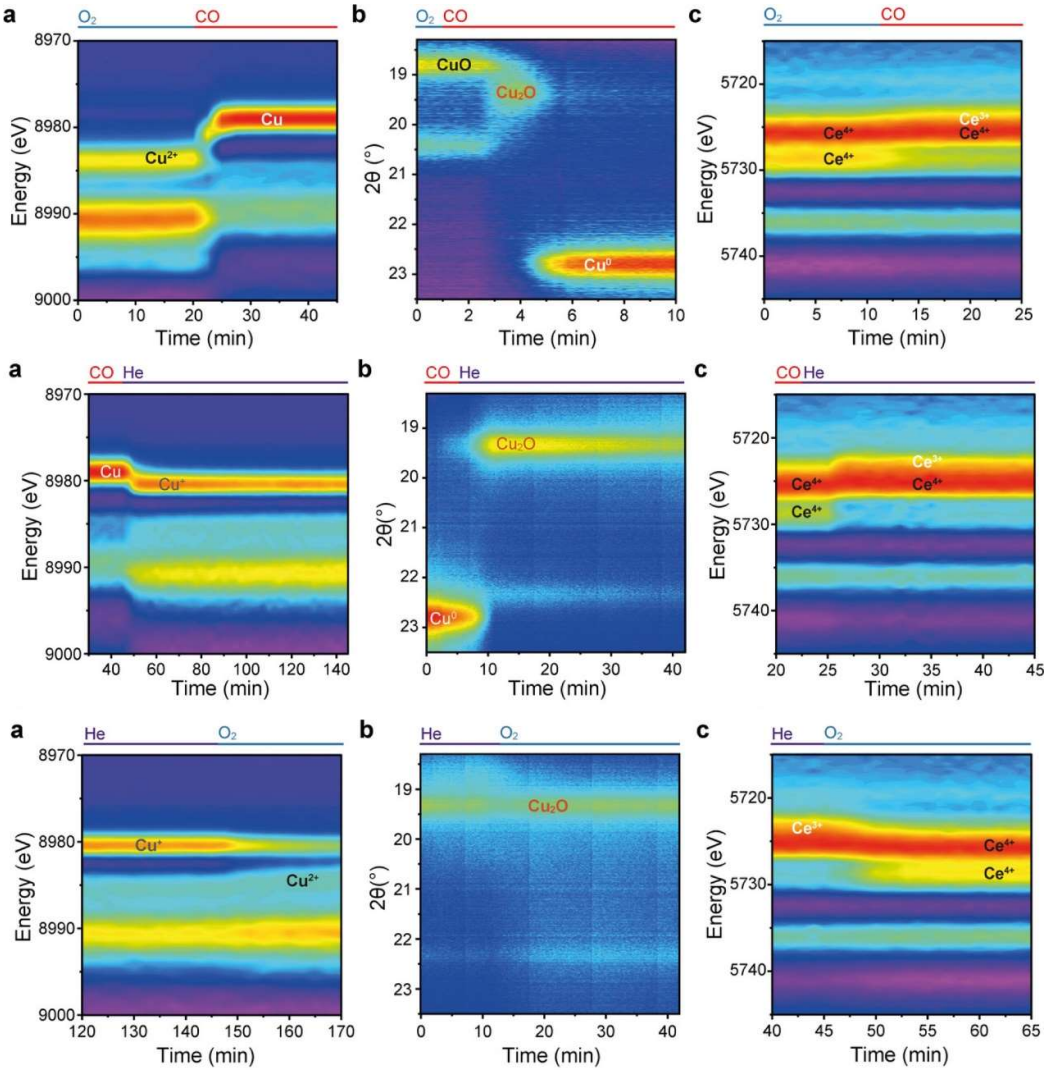

Figure 2-5. Operando characterisation of Cu, Ce and surface carbon during the reduction of CO by CuO-CeO_2 at 453 K (top), at 453 K in He (middle) and at 453 K in O_2(bottom). **a)** Contour map of the Cu K-edge first derivative XANES spectra, showing the reduction of Cu^{2+} to Cu^0. **b)** Contour

map of the SXPD patterns, showing the conversion of CuO to metallic Cu. **c)** Contour map of the Ce L_3-edge first derivative XANES spectra, showing the increase of Ce^{3+} content after reduction. [37]

Based on Safonova's research, time-resolved X-ray absorption spectroscopy offers a distinctive perspective on the mechanism of oxygen activation occurring on copper-ceria catalysts that are highly dispersed. Through the utilization of a specifically crafted non-steady-state experimental approach in combination with time-resolved XAS, a platform was established for juxtaposing the reactivity of copper and cerium atoms in the CO oxidation cycle (Fig. 2-5). The process of oxygen activation, facilitated by a strongly bound oxygen intermediate, entails the redox activity of Cu^{2+}/Cu^{+} and Ce^{4+}/Ce^{3+} couples. The kinetics of reduction of Cu^{2+} and Ce^{4+} are interconnected with the rate-determining phase of CO oxidation. The involvement of the Ce^{4+}/Ce^{3+} couple in CO oxidation is estimated to be roughly 10 times less pronounced than that of Cu^{2+}/Cu^{+} (Fig. 2-6). Nonetheless, these two metals exhibit synergistic reactivity, likely operating within the confines of the same active site. Throughout the CO oxidation progression, enduring Cu^{+} and Ce^{3+} species emerge. Despite the necessity for further elucidation regarding the genesis and reactivity of these species, our findings underscore that they do not serve as catalysts for oxygen activation, leading to the formation of strongly bound oxygen intermediates.[38]

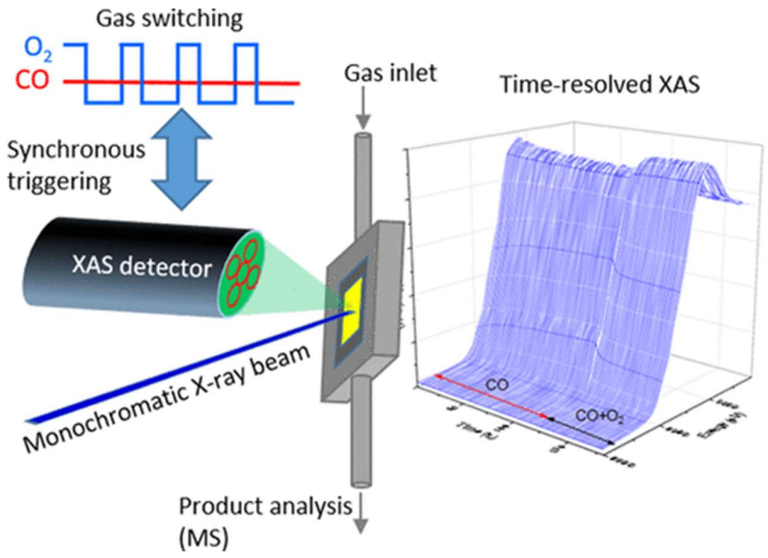

Figure 2-6. Scheme of the experimental setup for in situ/operando time-resolved XAS studies of heterogeneous catalysts in a plug-flow reactor cell.[38]

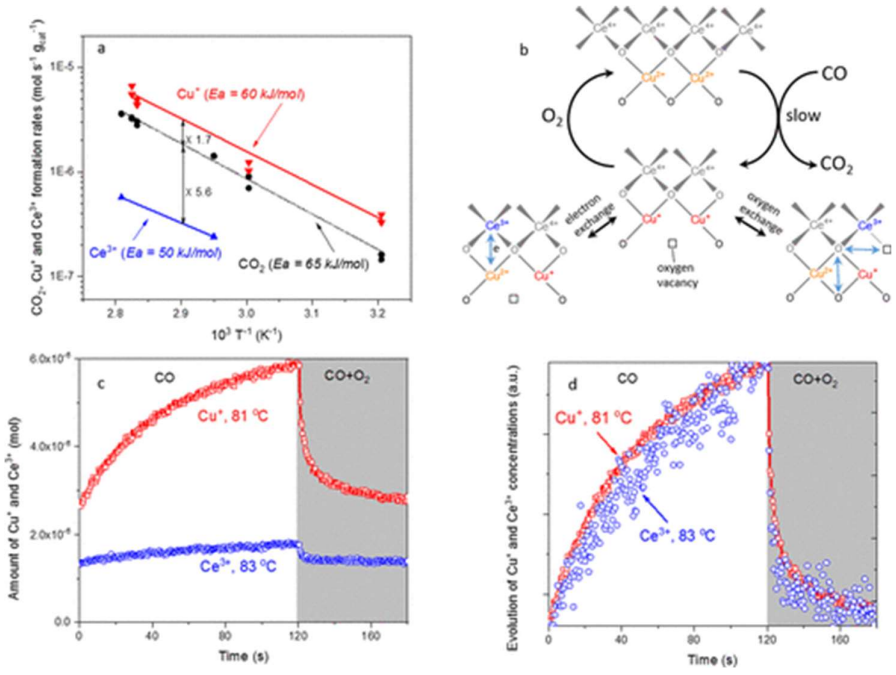

Figure 2-7. a) Comparison of the initial rates of CO_2, Cu^+, and Ce^{3+} formation in 1% CO during oxygen-cutoff experiments at different temperatures. **b)** Scheme explaining the redox activity of active sites during low-temperature CO oxidation on copper-ceria catalysts. **c)** Evolution of absolute amounts of Cu^+ and Ce^{3+} in 4 wt % Cu/CeO_2 catalyst during oxygen-cutoff experiments at similar temperatures. **d)** Evolution of Cu^+ and Ce^{3+} amounts in 4 wt % Cu/CeO_2 catalyst on relative scales. [38]

Through the application of operando XAS methodologies, researchers have unearthed intricate details regarding the redox dynamics and structural modifications of active sites in diverse catalytic systems. These studies offer crucial understandings into the mechanisms that drive catalytic reactions, thereby facilitating the rational development of enhanced catalyst materials.

2.3 Time-resolved EXAFS characterization for heterogeneous catalysts

The utilization of time-resolved Extended X-ray Absorption Fine Structure (EXAFS) analysis for the exploration of alterations in coordination environment dynamics in heterogeneous catalysts is a topic of growing interest in catalysis research. Heterogeneous catalysts hold a significant position in numerous industrial processes, and comprehending the fluctuations in their coordination environment under varying reaction conditions is paramount for enhancing their efficacy and innovating novel catalysts. This part endeavours to encapsulate the current advancements in this domain, concentrating on recent progressions and their correlation with the examination of matel

speciation and coordination environment dynamics in heterogeneous catalysts via time-resolved EXAFS analysis.

2.3.1 Metal speciation

A seminal work in this sphere by Grunwaldt et al. discusses the appropriateness of diverse reaction cells for amalgamated catalyst characterization and time-resolved investigations, particularly utilizing X-ray Absorption Spectroscopy. This research underscores the necessity of scrutinizing the configuration of solid catalysts concurrently and at the precise site where catalytic and structural modifications transpire[39]. The article delineates the trade-off between the spectroscopic setup and the optimal blueprint for an in situ reactor cell, accentuating the possibilities and constraints of in situ and time-resolved XAS. This lays a crucial foundation for further exploration into capturing and scrutinizing the dynamic alterations in coordination environments to extract insights into catalyst behaviours. Moreover, the reactivity of binuclear tantalum clusters on silica investigated through transient time-resolved spectroscopy by Nemana, Sun, and Gates, delves into the coordination dynamics of tantalum clusters during interactions with hydrogen, deuterium, and ethylene[40]. This inquiry demonstrates how time-resolved IR and EXAFS can elucidate the alterations in coordination numbers and bonding distances, underscoring the pivotal role of EXAFS in comprehending the dynamics of active sites in catalysts. For some reasons, the coordination number and bond distance sometimes are not easy to get from EXAFS fitting based on the spectra quality. In this case, standards were used to get the linear combination fitting to have the composition of each component presenting in materials. Boland using time-resolved XAS to quantitatively analyse the rate at which ferrihydrite transforms into goethite under varying Fe^{2+} concentrations, as well as under different pH conditions[41]. They were using a solution of 1 M $FeSO_4$ and a suspension of ferrihydrite as the standard spectra to get the proportion of each components. Another research applied by Dabros also used standards for linear combination fitting for analysis of EXAFS for metal speciation[42]. With time-resolved XAS, the metal speciation can be monitored alone with the temperature raising. It can be seen in Figure. 2-8 that the oxide precursor experienced a series of chemical changes resulting in the formation of intermediate oxy-sulfide species, which served as an important transitional phase before ultimately being converted into the final sulfide form through a complex reaction process.

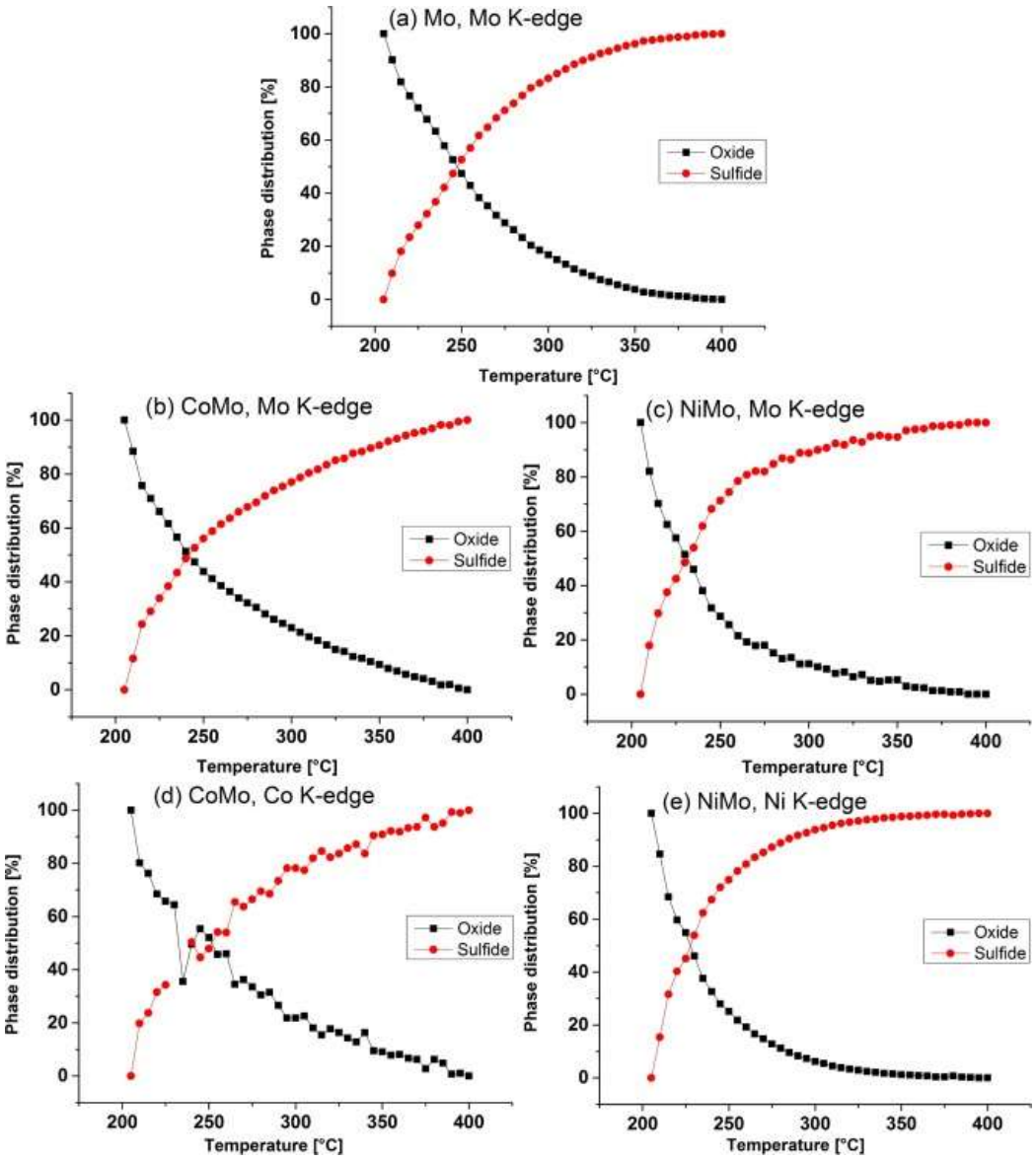

Figure 2-8. LCF analysis of fitted EXAFS spectra from in-situ sulfidation at the Mo K-edge for **a)** Mo, **b)** CoMo, **c)** NiMo, at the Co K-edge for **d)** CoMo, and at the Ni K-edge for **e)** NiMo.[42]

Combined with other characterization techniques, EXAFS can also show strong evidence of the speciation of materials. The application of MCR-ALS (Multivariate Curve Resolution with Alternating Least Squares) to time-resolved Quick-XAS spectra has provided a valuable opportunity to investigate the speciation of catalysts based on Mo–W materials supported on alumina. The research has indicated that the presence of molybdenum within the HPA tungsten framework ($SiMo_3W_9$/Al) as opposed to W_{12}/Al, promotes the sulfidation of tungsten. The findings support the notion of a simultaneous sulfidation process affecting both Mo and W elements within the $SiMo_3W_9$/Al catalyst,

leading to the creation of composite Mo-W sulfide layers. This formation has also been confirmed through HAADF imaging techniques[43].

2.3.2 Coordination environment investigation

The intricate arrangement of atoms within a material can be elucidated by meticulously analyzing the Extended X-ray Absorption Fine Structure (EXAFS) data, which involves determining the coordination numbers as well as the distances between neighboring atoms. This comprehensive analysis provides valuable insights into the coordination environment of the material under study.

Expanding upon the techniques for time-resolved EXAFS, Liang and Gates presented a striking illustration of the efficacy of time-resolved structural analysis through their exploration on rhodium clusters supported in zeolites[44]. Their research on the formation and disintegration of these clusters unveiled the dynamic nature of coordination environments affected by interactions with hydrogen and ethylene. This study epitomizes the type of revelations that can be obtained by leveraging time-resolved EXAFS to scrutinize the coordination dynamics of metal clusters in heterogeneous catalysts. A classic research on Oxygen storage materials was performed with time-resolved XASF by Takashi[45]. In his study, the dynamics of Zr-O bond formation and breaking in $Ce_2Zr_2O_8$ nanoparticles during oxygen storage/release were monitored, revealing changes in coordination O around Zr ions. In the processes of storing and releasing oxygen, the oxidation state of Ce locations undergo changes initially, followed by structural alterations taking place at Zr sites involving the formation or cleavage of Zr-O bonds (Fig. 2-5). This sequence of events highlights the dynamic interplay between Ce and Zr in facilitating the crucial oxygen storage and release mechanisms.

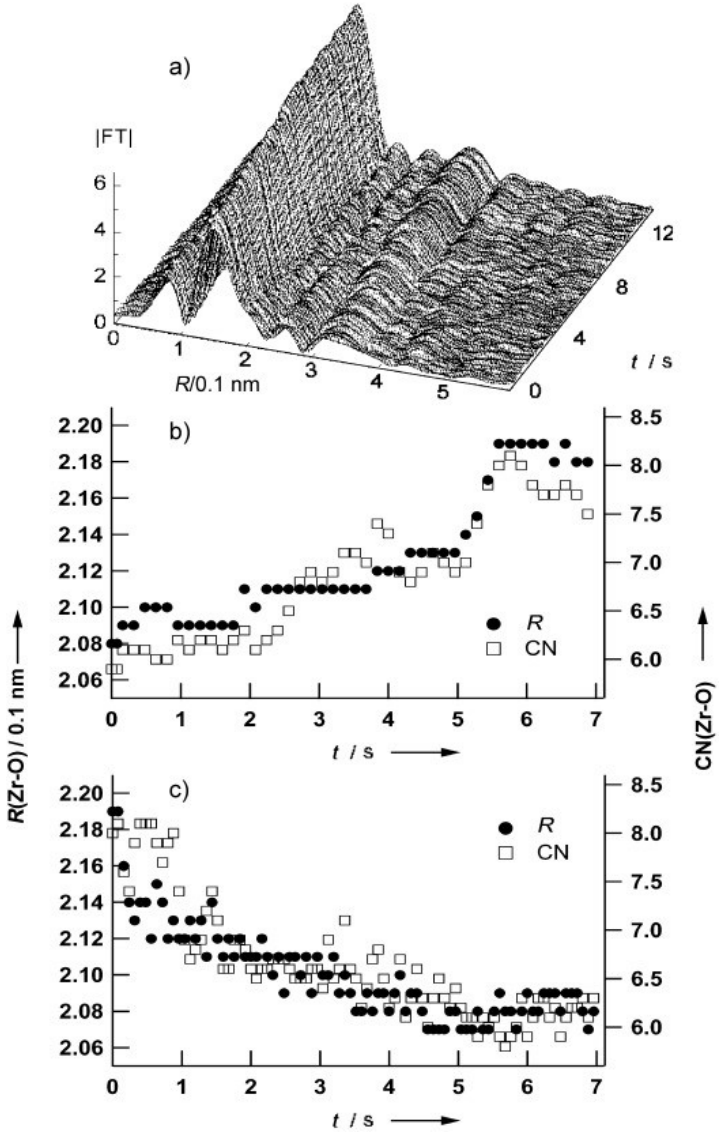

Figure 2-9. a) Serial k^3-weighted energy-dispersive EXAFS Fourier transforms at the Zr K edge for $Pt/Ce_2Zr_2O_8$ in the oxygen-release process at 773 K. **b)** and **c)** Time profiles of the coordination number (CN) and Zr-O coordination distance (R) in the oxygen-storage **b)** and -release processes **c)** at 773 K. R0.002 nm. CN0.7.[45]

Similarly, Yasutaka study the structure of $Ce_{0.5}Zr_{0.5}O_2$ as oxygen storage materials with EXAFS[46]. He found that the solid solution of $Ce_{0.5}Zr_{0.5}O_2$, which is atomically homogeneous, displayed the highest Oxygen Storage Capacity (OSC) compared to the other CeO_2–ZrO_2 samples under examination. This observation highlights the significance of achieving a high level of homogeneity in the CeO_2–ZrO_2 solid solution for maximizing OSC. Notably, the local oxygen environment surrounding the Ce and Zr atoms experienced significant alterations due to the increased homogeneity of the

solid solution. It was hypothesized that the improved homogeneity of the CeO_2–ZrO_2 solid solution and the consequent modifications in the oxygen environment are key factors contributing to the enhancement of OSC. Another Japanese researcher, Soichi tried to investigate the metal-support interaction between PtO_2 and γ-Al_2O_3 by in-situ time-resolved XAS (Fig. 2-10)[47]. In this study, they examined the dynamics behaviour associated with the development of two-dimensional low-coordinated Pt particles as a result of the reduction process of PtO_x particles by H_2 gas (Fig. 2-11). These PtO_x particles were experiencing metal-support interaction (MSI) with the γ-Al_2O_3 support material. It was observed that the PtO_x species, initially relatively stabilized, underwent reduction at temperatures below 373 K, while the PtO_x species located at the interface with the γ-Al_2O_3 surface underwent reduction at temperatures exceeding 373 K. The time-resolved Pt L3-edge X-ray absorption spectroscopy (XAS) data provided insights into the transformation of the particle morphology from three-dimensional PtO_x particles to two-dimensional low-coordinated Pt particles during the in-situ reduction process of $PtOx/Al_2O_3$ at 473 K; conversely, at 373 K, the interfacial PtOx species persisted even after reduction.

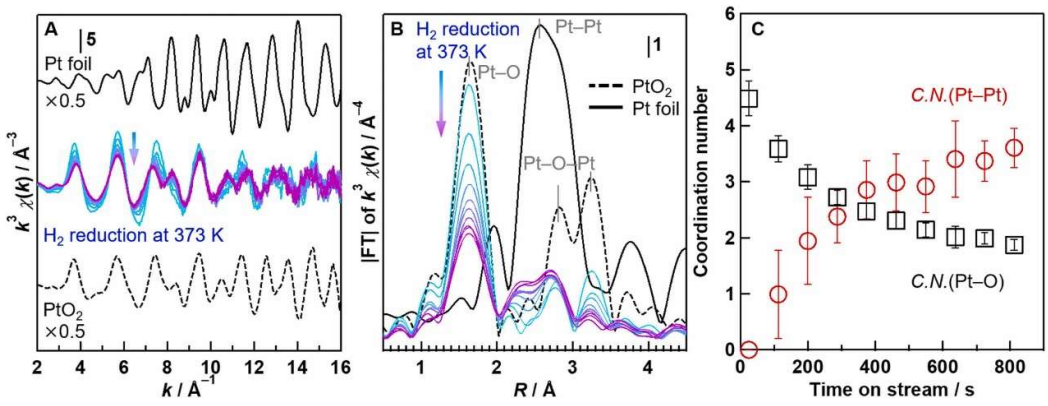

Figure 2-10. a) A series of Pt L_3-edge EXAFS oscillations of PtO_x/Al_2O_3 during in situ reduction with 500 ppm H_2/He at 373 K. Solid line; Pt L_3-edge EXAFS oscillation of Pt foil acquired at room temperature, dashed line; Pt L_3-edge EXAFS oscillation of PtO_2 acquired at room temperature. **b)** A series of Fourier-transformed Pt L_3-edge EXAFS oscillations of PtO_x/Al_2O_3 during in situ reduction with 500 ppm H_2/He at 373 K. Solid line; Fourier-transformed Pt L_3-edge EXAFS oscillation of Pt foil acquired at room temperature, dashed line; Fourier-transformed Pt L_3-edge EXAFS oscillation of PtO_2 acquired at room temperature. **c)** The temporal change in the C.N.(Pt–O)s (black squares) and C.N.(Pt–Pt)s (red circles) of PtO_x/Al_2O_3 during in situ reduction with 500 ppm H_2/He at 373 K.[47]

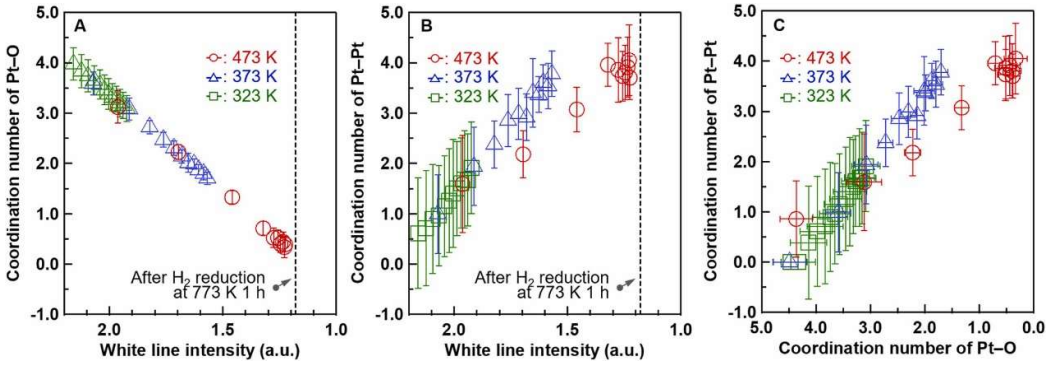

Figure 2-11. a) The correlation between the WL intensities and the *C.N.*(Pt–O)s of each Pt L_3-edge XANES spectrum of PtO_x/Al_2O_3 during in situ reduction with 500 ppm H_2/He. **b)** The correlation between the WL intensities and the *C.N.*(Pt–Pt)s of each Pt L_3-edge XANES spectrum of PtO_x/Al_2O_3 during in situ reduction with 500 ppm H_2/He. **c)** The correlation between the *C.N.*(Pt–O)s and the *C.N.*(Pt–Pt)s of each Pt L_3-edge XANES spectrum of PtO_x/Al_2O_3 during in situ reduction with 500 ppm H_2/He. Red circles; reduced at 473 K, blue triangles; reduced at 373 K, green squares; reduced at 323 K.[47]

These studies collectively indicate a positive path for the utilization of advanced time-resolved characterization techniques in understanding the intricacies of catalyst performance in real-world scenarios, providing valuable insights that have the potential to inform the creation of catalytic materials that are both more efficient and longer-lasting.

2.4 ultra-fast XAS research on heterogeneous catalysis

The intersection of ultra-fast X-ray absorption spectroscopy (XAS) and pump-probe XAS has opened new vistas in understanding dynamic processes on extremely short timescales. These techniques have evolved considerably, offering unprecedented insights into transient states and reaction dynamics in various systems. At the heart of this progress are developments in both theoretical models and experimental methodologies that enhance the temporal and spectral resolution of measurements. Using optical laser pulse and XFEL with certain repetition rate, there is a time delay between two each other, by controlling which the ultra-short temporal resolution with ps or even fs timescale can be achieved between ground state and excited state of materials (Fig. 2-12).

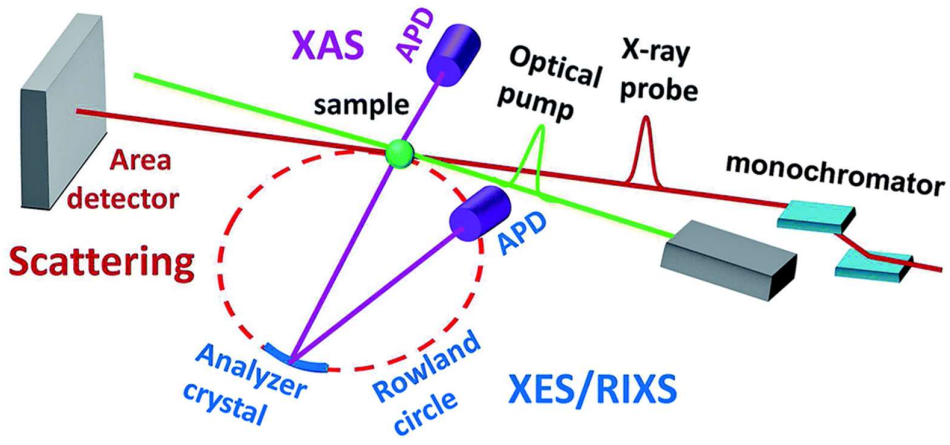

Figure 2-12. Illustration of combined XAS, XES and RIXS measurements at a pump probe set-up.[48]

A selection of research efforts helps encapsulate the state-of-the-art in this swiftly evolving domain. G. Smolentsev et al. have demonstrated a notable application of pump-probe XAS in investigating the triplet state of an Ir-based photosensitizer [49]. Their work combines pump-probe X-ray absorption near edge structure (XANES) spectroscopy with density functional theory (DFT) calculations, offering a nuanced understanding of the excited states of photosensitizers, which are crucial for photovoltaic and photocatalytic applications. This study is representative of the broader utility of pump-probe XAS in dissecting the electronic structures and dynamics of photoactive materials. Further pushing the boundaries of XAS applications, P. Glatzel introduced a novel MHz pump and probe scheme combined with X-ray absorption spectroscopy (XAS-XES) at the European Synchrotron Radiation Facility[50]. By operating at high frequencies, this approach allows for the investigation of transient species and dynamics in materials under conditions closer to real operating environments. Such advancements in experimental setup are critical for the detailed characterization of complex systems such as spin cross-over materials, providing deeper insights into the mechanisms driving their behavior. The work by D. Kido et al. on the metastable structure of photoexcited tungsten oxide (WO_3) showcases another dimension of pump-probe XAS. By examining the local structure of photoexcited states with extended X-ray absorption fine structure spectroscopy, they revealed unexpected structural dynamics in WO_3, demonstrating the power of ultra-fast XAS to uncover novel phenomena that challenge existing theoretical models[51]. These findings underscore the technique's potential in revealing the subtle interplays between electronic and structural dynamics in materials. J. Mahl et al., in their study of optical pump-X-ray probe transient inner-shell absorption spectroscopy, provided essential methodological contributions to understanding the electronic and lattice contributions to spectroscopic signals[52]. This ability to distinguish between and comprehend the roles

of electronic excitation and lattice temperature changes opens new pathways for decoding the behavior of materials under laser excitation. Another notable contribution to this field originates from the research on the evaluation of broad spectrum multi-keV laser plasma x-ray sources for femtosecond time-resolved EXAFS[53]. This study by Forget et al. elucidates the advancement of a potent broad-spectrum x-ray source tailored for EXAFS experiments that can capture the dynamics of physical and chemical processes on the femtosecond time scale. While this study does not directly target heterogeneous catalysts, it introduces a valuable instrument for scrutinizing the rapid changes in coordination environments, potentially adaptable to the examination of catalysts under reaction circumstances.

2.4.1 Transient state and transient species investigation

the transition state (TS) plays a crucial role in comprehending chemical reactivity as it serves to separate reactants from products, and the amount of free energy needed to reach it ultimately governs the kinetics of an elementary chemical reaction. Molecules existing in the TS are notoriously difficult to capture or observe due to their fleeting lifespan, resulting in a nearly negligible TS population under steady-state conditions. Nevertheless, the advent of ultrafast pump-probe techniques has presented novel avenues for investigating molecular configurations in the proximity of the TS region by generating a significant population of molecules, thereby enabling their detection within short timeframes. This advancement in technology has revolutionized the study of chemical reactions by shedding light on previously elusive molecular states, offering invaluable insights into the intricate mechanisms underlying reactivity. By employing such cutting-edge methodologies, researchers can now delve into the realm of transition states with unprecedented precision, unravelling the intricacies of chemical transformations at a molecular level and paving the way for groundbreaking discoveries in the field of chemistry. In essence, the exploration of transition states through innovative experimental approaches represents a fundamental cornerstone in advancing our understanding of chemical reactivity and promises to fuel further advancements in the realm of chemical kinetics and reaction mechanisms.

Some instructive studies by Nilsson and his group were performed monitoring the CO species on Ru surface, investigating the dynamics of electronic structure changing and transient state region. Öström [54] using pump-probe XAS tracks the intransient state region in CO oxidation on Ru. They were using optical laser as a trigger to excites the motions of CO and O on the adsorption site on Ru. By measuring O K-edge XAS for ground state and excited state, a new electronic state for O reveals the dynamics for

formation of transient state of O*C-O and OC-O* (Fig. 2-13). Together with density functional theory calculations (DFT) they suggest that the observed outcomes are a consequence of alterations in the adsorption site and the establishment of bonds between carbon monoxide and oxygen, resulting in a range of carbon-oxygen bond lengths in proximity to the transition state. The detailed process of whole CO oxidation was described: the O is set into motion with movements that are parallel to the surface within a time frame that is less than 300 femtoseconds, while CO is set into motion within a time frame of 500 femtoseconds. As a result of being caged by O atoms in neighbouring sites within the adsorbed honeycomb structure, CO will eventually start colliding on the surface. These collisions give rise to a transient population of species around the transition state (TS) region, which becomes evident on time scales just slightly longer than the initial motions of the CO and O species. It is observed that the majority of these collisions lead to dissociation back into CO and O, followed by further collisions towards the TS, with only a small percentage of the occurrences resulting in the production of CO2, leading to a low reaction yield[55].

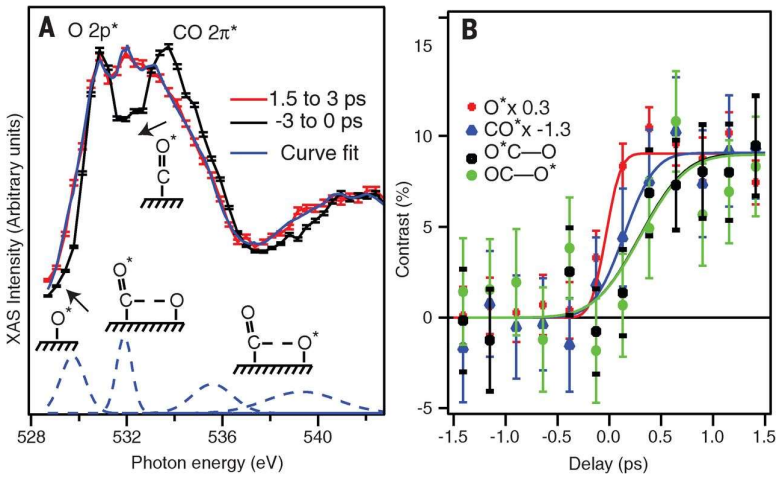

Figure 2-13. Measured x-ray absorption spectra with time-dependent changes. a) Pump-probe O K-edge XAS spectrum of CO/O/Ru(0001).The black line and markers show as reference the spectrum averaged over the 3 ps right before the arrival of the pump pulse, and the red line and markers show the spectrum averaged over the interval between 1.5 and 3 ps after the arrival of the laser pump. Averaging is performed to reduce noise. The solid blue line shows a curve fit obtained from a weighted sum of the unpumped XAS spectrum and the four Gaussians plotted with dashed blue lines in the bottom of the figure, with a red shift of the CO 2p* due to external vibrational motion taken into account. The insets schematically depict the microscopic interpretation of the laser-induced spectral changes, and the arrows indicate the direction of spectral shifts as the O and CO species move out from their equilibrium sites. **b)** Time development of the spectral intensities in four different spectral regions plotted as the contrast. The red dots (O*) show the contrast on the low-energy side of the O 2p* that corresponds to activation of adsorbed O. Note the very fast (280 fs) change in contrast following the pump laser. The blue triangles (CO*) show the contrast on the

CO 2p* resonance, where a negative contrast appears on a 550-fs time scale, corresponding to a loss of intensity after laser irradiation due to activation of external vibrations in the adsorbed CO. The black squares (O*C–O) and green circles (OC–O*) show the contrast around the O–CO p* and O–CO s*, respectively. Both show a transient increase in the contrast on a time scale of 800 fs. [54]

Dell'Angela from the same group using pump-probe XAS and XES observed the bond breaking. We detected changes in the electronic configuration that align with a reduction in the interaction between CO and the substrate, yet there is no significant evidence of desorption occurring[56]. This suggests a shift in the binding mechanism without a noticeable release of molecules. And the dynamics of this electronic structure changing is around 6-10 ps.

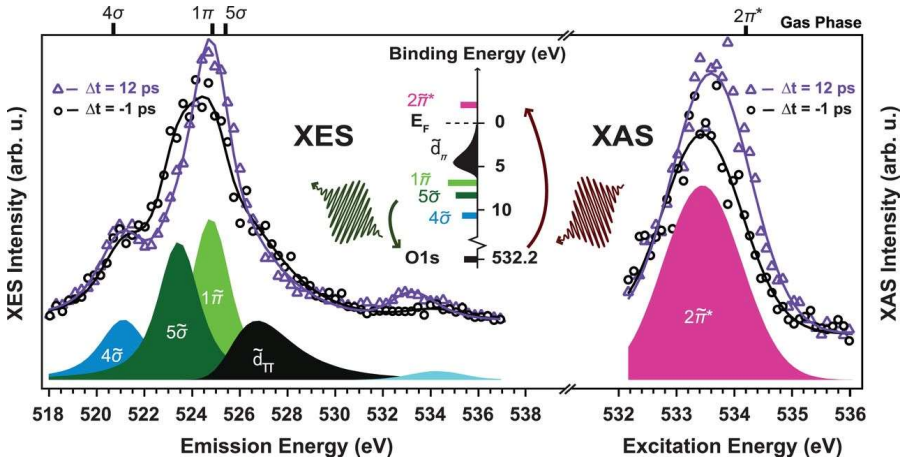

Figure 2-14. Oxygen K-edge XES (left) and XAS (right) spectra (markers) of CO/Ru(0001) and corresponding fits (solid lines) measured at two selected pump-probe delays. At the bottom of the two panels, the peak deconvolution resulting from the fit of the spectra acquired at $\Delta t = -1$ ps is shown. The XAS data have been fitted with a Gaussian peak for the O1*s* →2π˜* resonance. The XES spectra have been fitted with three peaks of Voigt lineshape for the 1π˜, 5σ˜, and 4σ˜ orbitals and an asymmetric Gaussian for the d˜π states; the elastic peak is indicated in light blue around 534 eV. The fit of the spectra at $\Delta t = 12$ ps has been performed by varying only intensity and position of the previously determined components. (**Top**) The positions of the fitted components measured in previous resonant gas phase experiments are also indicated. (**Middle**) A schematic illustration of the excitation process from the O1*s* level to the unoccupied 2π˜* resonance in XAS and the core hole decay process from occupied molecular orbitals back to the O1*s* in XES.[56]

2.4.2 Electron excitation and transition monitoring

Pump probe XAS is a perfect tool for monitoring dynamics of electron excitation or even transition especially for photo-sensitive materials. Since the wavelength of the optical laser can be adjusted, the distinction for different materials can be meet for

excite the electron from valence band to conduction band. There was lots of measurement for metals like Fe[57], Cu[58], Ru[59] to investigate the photo-induced electronic structure changing between ground state and excited state. Chargui and his group did some remarkable works on TiO_2 using pump probe XAS for revealing the nature of trapping sites where the excitation of electron to CB will fall into[60]. And by comparing the anatase and amorphous TiO_2 transient XAS, the difference between trapping sites outer surface and inside the surface shell can be distinguished (Fig. 2-15).

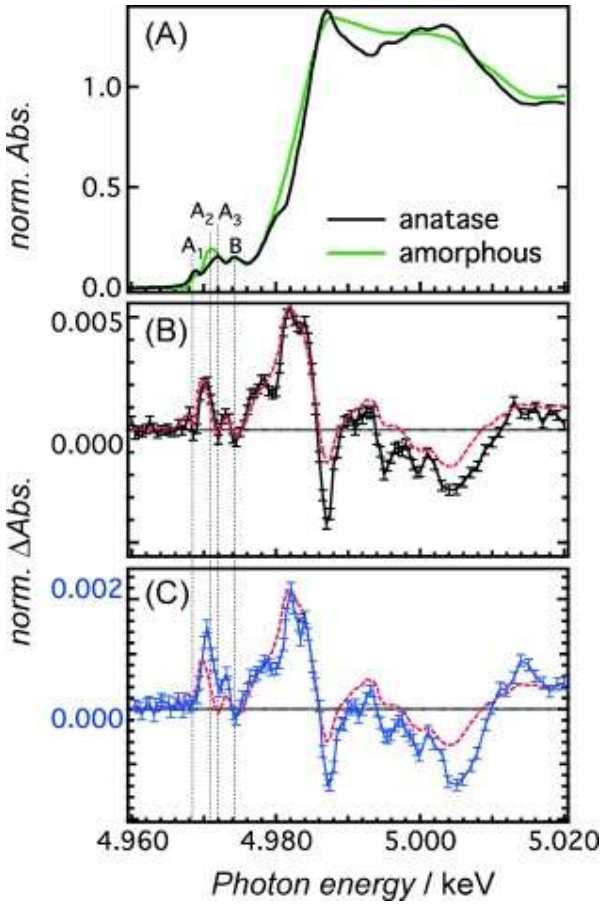

Figure 2-15. Edge region of XAS spectra of anatase and amorphous TiO_2 NPs (pre-edge peaks A_{1-3} and B, and X-ray absorption near-edge structure). a) Ti K-edge absorption spectra of bare anatase and amorphous TiO_2 NPs. b) Transient X-ray absorption spectra of bare anatase TiO_2 NPs excited at 355 nm at a time delay of 100 ps (black) together with the calculated difference spectrum (red dashed line): the amorphous-sample steady-state spectrum shifted by −1 eV, minus the anatase-sample spectrum (the difference spectrum was scaled by 0.016, by normalization at the edge at 4.982 keV; see text). c) Transient XAS spectrum of N719-dye-sensitized anatase TiO_2 NPs at a time delay of 100 ps (blue) after excitation at 532 nm. The dashed red trace is the same as in b), but has been scaled by a factor of 0.006. [60]

Similarly, Obara studied the dynamics of the electron trapping in anatase TiO_2 with fs temporal resolution XAS for Ti K-edge[61]. Before dynamics study, they investigated the excitation optical laser power intensity dependence on Ti K-edge XANES (Fig.2-16). As shown in figure, a linear dependence revealed that multiphoton excitation can be neglected below 140 μJ excitation intensity. After that, the temporal profile of the changing of each features in Ti K-edge XANES was studied. The phenomenon of edge shift observed in this study is attributed to the entrapment of conduction band electrons within self-trapped polarons or penta-coordinated Ti sites. Through experimental analysis, it was found that the rise times required for the development of the pre-edge peak and the decrease of the peak above the edge fell within the timeframe of 300 to 400 femtoseconds, as determined with the assistance of arrival-time diagnostics. These timeframes are indicative of the dynamic structural distortions occurring at the penta-coordinated sites located in close to the surface region.

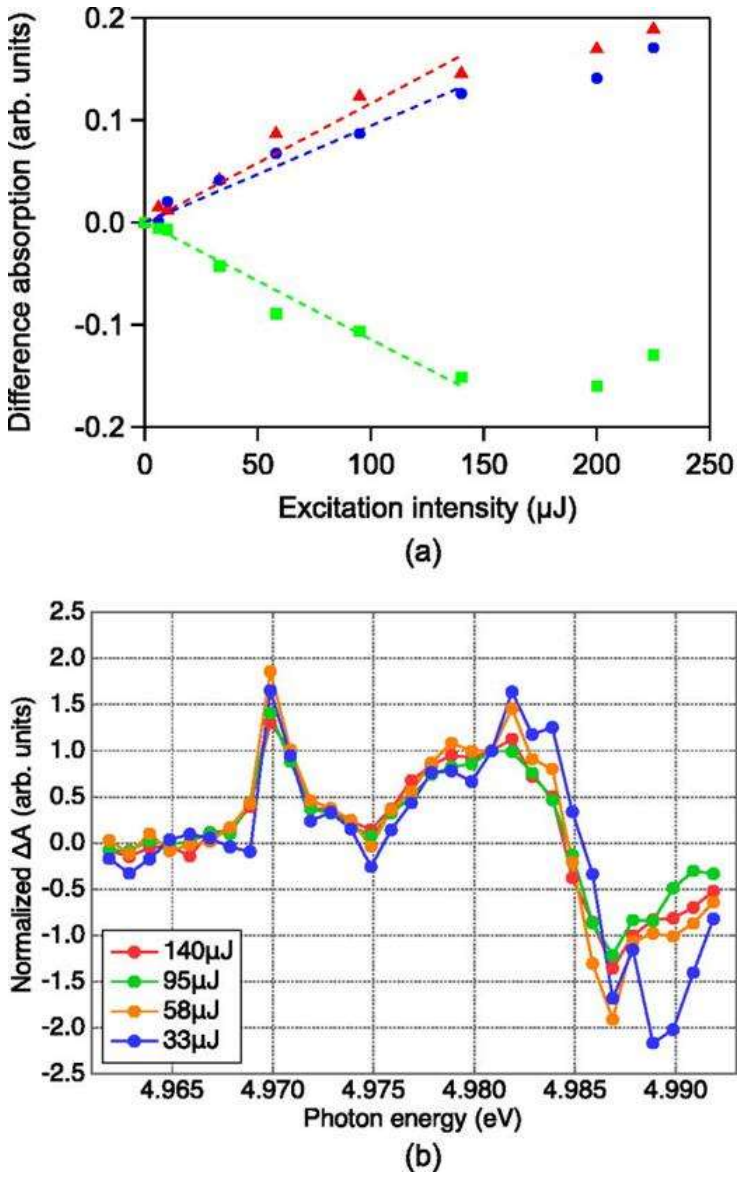

Figure 2-16. a) Change of absorbance at 4.9695 keV (pre-edge), 4.9815 keV (edge), and 4.9865 keV (above-edge) as a function of the UV excitation intensity. The absorbance shows a linear dependence up to 140 μJ. The dashed lines are a linear fit of each dataset within 140 μJ. **b)** Normalized difference absorption spectra excited at 140, 95, 58, and 33 μJ/pulse. The spectra exhibit identical features up to 140 μJ, which indicates that multiphoton effects are unimportant up to at least this intensity.[61]

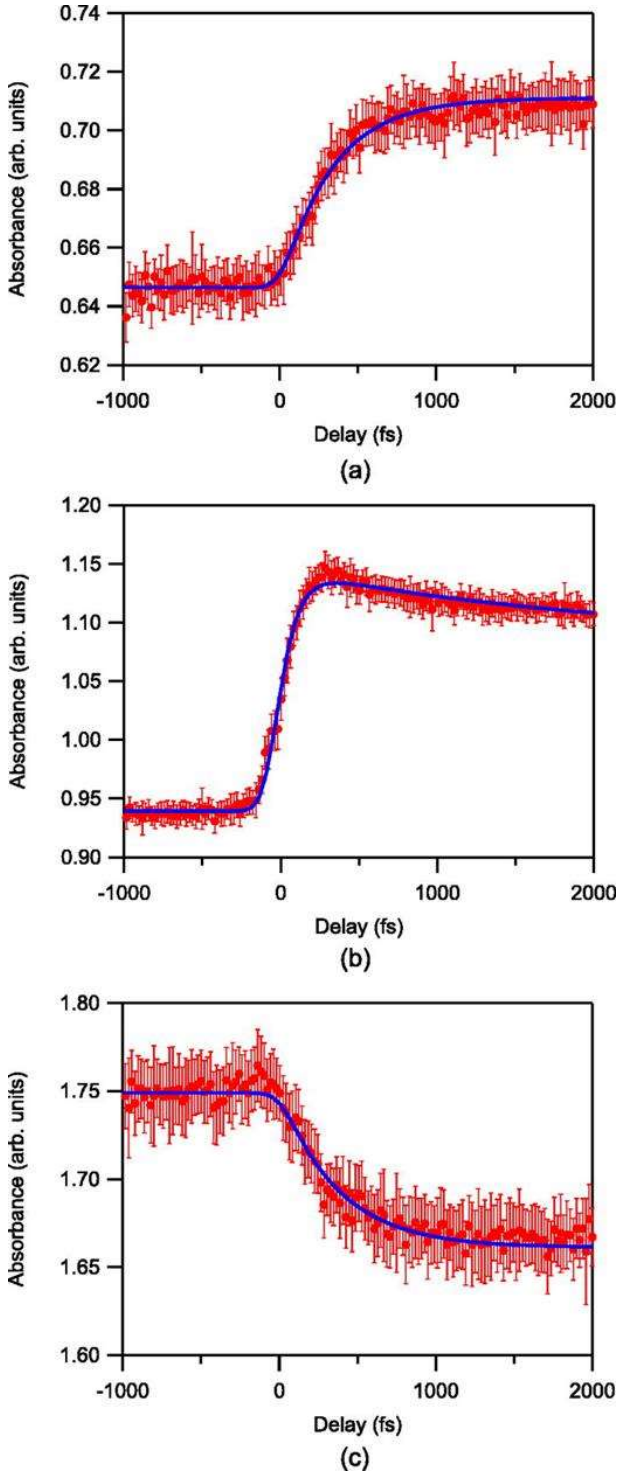

Figure 2-17. Transient profiles together with fitted decay curves at **a)** 4.9695 keV, **b)** 4.9815 keV, and **c)** 4.9865 keV. The red dots show the absorbance of the sorted dataset averaged with a time window of 20 fs. The error bars represent the standard error of the average. The blue line is a least-squares fit to the data. [61]

Apart from these, scientists from PAL (Pohang Accelerator Laboratory) use soft x-ray XFEL to observe the dynamics of hole transfer. Kown and his college Park present a demonstration of the intricate exploration of the behaviour of photo-induced gaps within metal oxides[62]. Through their meticulous investigation, they have successfully determined the precise energy levels and extended lifespan of these gaps, particularly showcasing an impressive longevity of 230 ps within nano-crystalline TiO_2. Furthermore, their comprehensive analysis has revealed that the confined gaps exhibit a notable energy dispersion within the bandgap zone, unveiling a swift formation period of merely 0.3 ps and a subsequent decay span of 8.0 ps under standard room temperature conditions. Additionally, our research has also established a coherent correlation between the behaviours of the electrons through the utilization of X-ray absorption spectroscopy at the metal L-edges, providing a holistic and synchronized elucidation of the dynamics observed in conjunction with the aforementioned gaps.

Together, these studies underscore the substantial progress and the diverse applications of ultra-fast XAS and pump-probe XAS techniques in contemporary research. From elucidating excited-state dynamics in photosensitizers to investigating the response of materials to photoexcitation, these techniques offer a rich toolkit for unravelling the complexities of materials on the shortest timescales. As theoretical and technological advancements continue, it is expected that ultra-fast XAS and pump-probe XAS will further deepen our understanding of dynamic processes in materials science, chemistry, and beyond.

2.5 Reference

1 Reimers, W., Pyzalla, A. R., Schreyer, A. & Clemens, H. Neutrons and synchrotron radiation in engineering materials science. *From Fundamentals to Material and component characterization* (2008).

2 Cutsail Iii, G. E. & DeBeer, S. Challenges and Opportunities for Applications of Advanced X-ray Spectroscopy in Catalysis Research. *ACS Catalysis* **12**, 5864-5886 (2022). https://doi.org:10.1021/acscatal.2c01016

3 Zimmermann, P. *et al.* Modern X-ray spectroscopy: XAS and XES in the laboratory. *Coordination Chemistry Reviews* **423**, 213466 (2020).

4 Vogel, M. (Taylor & Francis, 2022).

5 Gürsoy, D., De Carlo, F., Xiao, X. & Jacobsen, C. TomoPy: a framework for the analysis of synchrotron tomographic data. *Journal of synchrotron radiation* **21**, 1188-1193 (2014).

6 Winick, H. Personal View: Personal View on the Development of Synchrotron Radiation Research Facilities and Insertion Devices. *Synchrotron Radiation News* **20**, 4-8 (2007).

7 Winick, H. in *AIP Conference Proceedings*. 2138-2182 (American Institute of Physics).

8 Fan, C. & Zhao, Z. *Synchrotron radiation in materials science: light sources, techniques, and applications*. (John Wiley & Sons, 2018).

9 Tschentscher, T. *et al.* Photon Beam Transport and Scientific Instruments at the European XFEL. *Applied Sciences* **7**, 592 (2017).

10 Ayvazyan, V. *et al.* First operation of a free-electron laser generating GW power radiation at 32 nm wavelength. *The European Physical Journal D-Atomic, Molecular, Optical and Plasma Physics* **37**, 297-303 (2006).

11 Saldin, E. L., Schneidmiller, E. & Yurkov, M. V. *The physics of free electron lasers*. (Springer Science & Business Media, 2013).

12 Wu, R. *et al.* in *Journal of Physics: Conference Series*. 012001 (IOP Publishing).

13 Grünert, W. & Klementiev, K. X-ray absorption spectroscopy principles and practical use in materials analysis. *Physical Sciences Reviews* **5**, 20170181 (2020).

14 Torchio, R. *et al.* Probing local and electronic structure in Warm Dense Matter: single pulse synchrotron x-ray absorption spectroscopy on shocked Fe. *Scientific Reports* **6**, 26402 (2016).

15 Kristiansen, P. T., Rocha, T., Knop-Gericke, A., Guo, J. & Duda, L. Reaction cell for in situ soft x-ray absorption spectroscopy and resonant inelastic x-ray scattering measurements of heterogeneous catalysis up to 1 atm and 250° C. *Review of Scientific Instruments* **84** (2013).

16 Weckhuysen, B. M. Snapshots of a working catalyst: possibilities and limitations of in situ spectroscopy in the field of heterogeneous catalysis. *Chemical Communications*, 97-110 (2002).

17 Mitsunobu, S., Takahashi, Y. & Uruga, T. Observation of chemical reactions at the solid–water interface by quick XAFS combined with a column reactor. *Analytical chemistry* **78**, 7040-7043 (2006).

18 Ginder-Vogel, M., Landrot, G., Fischel, J. S. & Sparks, D. L. Quantification of rapid environmental redox processes with quick-scanning x-ray absorption spectroscopy (Q-XAS). *Proceedings of the National Academy of Sciences* **106**, 16124-16128 (2009).

19 Dent, A. J. Development of time-resolved XAFS instrumentation for quick EXAFS and energy-dispersive EXAFS measurements on catalyst systems. *Topics in Catalysis* **18**, 27-35 (2002).

20 Borri, M. *et al.* Characterisation of Ge micro-strip sensors with a micro-focused X-ray beam. *Nuclear Instruments and Methods in Physics Research Section A: Accelerators, Spectrometers, Detectors and Associated Equipment* **988**, 164932 (2021).

21 Pascarelli, S., Mathon, O., Munoz, M., Mairs, T. & Susini, J. Energy-dispersive absorption spectroscopy for hard-X-ray micro-XAS applications. *Journal of synchrotron radiation* **13**, 351-358 (2006).

22 Ishiguro, N. & Tada, M. Structural kinetics of cathode events on polymer electrolyte fuel cell catalysts studied by operando time-resolved XAFS. *Catalysis Letters* **148**, 1597-1609 (2018).

23 Sonntag, B. VUV and X-ray free-electron lasers. *Nuclear Instruments and Methods in Physics Research Section A: Accelerators, Spectrometers, Detectors and Associated Equipment* **467**, 8-15 (2001).

24 Pellegrini, C. The next generation of X-ray sources. *Reviews of Accelerator Science and Technology* **3**, 185-202 (2010).

25 Milne, C., Penfold, T. & Chergui, M. Recent experimental and theoretical developments in time-resolved X-ray spectroscopies. *Coordination Chemistry Reviews* **277**, 44-68 (2014).

26 Barletta, W. *et al.* Free electron lasers: Present status and future challenges. *Nuclear Instruments and Methods in Physics Research Section A: Accelerators, Spectrometers, Detectors and Associated Equipment* **618**, 69-96 (2010).

27 Gaillard, J.-F., Webb, S. M. & Quintana, J. P. Quick X-ray absorption spectroscopy for determining metal speciation in environmental samples. *Journal of Synchrotron Radiation* **8**, 928-930 (2001).

28 Zitolo, A. *et al.* Identification of catalytic sites for oxygen reduction in iron-and nitrogen-doped graphene materials. *Nature materials* **14**, 937-942 (2015).

29 Bacquart, T. *et al.* Subcellular speciation analysis of trace element oxidation states using synchrotron radiation micro-X-ray absorption near-edge structure. *Analytical chemistry* **79**, 7353-7359 (2007).

30 Reitz, T. *et al.* Time-resolved XANES investigation of CuO/ZnO in the oxidative methanol reforming reaction. *Journal of catalysis* **199**, 193-201 (2001).

31 Shapovalova, S. *et al.* Temperature and time-resolved XANES studies of novel valence tautomeric cobalt complex. *Chemistry Letters* **50**, 1933-1937 (2021).

32 Oezaslan, M. *et al.* in *Electrochemical Society Meeting Abstracts 242.* 1900-1900 (The Electrochemical Society, Inc.).

33 Friebel, D., Miller, D. J., Nordlund, D., Ogasawara, H. & Nilsson, A. Degradation of Bimetallic Model Electrocatalysts: An In Situ X-Ray Absorption Spectroscopy Study. *Angewandte Chemie International Edition* **50**, 10190-10192 (2011).

34 Browne, M. P. *et al.* Probing Changes in the Local Structure of Active Bimetallic Mn/Ru Oxides during Oxygen Evolution. *ACS Applied Energy Materials* **6**, 8607-8615 (2023).

35 Gervais, C., Lanquille, M.-A., Moretti, G. & Réguer, S. in *Journal of Physics: Conference Series.* 012139 (IOP Publishing).

36 Koga, H. *et al.* Operando X-ray absorption study of the redox processes involved upon cycling of the Li-rich layered oxide Li1. 20Mn0. 54Co0. 13Ni0. 13O2 in Li ion batteries. *The Journal of Physical Chemistry C* **118**, 5700-5709 (2014).

37 Kang, L. *et al.* The Electrophilicity of Surface Carbon Species in the Redox Reactions of CuO-CeO2 Catalysts. *Angewandte Chemie* **133**, 14541-14549 (2021).

38 Safonova, O. V. *et al.* Elucidating the Oxygen Activation Mechanism on Ceria-Supported Copper-Oxo Species Using Time-Resolved X-ray Absorption Spectroscopy. *ACS Catalysis* **10**, 4692-4701 (2020). https://doi.org:10.1021/acscatal.0c00551

39 Grunwaldt, J.-D., Caravati, M., Hannemann, S. & Baiker, A. X-ray absorption spectroscopy under reaction conditions: suitability of different reaction cells for combined catalyst characterization and time-resolved studies. *Physical Chemistry Chemical Physics* **6**, 3037-3047 (2004).

40 Nemana, S., Sun, J. & Gates, B. C. Reactivity of binuclear tantalum clusters on silica: Characterization by transient time-resolved spectroscopy. *The Journal of Physical Chemistry C* **112**, 7477-7485 (2008).

41 Boland, D. D., Collins, R. N., Glover, C. J. & Waite, T. D. An in situ quick-EXAFS and redox potential study of the Fe (II)-catalysed transformation of ferrihydrite. *Colloids and Surfaces A: Physicochemical and Engineering Aspects* **435**, 2-8 (2013).

42 Dabros, T. M. H. *et al.* Influence of H2O and H2S on the composition, activity, and stability of sulfided Mo, CoMo, and NiMo supported on MgAl2O4 for hydrodeoxygenation of ethylene glycol. *Applied Catalysis A: General* **551**, 106-121 (2018).

43 Nikulshina, M. *et al.* Genesis of active phase in MoW/Al2O3 hydrotreating catalysts monitored by HAADF and in situ QEXAFS combined to MCR-ALS analysis. *Applied Catalysis B: Environmental* **269**, 118766 (2020).

44 Liang, A. J. & Gates, B. C. Time-resolved structural characterization of formation and break-up of rhodium clusters supported in highly dealuminated Y zeolite. *The Journal of Physical Chemistry C* **112**, 18039-18049 (2008).

45 Yamamoto, T. *et al.* Origin and dynamics of oxygen storage/release in a Pt/ordered CeO2–ZrO2 catalyst studied by time-resolved XAFS analysis. *Angewandte Chemie International Edition* **46**, 9253-9256 (2007).

46 Nagai, Y. *et al.* X-ray absorption fine structure analysis of local structure of CeO2–ZrO2 mixed oxides with the same composition ratio (Ce/Zr=1). *Catalysis Today* **74**, 225-234 (2002). https://doi.org:https://doi.org/10.1016/S0920-5861(02)00025-1

47 Kikkawa, S., Teramura, K., Asakura, H., Hosokawa, S. & Tanaka, T. In situ time-resolved XAS study on metal-support-interaction-induced morphology change of PtO2 nanoparticles supported on γ-Al2O3 under H2 reduction. *Catalysis Today* **410**, 157-163 (2023).

48 Chen, L. X., Zhang, X. & Shelby, M. Recent advances on ultrafast X-ray spectroscopy in the chemical sciences. *Chemical science* **5**, 4136-4152 (2014).

49 Smolentsev, G. *et al.* Pump—probe XAS investigation of the triplet state of an Ir photosensitizer with chromenopyridinone ligands. *Photochemical & Photobiological Sciences* **17**, 896-902 (2018).

50 Glatzel, P. & Juhin, A. X-ray Absorption and Emission Spectroscopy. *Local Structural Characterisation: Inorganic Materials Series*, 89-171 (2013).

51 Kido, D. *et al.* Metastable Structure of Photoexcited WO3 Determined by the Pump-probe Extended X-ray Absorption Fine Structure Spectroscopy and Constrained Thorough Search Analysis. *Chemistry Letters* **51**, 1083-1086 (2022).

52 Mahl, J. *et al.* Decomposing electronic and lattice contributions in optical pump–X-ray probe transient inner-shell absorption spectroscopy of CuO. *Faraday discussions* **216**, 414-433 (2019).

53 Forget, P. *et al.* in *Applications of X Rays Generated from Lasers and Other Bright Sources II.* 49-55 (SPIE).

54 Öström, H. *et al.* Probing the transition state region in catalytic CO oxidation on Ru. *Science* **347**, 978-982 (2015).

55 Her, T.-H., Finlay, R. J., Wu, C. & Mazur, E. Surface femtochemistry of CO/O 2/Pt (111): The importance of nonthermalized substrate electrons. *The Journal of chemical physics* **108**, 8595-8598 (1998).

56 Dell'Angela, M. *et al.* Real-time observation of surface bond breaking with an x-ray laser. *Science* **339**, 1302-1305 (2013).

57 Ogi, Y. *et al.* Ultraviolet photochemical reaction of [Fe (III)(C2O4) 3] 3− in aqueous solutions studied by femtosecond time-resolved X-ray absorption spectroscopy using an X-ray free electron laser. *Structural Dynamics* **2** (2015).

58 Penfold, T. J. *et al.* Solvent-induced luminescence quenching: Static and time-resolved x-ray absorption spectroscopy of a copper (I) phenanthroline complex. *The Journal of Physical Chemistry A* **117**, 4591-4601 (2013).

59 El Nahhas, A. *et al.* X-ray absorption spectroscopy of ground and excited rhenium–carbonyl–diimine complexes: Evidence for a two-center electron transfer. *The journal of physical chemistry A* **117**, 361-369 (2013).

60 Rittmann-Frank, M. H. *et al.* Mapping of the Photoinduced Electron Traps in TiO2 by Picosecond X-ray Absorption Spectroscopy. *Angewandte Chemie International Edition* **53**, 5858-5862 (2014). https://doi.org:https://doi.org/10.1002/anie.201310522

61 Obara, Y. *et al.* Femtosecond time-resolved X-ray absorption spectroscopy of anatase TiO2 nanoparticles using XFEL. *Structural Dynamics* **4** (2017). https://doi.org:10.1063/1.4989862

62 Park, S. H. *et al.* Direct and real-time observation of hole transport dynamics in anatase TiO2 using X-ray free-electron laser. *Nature communications* **13**, 2531 (2022).

Chapter 3

Oxygen vacancy formation as the rate-determining step in the Mars-van Krevelen mechanism

3.1 Abstract

The Mars-van Krevelen mechanism (MvK) is a widely recognized model for describing the role of lattice oxygen in catalysis. Following the MvK mechanism, the formation and conversion of surface oxygen vacancy (V_O) are considered as the key steps. CeO_2-ZrO_2 (CZ) mixed oxides are the typical catalyst support in MvK mechanism. They have the unique property of hosting remarkable amount of V_O without significant change in lattice structure, offering O storage and release capability that maintains the required concentration of active O on the catalytic surface. In this regard, the rate of V_O formation and conversion directly affect their catalytic performance. In this work, we obtained the V_O formation and conversion kinetics by measuring the rate of the Ce^{4+} reduction and oxidation *via operando* energy dispersive Extended X-ray Absorption Fine Structure (EDE). The main conclusions are: 1) V_O formation is 10 times slower than V_O conversion; 2) V_O formation rates are comparable with the CO oxidation rates, thereby serving as the rate-determining step in CO oxidation; 3) Pd and Cu serve as catalysts for V_O formation by significantly improving its rate by 50 times at 250 °C by weakening the metal-O bonding strength, whereas the activation energy have been reduced to 58.4 kJ/mol and 36.5 kJ/mol, respectively. Our method in measuring and analysing partial reaction rates within a turnover is therefore important for all chemical reactions.

3.2 Introduction:

Oxygen storage materials (OSMs) are widely used in catalysis, energy conversion and medical devices with their ability to store and release oxygen reversibly [1,2]. CeO_2-ZrO_2 (CZ) is a commercial OSM material used in the automobile three-way catalysts and solid oxide fuel cells[3]. The successful commercial application of CZ materials has led people to consider their use in other catalytic reactions, especially oxidation reactions[4-7] and CO_2 reduction. CZ is a solid solution of cerium oxide (CeO_2) and zirconium oxide (ZrO_2), in which Zr^{4+} and Ce^{4+} are homogeneously dispersed in the lattice, providing the ability to store and release oxygen ions, which takes very important role in the redox of reactants such as CO, NO and hydrocarbons (C_xH_y)[8]. ZrO_2 can enhance the oxygen storage capacity (OSC) of CeO_2 by promoting the formation of oxygen vacancies (V_O) and stabilizing the structure after the O release[9], and thus the OSC performance.

After being commercialised for over 20 years[10], studies focused on such successful catalyst are in an endless stream, from synthesis[11] to catalytic performance; from crystal structure[12-14] to electronic structure[15,16]. Meanwhile, Mars-van Krevelen (MvK) mechanism is well established for V_O formation in Ce based catalysts to explain what

role Ce plays in this catalysis reaction. The kinetic studies based on MvK mechanism were usually including all the processes including CO adsorption; CO_2 formation (eq. 3-2); CO_2 desorption & V_O formation (eq. 3-3); and O_2 adsorption at V_O (eq. 3-4). However, the kinetics of every single process were rarely studied, especially for the rate of surface CO_2 formation (eq. 3-2) and V_O formation (eq. 3-3). To investigate the kinetics of these processes, the complete CO oxidation reaction was separated to two half reactions: V_O formation reaction where CO reduced Ce (eq. 3-2&3) and V_O conversion reaction where O_2 re-oxidized Ce (eq. 3-4).

Unlike catalytic CO oxidation with both CO and O_2 continuously feed (equation. 1), V_O formation reaction consumes lattice oxygen (equation. 3-2 & 3, $-r = k*p_{CO}*C_{[O]}$, in which p_{CO} is the CO pressure and $C_{[O]}$ is the reactive lattice O concentration). This results in a CO and lattice oxygen concentration gradient where the upstream of the catalyst is reacted in the first instance at the very beginning of the CO flux, while downstream the catalyst has not even come into contact with the CO. And the diffusion of CO within the catalysts also effects the dynamics of reaction. These gas transport limitations are nearly unavoidable for fixed bed reactor using gas detection in exhaust, which ultimately makes exceedingly challenging to measure half reaction kinetics precisely, thereby complicating the overall understanding of the reaction dynamics involved. With time-resolved XAFS studies, we measure the rate of Ce4+ reduction in the beginning of the bed, because detecting the catalysts directly is more accurate than measuring the CO2 concentration in the exhaust.

$$O_2 + 2CO = 2CO_2 \qquad \text{eq. 3-1}$$

$$Ce^{4+} - O^{2-} - M^{x+} + CO = Ce^{4+} - C^{2+}O^{2-}{}_2 - M^{x+} \qquad \text{eq. 3-2}$$

$$Ce^{4+} - C^{2+}O^{2-}{}_2 - M^{x+} = Ce^{3+} - V_O - M^{(x-1)+} + CO_2 \qquad \text{eq. 3-3}$$

$$Ce^{3+} - V_O - M^{(x-1)+} + 1/2\ O_2 = Ce^{4+} - O^{2-} - M^{x+} \qquad \text{eq. 3-4}$$

M is the metal boned with Ce and O.

Noble metals such as Pd are the main active metals in three-way catalysts. They not only provide active site to convert CO, C_xH_y and NO_x, but can also improve the OSC performance of CZ[17,18]. 3d transition metals, such as Cu, are also considered [19-21], partially due to their strong metal-support interaction with CeO_2[15,22]. Now the OSC under steady state of Cu-CZ is as good as CZ materials dopped by noble metals with similar loading[23]. Here the impact of the metal sites in the V_O formation kinetics is studied for CZ, Cu-CZ and Pd-CZ catalysts. The results show that highly dispersed Cu and Pd not only improved OSC but also the serving as the catalyst for V_O formation reaction. As a result, they led to a significant improvement in catalytic performance of CO oxidation.

3.3 Results and Discussion

3.3.1 Geometric and electronic structure of CZ

In general, there is no phase separation in all three CZ samples. HAADF-STEM image (Fig.1a) and BF-STEM (Supplementary Fig. S3-1) suggest that Ce and Zr disperse uniformly in the CZ solid solution with the lattice plane spacing of (101): 0.304nm (red); (002)(110): 2.632nm (blue); (112)(200): 1.867nm (green) and (211): 1.588nm(yellow) which match the crystal plane spacing of $Ce_{0.5}Zr_{0.5}O_2$ standard (P42/nmc)[24]. The distribution of Ce and Zr is homogeneous according to EDX maps (Fig. 3-1a). Different from other studies, all three CZ catalysts have tetragonal structure (Fig. 3-1e) but not the cubic structure which is more commonly observed. According to Duwez and Odell's phase diagram[25], when atom ratio between Ce and Zr is close to 1:1, and the temperature is below 1000 ºC, there should be a mixture of cubic and tetragonal crystalised phase, but the exact content of each phase is still unknown.

Ce K-edge XANES (Fig. 3-1b) shows almost the same absorption edge position around 40450 eV which is the 1s→6p transition, indicating that the oxidation state of most Ce remains 4+. The Fourier-Transform of EXAFS (Fig. 3-1c) shows obvious difference in Ce-O coordination and the second shell coordination comparing with CeO_2 standard, demonstrating the microstructure of CZ materials is different from CeO_2 standard, which also proving the formation of CeO_2-ZrO_2 solid solution phase[26]. Ce-O bond distance is also slightly shorter than which in CeO_2 standard based on the EXAFS fitting results: R_Ce-O_CeO_2=2.343 Å; R_Ce-O_CZ=2.256 ± 0.012 Å; R_Ce-O_Cu-CZ=2.260 ± 0.015 Å and R_Ce-O_Pd-CZ=2.269 ± 0.025 Å (Supplementary Table. 1 and Fig. S3-13). Zr K-edge XANES (Fig. 3-1d) also shows the same absorption edge for all three CZ samples. The pre-edge peak A refers to the 1s→4d electron transition, which is influenced by the Zr-O coordination geometry[27]. It is more intense in compounds that deviate from central symmetric, and is particularly noticeable in pure tetragonal ZrO_2[28]. Comparing with the tetragonal ZrO_2 standard which has a single white line peak(Fig. 1d), the peak B splitting is because of the CeO_2 concentration in the solid solution and changed the coordination environment for Zr[29]. Finally, adding Pd and Cu does not change the electronic (XANES) and geometric (EXAFS) structure of the CZ.

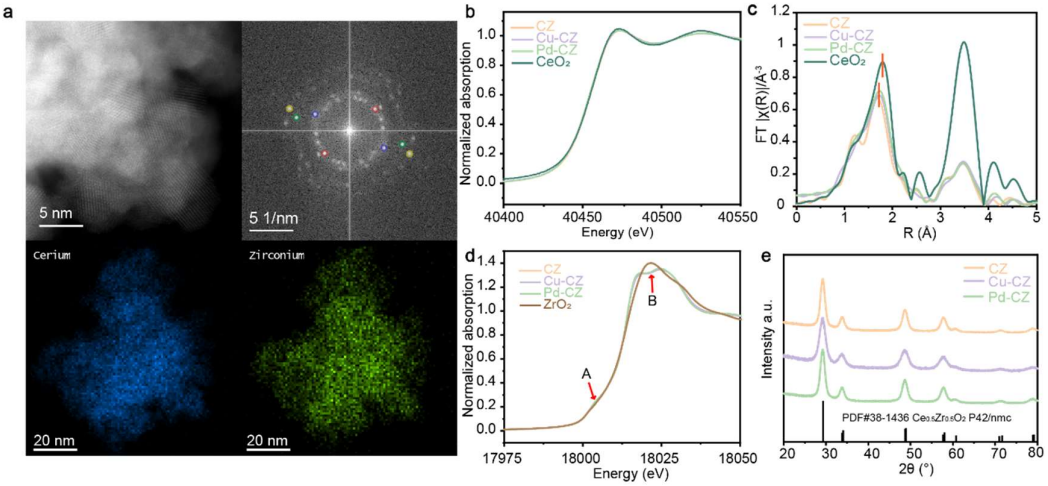

Figure 3-1. Morphology and electronic structure of CZ samples. a. HAADF-STEM image and reduced FFT, and EDX mapping for CZ. **b.** Ce K-edge XANES of CZ; Cu-CZ; Pd-CZ and CeO_2 standard. **c.** Ce K-edge Fourier-Transform EXAFS of CZ; Cu-CZ; Pd-CZ and CeO_2 standard. **d.** Zr K-edge XANES of CZ; Cu-CZ; Pd-CZ and ZrO_2 standard. **e.** PXRD for CZ; Cu-CZ; Pd-CZ and the standard PDF.

3.3.2 Mars-van Krevelen mechanism

The conventional MvK mechanism for CO oxidation includes CO adsorption; CO_2 formation reaction; CO_2 desorption and V_O formation; and O_2 adsorption to refill the V_O (Fig.3- 2a). The part of these processes in which Ce is directly involved is step ii; step iii (V_O formation) and step iv (V_O conversion). To obtain accurate kinetics for these steps, the quantification of Ce^{3+}/Ce^{4+} at the beginning of the bed is required. This has also been confirmed in the literature,[30] in which different position of a catalytic bed is measured with XAS, and concluded that the diffusion can be avoid when measure the upstream of the catalyst. This can be obtained by measuring Ce L_3 edge EDE spectra with high time resolution under *operando* conditions. This is also based on the previous discussion that the process of V_O formation release can in turn be regarded as a reduction of Ce process (equation. 2 & 3), whereas Zr will not be reduced during this process (Fig. 3-2b). Our *operando* EDE setup directly measures the Ce species at the beginning of the bed (Fig. 3-2a). A micro-focused beam size (H×V=30μm×100μm), the concentration gradience of CO/CO_2 within the beam is negligible. During quick gas switch between CO and O_2 without changing the overall weight hour space velocity (WHSV = 10,000 $ml_{CO}/g{\cdot}h$), the Ce reduction and oxidation during the gas switch were monitored by measuring the time-resolved Ce L_3 edge XAFS (Fig. 3-2b).

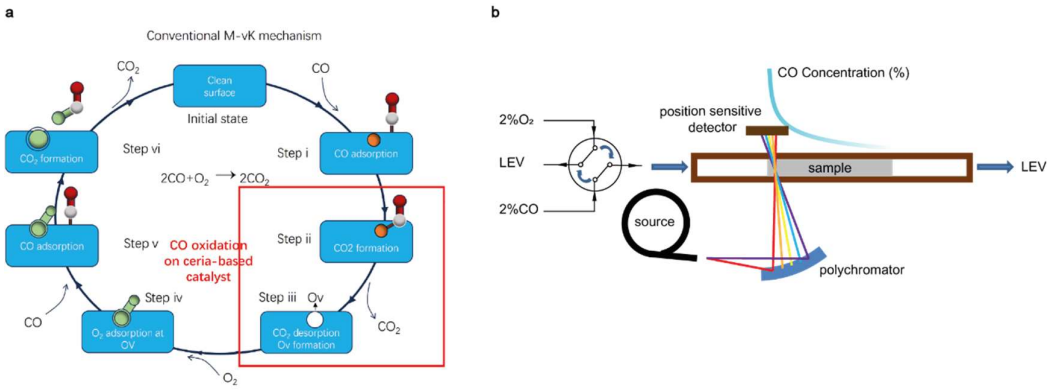

Figure 3-2. a. Mars-van Krevelen mechanism for CO oxidation on ceria-based catalysts reaction flow chart. **b.** schematic of the EDE reactor setup

3.3.3 Redox behaviour and oxygen storage capacity

Enhancing the redox properties of Ce is a top priority for increasing OSC of OSMs. By comparing the energy of the absorption edge of the Ce K edge XANES, the change of valence state of Ce can be monitored in CO temperature programmed reduction (TPR). With 1wt% of Cu or 0.6wt% Pd doping, the redox ability of Ce at low temperature was significantly improved (Supplementary Fig. S3-2). The first derivative of XANES shows an obvious absorption peak shift upon reduction under CO (Supplementary Fig.3-3). The first derivative peak position is around 40456 eV for all three CZ samples under O_2. Heating under CO from 75 °C to 250 °C, the maximum peak shift is around 0.7 eV, 6.7 eV and 7.3 eV to the left for CZ, Cu-CZ and Pd-CZ (Supplementary Fig.S3-3). Such reduced peak feature is plotted as the function of temperature (Fig. 3-3d). Cu-CZ (Fig. 3-3a) and Pd-CZ (Supplementary Fig.S3-3) start reducing at 100 °C with a steady decay of Ce^{4+} concentration along the increase of temperature. CZ, on the other hand, has only small amount of reduction, indicating the improve Ce reduction and thus OSC performance in the presence of Cu and Pd at low temperatures. The surface sensitive soft x-ray NEXAFS was also used to test the redox ability of surface metal and the results shows similar phenomena (Supplementary Fig. S3-4 & 5). Zr K edge XANES were measured under the same *in situ* conditions as Ce K edge (Fig. 3b & Supplementary Fig. S3-6). There is no obvious change in the absorption edges of all three CZ materials, which proves that the valence state of Zr hardly changes during the heating process (Fig. 3-3e). Therefore, only the reduction of Ce is considered when looking at OSC.

OSC was measured by integrating the real-time concentration of CO_2 produced (Supplementary Fig. S3-8) in eq. 2 and subsequently converted into the amount of O released (Fig. 3-3c). The OSC is in the orders of Pd-CZ > Cu-CZ >> CZ for all

temperatures, which correlates well with the Ce reduction determined in the Ce K edge (Fig. 3-3f, Supplementary Fig. S3-7).

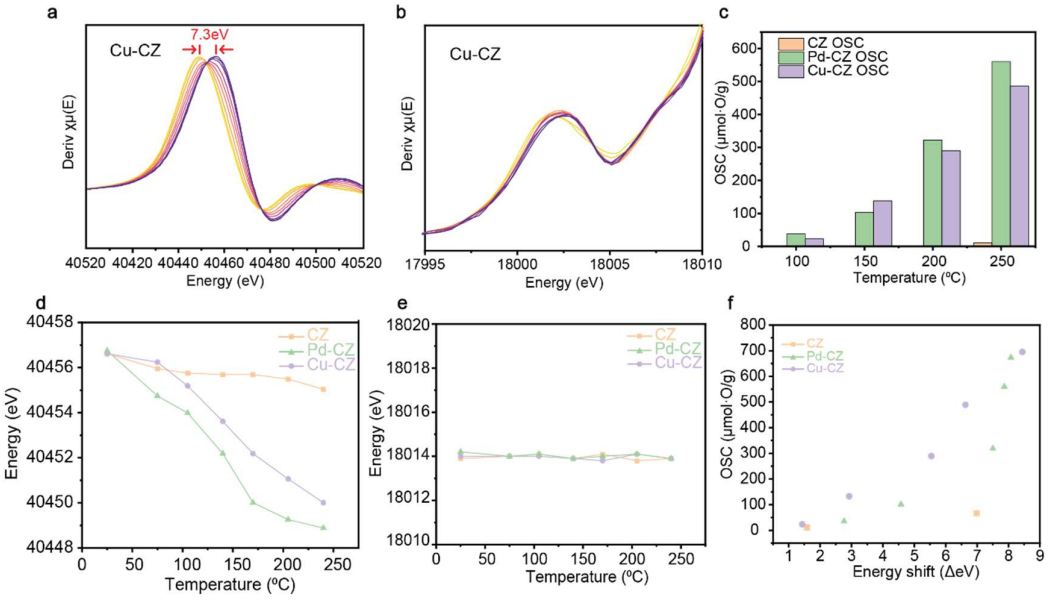

Figure 3-3. Ce redox behaviour and oxygen storage capacity. a. The first derivative of Ce K-edge XANES for Cu-CZ in CO TPR (RT & 240 °C, 40sccm 10% CO and 160 sccm 100% He). **b.** The first derivative of Zr K-edge XANES for Cu-CZ in CO TPR (RT & 240 °C, 40sccm 10% CO and 160 sccm 100% He). **c.** OSC for CZ, Pd-CZ and Cu-CZ. **d.** The absorption edge position of Ce K-edge XANES in CO TPR. **e.** The absorption edge position of Zr K-edge XANES in CO TPR. **f.** The energy shift of XANES absorption edge with oxygen storage capacity.

3.3.4 Vo formation and conversion kinetics determined by time resolved EDE

The unavoidable effect of CO diffusion makes it extremely difficult to study the kinetics of the oxygen release *via* measuring the exhaust CO or CO_2 concentration (Supplementary Fig. S3-7). The shift of the main peak to lower energies in the Ce L_3 edge XANES as the reduction progresses can be seen as an increase in the Ce^{3+} contribution and a decrease in the Ce^{4+} (Fig. 3-4a). The relative Ce^{3+} and Ce^{4+} content were determined based on the peak fitting results of *in situ* EDE result with 0.5 s time resolution (Supplementary Figure. S3-10, Supplementary Note .1), and shown in Supplementary Figure. S3-10,11,12. The change of fraction of Ce^{3+} and Ce^{4+} was obtained from the linear combination fitting results with the most oxidised and reduced species as the internal standards. The examples of relative Ce^{3+} and Ce^{4+} fraction upon CO and O_2 pulse for Cu-CZ and CZ at 250°C is shown in Fig. 4b and Fig. 4c. The results upon multiple switches confirm the reproducibility of the experiments. 15%

Ce^{3+} presented in the Cu-CZ even under O_2 condition. CO reduces an additional 10% of Ce^{4+} at 250 °C. The same fitting is carried out for CZ, Pd-CZ and Cu-CZ across all the temperatures (Supplementary Fig. S3-11,12,13), with the OSC being calculated based on the reducible Ce^{3+}/Ce^{4+} content according to Eq. 2 OSC. These OSC determined from Ce^{3+}/Ce^{4+} content was then compared with those obtained by measuring the formation of CO_2 from the outlet of the reactor (Fig. 3-4d,e). These two OSCs obtained using different methods are similar. This confirms the reliability of the OSC measurement from Ce^{3+}/Ce^{4+} contents, and further confirms that it is possible to use this method to determine the Ce^{4+} reduction rate and Ce^{3+} oxidation rate, which is equivalent to the V_O formation rates and V_O conversion rate respectively.

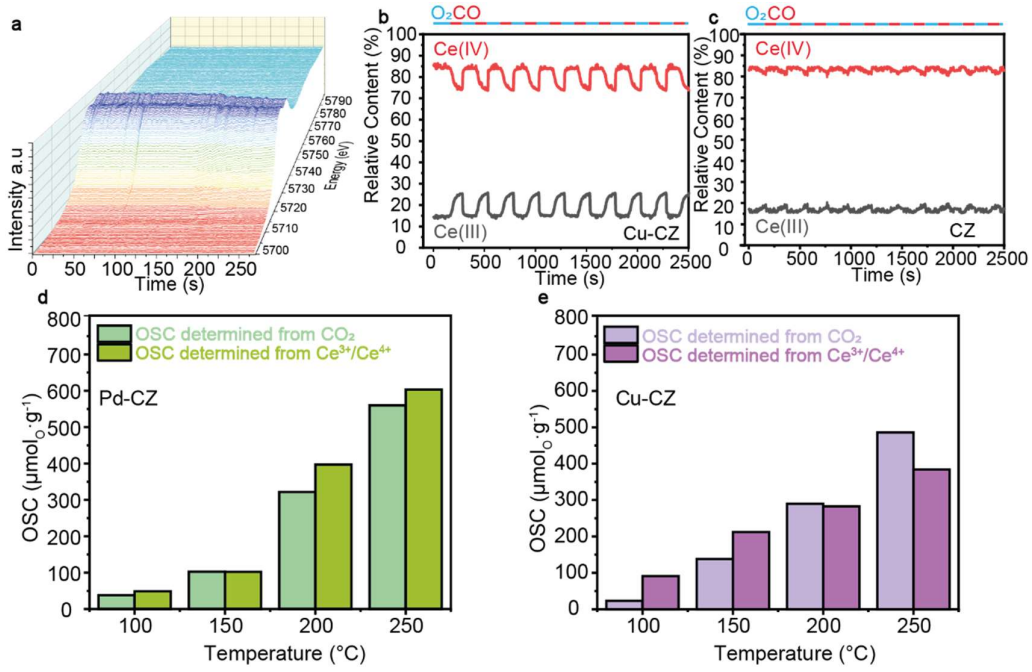

Figure 3-4. a. Time-resolved XANES of Ce L3-edge of one gas switch (from O_2 to CO); **b.** Relative content of Ce^{3+} and Ce^{4+} during 10 repetitions of gas switching for Cu-CZ at 150℃. **c**. Relative content of Ce^{3+} and Ce^{4+} during 10 repetitions of gas switching for Cu-CZ at 250℃. **d.** Calculated OSC from CO_2 and Ce^{3+}/Ce^{4+} for Pd-CZ. **e.** Calculated OSC from CO_2 and Ce^{3+}/Ce^{4+} for Cu-CZ.

The reduction rate of Ce^{4+} was calculated by the slope of the tangent line to the initial fraction of Ce^{3+} change curve, so as the oxidation rate (Fig. 3-5a). Clearly the Ce^{3+} oxidation rate is much faster than the Ce^{4+} reduction rate. On the basis the inlet CO and O_2 concentrations are 2 vol% and 2 vol% respectively, we can then determine the rate for Eq. 4 is 5.7 X 10^{-5} $mol_{Ce}{\cdot}s^{-1}{\cdot}g^{-1}$ 10 times higher than Eq. 3 6.7 X 10^{-6} $mol_{Ce}{\cdot}s^{-1}{\cdot}g^{-1}$ for Cu-CZ at 150 °C. Hence, the V_O formation rate is much slower than the V_O

conversion rate. Therefore, how fast the OSMs can provide the reactive O on the surface is the key to improving the catalytic performance. At temperatures below 250 °C, little reduction of Ce in pure CZ occurs, so the rate of reduction of Ce in CZ can be regarded near 0. The massive improvement of the rate of Ce reduction, also regarded to CO oxidation by lattice O, is due to the small loading amounts of Cu/Pd. At 250 °C, the Pd-CZ achieved the rate of 9.55×10^{-5} mol·s^{-1}·g^{-1} at 2% CO with a WHSV of 10,000 ml$_{CO}$/g·h. Based on our current knowledge, this is the first-time quantification of the V_O formation rate. Obtaining such rate at different temperature derives the activation energy (E_a). It can still be seen that Cu-CZ (36.5 kJ/mol) and Pd-CZ (58.39 kJ/mol) have much lower E_a than that of CZ (110.8 kJ/mol). This is a typical catalytic process that Pd and Cu here serve the concept of catalysis: by reacting with CO and Ce^{4+}, Pd and Cu pass the electrons from CO to Ce^{3+} and provide the neighbour O^{2-} to form CO_2. The newly formed V_O is then recovered via migration of O^{2-} species[15], which is consistent with the MvK mechanism for understanding of the CO oxidation with Ce based catalysts. The catalytic performance for CO oxidation by O_2 ·matches the kinetics study and the atom utility analysis (Fig. 3-5c). Pd-CZ shows the best CO conversion at low temperature: twice as good as Cu-CZ, where CZ shows no activity.

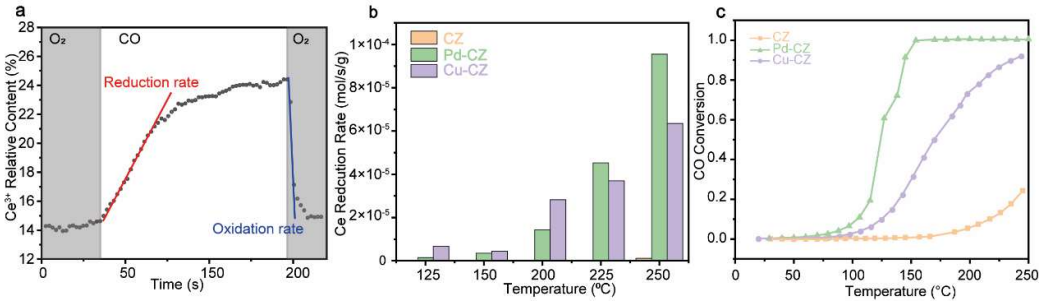

Figure 3-5. Kinetic study from time resolved energy dispersive XAFS. a. Evolution of Ce^{3+} concentration in Cu-CZ catalyst during gas switch experiments at 150 °C (average of 9 cycles). **b.** Ce reduction rate for Cu-CZ; Pd-CZ and CZ with temperature. **d.** catalytic performance of CO oxidation for CZ; Cu-CZ and Pd-CZ.

3.3.5 Discussion

With small amount of Cu/Pd loading, the kinetic of Ce reduction by CO was improved by accelerating the reaction rate by 50 times and decreasing the activation energy from 134.6 kJ/mol to 36.5 kJ/mol at 250 °C. So, Cu and Pd can also be regarded as a catalyst for Ce^{4+} reduction and V_O formation. The kinetic study by *operando*-EDE was compared with the kinetics of CO oxidation reaction (Fig. 3-6). Despite that Ce^{4+} reduction rate is measured with X-ray and CO oxidation rate is measured by online gas analyser, the calculated rates with the unit of mol·g^{-1}·s^{-1} form very similar kinetics plots

(Fig. 3-6a,b&c). Such comparison of partial reaction (eq.2&3) and full reaction (eq.1) kinetics is the first time in the world and clearly showing that V_O formation (eq.2&3) is the rate determine step in MvK mechanism for CO oxidation. By calculating the promoted reduced Ce atoms number by Cu/Pd single atom, the utility of 'catalytic' Cu/Pd atom can be compared (Supplementary Fig. S3-14). At temperature of 200 °C, Pd catalysed the reduction of 6.4 Ce^{4+} atoms whereas Cu catalysed only 3.2 Ce^{4+} atoms. As the temperature rises, the performance of Cu gradually catches up with that of Pd. With loading of small amount of Cu, the Ce-O-Ce bond will change to Ce-O-Cu bond which generally occurs on the surface of the particles where CO will be adsorbed. According to the calculation studies[31,32], the Ce-O-Cu bond is weaker than Ce-O-Ce bond, which leads to stronger CO adsorption and Ce-O bond breaking.

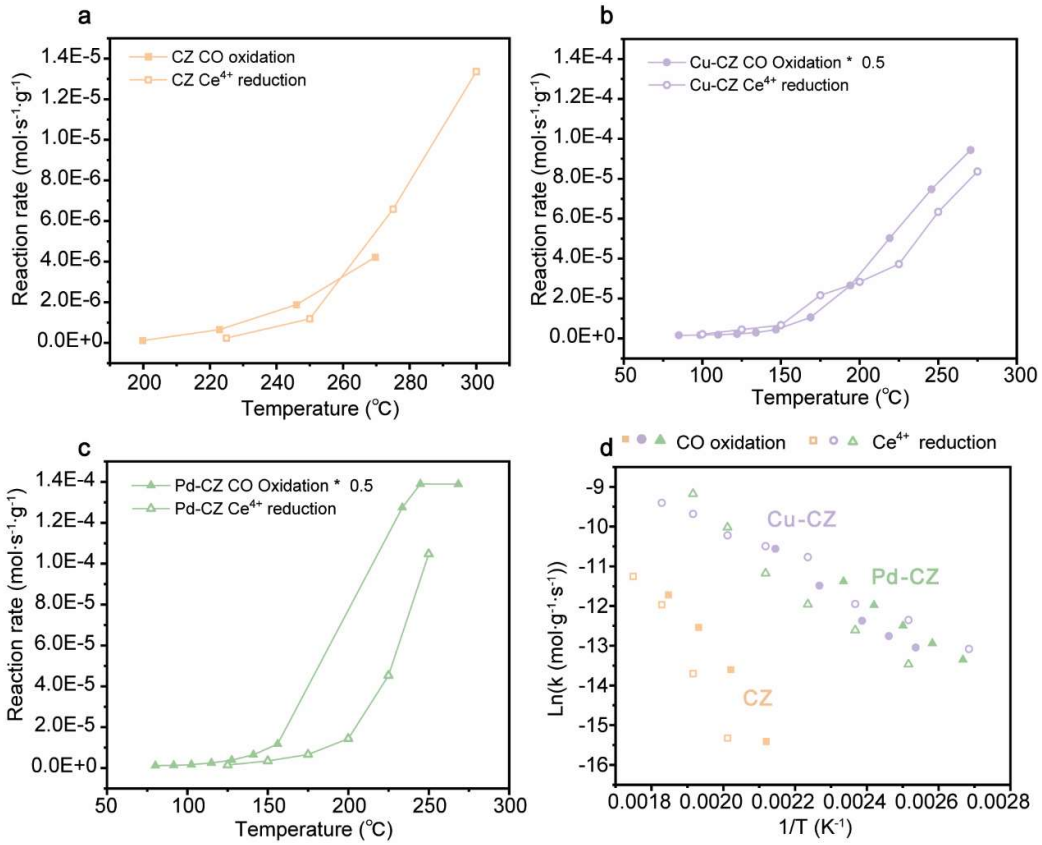

Figure 3-6. Kinetics comparison between Ce^{4+} reduction and CO oxidation. a. Comparison between reaction rate of Ce^{4+} reduction and CO oxidation for CZ. **b.** Comparison between reaction rate of Ce^{4+} reduction and CO oxidation for Cu-CZ. CO oxidation rate was multiplied by 0.5. **c.** Comparison between reaction rate of Ce^{4+} reduction and CO oxidation for Pd-CZ. CO oxidation rate was multiplied by 0.5. **d.** Arrhenius plot for CO oxidation and Ce redcution.

3.4 Conclusions:

In summary, by measuring the Ce^{4+} reduction/ Ce^{3+} oxidation rate at the beginning of the bed in fast EDE measurement, the accurate kinetics of V_O formation and conversion are achieved for the first time. Comparing such partial reaction rates with the full reaction rates reveals the rate-determining step in MvK mechanism to be the V_O formation. With highly dispersed Cu/Pd loading, not only the thermal dynamics OSC performance are significantly improve, but also the kinetics of V_O formation is massively enhanced by reducing the activation energy of the V_O formation reaction when loading with Cu/Pd. Such enhancement of the kinetics contributes to a higher reaction rate of CO oxidation as well as a better catalytic performance.

3.5 Methods

Sample preparation:

CeO_2-ZrO_2 (CZ) samples are prepared by the co-precipitation methods using $(NH_4)_2[Ce(NO_3)_6]$ and $ZrO(NO_3)_2 \cdot xH_2O$ as the precursors. The obtained precipitate was calcined in Air at 500℃ for 2 hours. 0.6wt%Cu and 1wt%Pd was dopped on the prepared CZ by wet-impregnation method using $Cu(NO_3)_2$ and $Pd(NO_3)_2$ as the precursors and deionized-water as the solvent. After the impregnation, the samples were calcined in Air at 500 ℃ for 2 hours.

Operando Time-resolved energy dispersive EXAFS (EDE)

Time resolved Energy Dispersive EXAFS (EDE) characterization was performed at I20-EDE beamline in Diamond Light Source[33,34]. Polychromatic beam ($\Delta E/E$=10%) was produced through a wiggler insertion device and focussed vertically using Rh/Pt coated silicon mirror. A band-pass mirror combined with a band-pass filter was used to select a sufficiently wide bandpass as well as to remove the heat load. A mechanically bent thin Si(111) polychromator crystal working in Bragg configuration was equipped to diffract the polychromatic X-rays[35]. The EDE spectra were collected in transmission mode using an 1028 pxl micro-strip Ge XH detector[36].
The experiment set-up is shown in Figure. 1a. For each experiment, 3mg of CZ sample powder diluted by 7mg hexagonal boron nitride (h-BN) was filled into a Kapton tube (3.0 mm inner diameter, 0.125 mm wall thickness). The loaded Kapton tube was then connected to the plug-flow reactor with a rotating gas adaptor, which can allow tube to rotate during an XAS measurement to have relatively homogeneous sample conditions (averaging of pin hole effects) for the better EDE measurement. The beam after the polychromator was focused on the side near the gas inlet side to avoid the gas diffusion effects and sensitively monitor the sample as soon as the gas is switched. The time resolution was 500ms per spectrum. XANES range collected for the Ce L3-edge was -150 eV ~ +200 eV around the edge. 20 vol% O_2 (5 sccm) and 10 vol% CO (5 sccm) diluted by Ar were used with the quick gas switch (WHSV=10,000 $ml_{CO}/g \cdot h$). The gas

switch can be done within 500ms (50ms switching time) which is well within one spectrum collection time. The gas switching between CO and O_2 was repeated more than 10 times to collect the repeatable results. The temperature of the reactor is set between RT and 250 °C using a PID eurotherm controlled TDK-Lambda power supply (1000 W). A CeO_2 pellet was measured before every set of experiments for energy calibration to correct the energy drift of polychromator. The data was processed by Dawn Diamond (version 2.26)[37], the data process software based on Larch. The energy calibration was first conducted, followed by the normalization (set the first peak of first derivative as the E_0; the pre-edge linear fitting between -150 eV and -35 eV relative to the edge position and the post-edge 2nd order polynomial fitted between 100 eV and 200 eV above the edge energy.

In-situ XAS

The in-situ XAS was conducted at beamline BL01B1 in Spring-8 (Japan). Both Ce K-edge and Zr K-edge were measured. Transmission mode (crystal: Si 311; energy resolution: $\Delta E/E=2\times10^{-4}$) with ionization chambers (for Ce K: ion chamber gas for i_0: 80 vol% Ar, 20 vol% Kr; ion chamber gas for i_t: 100 vol% Kr; for Zr K: ion chamber gas for i_0: 50 vol% Ar, 50 vol% Kr; ion chamber gas for i_t: 80 vol% Ar, 20 vol% Kr) were chosen as our experiment set-up. CeO_2; $Ce(NO_3)_3$; Zr foil and ZrO_2 were measured as the standard for energy calibration and data fitting. Sample was mounted on the in-situ heating cell. The temperature control was calibrated in measurement condition. Both XANES and EXAFS were measured for each condition. Data was processed by the Demeter patch (0.9.26) including Athena and Artemis[38]. Data processing including normalization and XANES analysis were carried out by Athena. Artemis was used to do the EXAFS fitting for coordination number of first shell coordination and the distance between the centre atom and coordination atom.

In-situ NEXAFS

In-situ NEXAFS was conducted at beamline B07C in Diamond Light Source. CO TPR for CZ samples was carried out in B07C. The X-ray is with an energy range from 110 to 2800 eV, falling within the soft X-ray range, and it emits a flux of 1 x 10^{10} photons/s. The experiment setup is equipped with a stationary interface flange that accommodates the entrance cone of the ambient-pressure electron energy analyzer, (SPECS Phoibos NAP-150 model). Sample was casted on the Au coated Si wafer by drop casting method. Ambient NEXAFS set-up was used to have maximum 30mbar gas atmosphere in the measurement chamber and the temperature was controlled by a K-type thermocouple and regulated by a PID controller. Both Auger electron yield (AEY) and total electron yield (TEY) were measured for Ce M edge (870eV-930eV) and Cu L edge (920-960eV).

Oxygen storage capacity measurement

Total amount of 60mg CZ catalyst was loaded in the fixed-bed flow reactor. 1%vol O_2 and 2%vol CO were introduced and alternated with total flow rate of 300ml/min by mass flow controller (WHSV=6,000 $ml_{CO}/g \cdot h$). The product was detected by ABB detector: for CO and O_2, electrochemical sensors were used; and for CO_2, infrared sensor was used. Oxygen storage capacity were studied in temperature range from 100ºC to 400ºC. At each temperature, O_2 was first introduced for fully oxidized the catalyst and then quickly switched to CO for 10mins until the reaction finished and repeat the gas switch for 5 times. The total oxygen storage capacity was calculated by integrating the amount of generated CO_2.

CO oxidation catalytic activity test

The CO oxidation reaction was evaluated in a fix-bed flow reactor. The inlet gas composition and flowrate were set by mass flow controllers. A typical reaction gas composition was: 1% CO, 10% O_2 and balanced He. The total flowrate of the gas mixture was 200 mL/min (WHSV=1,500 $ml_{CO}/g \cdot h$). Typically, 80 mg catalyst was placed in the reactor tube, and the outlet gas composition was detected by Continuous Gas Analyser (ABB). The reaction was studied between 298K to 523K. The reaction was maintained at each temperature point for 30 minutes to measure the product gas signal (CO_2) after reaching steady state.

CO oxidation catalytic kinetics study

The kinetics study for CO oxidation reaction was evaluated in a fix-bed flow reactor. The inlet gas composition and flowrate were set by mass flow controllers. The reaction gas composition was: 2% CO, 4% O2 and balanced He. The total flowrate of the gas mixture was 200 mL/min (WHSV=1,2000 mlCO/g·h). 10 mg catalyst was placed in the reactor tube, and the outlet gas composition was detected by Continuous Gas Analyser (ABB). The reaction was studied between 298K to 523K. The reaction was maintained at each temperature point for 30 minutes to measure the product gas signal (CO2) after reaching steady state.

XRD

Powder X-ray diffraction (PXRD) was conducted by the STOE STADI-P diffractometer with Cu source (Kα=1.5406Å; using 40kV and 30mA). The range of 2θ is from 20° to 80° with the step of 0.02°.

STEM and EDS

High-resolution studies utilizing aberration-corrected Annular Bright Field (ABF) and High Angle Annular Dark Field Scanning Transmission Electron Microscopy (HAADF-STEM) were conducted at the electron Physical Science Imaging Centre (ePSIC). The ABF and HAADF-STEM images were simultaneously captured using a

probe-corrected (JEOL-COSMO) JEM ARM 300CF (JEOL, Japan), operating at 300 kV. To prepare all samples, a minimal quantity of dry powder was scattered onto 400 mesh gold/copper grids that were supported by a lacey carbon film.

The results from Energy-Dispersive X-ray Spectroscopy (EDS) were gathered using a probe-corrected (CEOS) JEM ARM 200CF (manufactured by JEOL, Japan), which was operated at 200 keV. This device is outfitted with large solid-angle dual EDS detectors, designed for X-ray spectroscopy and elemental mapping. The acquisition of EDS data was executed in the STEM imaging mode. The mapping process incorporated spatial drifting correction every 30 seconds. The EDS spectrum imaging data acquisition was facilitated using the Gatan Microscopy Suite Software.

3.7 Reference

1 Li, P., Chen, X., Li, Y. & Schwank, J. W. A review on oxygen storage capacity of CeO2-based materials: Influence factors, measurement techniques, and applications in reactions related to catalytic automotive emissions control. *Catalysis Today* **327**, 90-115 (2019).

2 Lord, M. S., Berret, J. F., Singh, S., Vinu, A. & Karakoti, A. S. Redox active cerium oxide nanoparticles: current status and burning issues. *Small* **17**, 2102342 (2021).

3 Sugiura, M. Oxygen storage materials for automotive catalysts: ceria-zirconia solid solutions. *Catalysis Surveys from Asia* **7**, 77-87 (2003).

4 Zhou, Z. *et al.* Catalytic oxidation of Hg0 over Mn-doped CeO2-ZrO2 solid solution and MnOx/CeO2-ZrO2 supported catalysts: Characterization, catalytic activity and SO2 resistance. *Fuel* **310**, 122317 (2022). https://doi.org:https://doi.org/10.1016/j.fuel.2021.122317

5 Farooq, A. *et al.* Linear low-density polyethylene gasification over highly active Ni/CeO2-ZrO2 catalyst for enhanced hydrogen generation. *Journal of Industrial and Engineering Chemistry* **94**, 336-342 (2021). https://doi.org:https://doi.org/10.1016/j.jiec.2020.11.005

6 Al-Fatesh, A. S. *et al.* In situ auto-gasification of coke deposits over a novel Ni-Ce/W-Zr catalyst by sequential generation of oxygen vacancies for remarkably stable syngas production via CO2-reforming of methane. *Applied Catalysis B: Environmental* **280**, 119445 (2021). https://doi.org:https://doi.org/10.1016/j.apcatb.2020.119445

7 Sun, J. *et al.* Enhancement of oxygen exchanging capability by loading a small amount of ruthenium over ceria-zirconia on dry reforming of methane. *Advanced Powder Technology* **33**, 103407 (2022). https://doi.org:https://doi.org/10.1016/j.apt.2021.103407

8 Fornasiero, P. *et al.* Modification of the Redox Behaviour of CeO2Induced by Structural Doping with ZrO2. *Journal of Catalysis* **164**, 173-183 (1996). https://doi.org:https://doi.org/10.1006/jcat.1996.0373

9 Omata, T., Kishimoto, H., Otsuka-Yao-Matsuo, S., Ohtori, N. & Umesaki, N. Vibrational Spectroscopic and X-Ray Diffraction Studies of Cerium Zirconium Oxides with Ce/Zr Composition Ratio=1 Prepared by Reduction and Successive Oxidation of t'-(Ce0.5Zr0.5)O2 Phase. *Journal of Solid State Chemistry* **147**, 573-583 (1999). https://doi.org:https://doi.org/10.1006/jssc.1999.8420

10 Kašpar, J., Fornasiero, P. & Graziani, M. Use of CeO2-based oxides in the three-way catalysis. *Catalysis Today* **50**, 285-298 (1999). https://doi.org:https://doi.org/10.1016/S0920-5861(98)00510-0

11 Yuanqing, D. *et al.* A novel method for the synthesis of CexZr1-xO2 solid solution with high purity of κappa phase and excellent reactive activity. *Catalysis Today* (2019). https://doi.org:10.1016/j.cattod.2018.04.040

12 Yuanqing, D. *et al.* Superior catalytic activity of a Pd catalyst in methane combustion by fine-tuning the phase of ceria-zirconia support. *Applied Catalysis B-environmental* (2020). https://doi.org:10.1016/j.apcatb.2020.118631

13 Fei, D., Toshitaka, T., Naoki, T. & Hirofumi, S. Investigation of the effective oxygen storage and release performances on the Pt/CeO2-ZrO2 catalysts by breakthrough method. *Catalysis Today* (2019). https://doi.org:10.1016/j.cattod.2018.07.046

14 Yamamoto, T. *et al.* Origin and dynamics of oxygen storage/release in a Pt/ordered CeO2–ZrO2 catalyst studied by time-resolved XAFS analysis. *Angewandte Chemie International Edition* **46**, 9253-9256 (2007).

15 Kang, L. *et al.* Adsorption and activation of molecular oxygen over atomic copper (I/II) site on ceria. *Nature communications* **11**, 1-11 (2020).

16 Kang, L. *et al.* The Electrophilicity of Surface Carbon Species in the Redox Reactions of CuO-CeO2 Catalysts. *Angewandte Chemie* **133**, 14541-14549 (2021).

17 Fonseca, J. d. S. L. *et al.* Cooperative effect between copper and gold on ceria for CO-PROX reaction. *Catalysis Today* **180**, 34-41 (2012).

18 Cargnello, M. *et al.* Active and stable embedded Au@ CeO2 catalysts for preferential oxidation of CO. *Chemistry of Materials* **22**, 4335-4345 (2010).

19 An, Y., Shen, M. & Wang, J. Comparison of the microstructure and oxygen storage capacity modification of Ce0. 67Zr0. 33O2 from CaO and MgO doping. *Journal of alloys and compounds* **441**, 305-310 (2007).

20 Narayana, B. L., Mukri, B. D. & Ch, S. Mn ion substituted CeO2 nano spheres for low temperature CO oxidation: the promoting effect of Mn ions. *ChemistrySelect* **1**, 3150-3158 (2016).

21 Venkataswamy, P., Jampaiah, D., Rao, K. N. & Reddy, B. M. Nanostructured Ce0. 7Mn0. 3O2− δ and Ce0. 7Fe0. 3O2− δ solid solutions for diesel soot oxidation. *Applied Catalysis A: General* **488**, 1-10 (2014).

22 Safonova, O. V. *et al.* Elucidating the Oxygen Activation Mechanism on Ceria-Supported Copper-Oxo Species Using Time-Resolved X-ray Absorption Spectroscopy. *ACS Catalysis* **10**, 4692-4701 (2020). https://doi.org:10.1021/acscatal.0c00551

23 D'Angelo, A. M., Wu, Z., Overbury, S. H. & Chaffee, A. L. Cu-enhanced surface defects and lattice mobility of Pr-CeO2 mixed oxides. *The Journal of Physical Chemistry C* **120**, 27996-28008 (2016).

24 Wakita, T. & Yashima, M. In situ observation of the tetragonal-cubic phase transition in the CeZrO4 solid solution - A high-temperature neutron diffraction study. *Acta crystallographica. Section B, Structural science* **63**, 384-389 (2007). https://doi.org:10.1107/S0108768107007720

25 Duwez, P. & Odell, F. Phase relationships in the system zirconia—ceria. *Journal of the American Ceramic Society* **33**, 274-283 (1950).

26 Nagai, Y. *et al.* X-ray absorption fine structure analysis of local structure of CeO2–ZrO2 mixed oxides with the same composition ratio (Ce/Zr=1). *Catalysis Today* **74**, 225-234 (2002). https://doi.org:https://doi.org/10.1016/S0920-5861(02)00025-1

27 Nagai, Y. *et al.* Local structure analyses of Ce0.5Zr0.5O2 mixed oxides by XAFS. *Journal of Synchrotron Radiation* **8**, 616-618 (2001). https://doi.org:10.1107/s0909049500017520

28 Dura, O. J. *et al.* XANES and EXAFS study of the local order in nanocrystalline yttria-stabilized zirconia. *Physical Review B* **87**, 174109 (2013). https://doi.org:10.1103/PhysRevB.87.174109

29 Li, P., Chen, I. W. & Penner-Hahn, J. E. X-ray-absorption studies of zirconia polymorphs. II. Effect of Y2O3 dopant on ZrO2 structure. *Physical Review B* **48**, 10074-10081 (1993). https://doi.org:10.1103/PhysRevB.48.10074

30 Alexander, A. G. *et al.* Fluorescence-detected XAS with sub-second time resolution reveals new details about the redox activity of Pt/CeO2 catalyst. *Journal of Synchrotron Radiation* (2018). https://doi.org:10.1107/s1600577518005325

31 Polychronopoulou, K. *et al.* Design aspects of doped CeO2 for low-temperature catalytic CO oxidation: transient kinetics and DFT approach. *ACS applied materials & interfaces* **13**, 22391-22415 (2021).

32 Gupta, A., Waghmare, U. & Hegde, M. Correlation of oxygen storage capacity and structural distortion in transition-metal-, noble-metal-, and rare-earth-ion-substituted CeO2 from first principles calculation. *Chemistry of Materials* **22**, 5184-5198 (2010).

33 Diaz-Moreno, S. *et al.* The spectroscopy village at diamond light source. *Journal of synchrotron radiation* **25**, 998-1009 (2018).

34 Diaz-Moreno, S. *et al.* in *Journal of Physics: Conference Series*. 012038 (IOP Publishing).

35 Sutter, J., Amboage, M., Hayama, S. & Díaz-Moreno, S. Geometrical and wave-optical effects on the performance of a bent-crystal dispersive X-ray spectrometer. *Nuclear Instruments and Methods in Physics Research Section A: Accelerators, Spectrometers, Detectors and Associated Equipment* **621**, 627-636 (2010).

36 Headspith, J. *et al.* in *2007 IEEE Nuclear Science Symposium Conference Record.* 2421-2428 (IEEE).

37 Basham, M. *et al.* Data analysis workbench (DAWN). *Journal of synchrotron radiation* **22**, 853-858 (2015).

38 Ravel, B. & Newville, M. Data analysis for X-ray absorption spectroscopy using IFEFFIT. *Journal of synchrotron radiation* **12**, 537-541 (2005). https://doi.org:10.1107/S0909049505012719

Chapter 4

Dynamics of metal-support electron transfer between Cu and Ce by the shared O: an XFEL study

4.1 Abstract

Charge transfer is one of the main metal support interactions affecting the catalytic properties of rational catalysts. Although massive efforts have been made for verification and explanation for this phenomenon, the direct observation and dynamics study is the last piece of the puzzle for understanding such milestone concept for exploring the fundamentals of elementary reaction and surface catalysis. With soft XFEL in Pohang Accelerator Laboratory, we use ultra-fast XAS on Cu L3-edge and Ce M5-edge monitoring the electronic structure variations contributed by the photo-induced electron migration between Ce and Cu via the Ce-O-Cu bond. The dynamics of such charge transfer process is around 200-300 fs. By comparing the dynamics of intraband excitation (1-2 ps) and charge transfer, only a small part of the excited electron migrated to Cu. Even such a small amount of electron migration dramatically alters the transient electronic structure of the surface-dispersed Cu. This provides an additional reaction boost to the surface reactants adsorbed at the Cu sites.

4.2 Introduction

Since 1978[1], metal support interaction (MSI) has been introduced to describe the improvement of chemisorption properties for metals which supported on another metal oxide[2,3]. In general, the supports play a crucial role in enhancing the utilization efficiency of metal atoms, providing stability to the metal active species, and potentially engaging in catalytic processes to facilitate chemical reactions[4]. Additionally, supports can contribute to the overall effectiveness and performance of catalysts by influencing the dispersion and interactions of metal species, thereby impacting the catalytic properties and selectivity of the system. Researchers put massive efforts on SMSI explanation and rational catalysts design based on such phenomena[5-8]. According to Pacchioni[9] and van Deelen's[5] studies, the charge transfer is one of the main phenomena of metal support interaction. This phenomenon of electron redistribution, while exhibiting noticeable effects, is generally confined to a limited region near the interface, and its manifestation may coincide with alterations in the oxidation state of the metal atoms present in either the nanoparticle or the metal ions within the support material. The investigations on metals supported by TiO_2 revealed that metals can be bonded to TiO_2 and differences in the Fermi level between the metal nanoparticle and the supporting material play a pivotal role in determining both the magnitude and direction of the charge transfer phenomenon, which is primarily aimed at reaching a state of equilibrium in electron chemical potentials[10,11]. With more and more research on different materials, CeO_2 has been increasingly used in catalysts because of its special redox properties. The charge transfer between metals and CeO_2 plays an indispensable

role in rational design for different catalysis reactions[12,13]. Liqun and Bolun[14] proposed a concept of electronic metal–support–carbon interaction (EMSCI) has been introduced as a theoretical framework to elucidate the intricate reaction mechanism involved in the oxidation of CO (Equation.1). By incorporating the EMSCI model, researchers are able to gain a complete understanding of both the mass and electron transfer processes, thereby facilitating the accurate prediction and enhancement of catalytic efficiency. This approach proves particularly valuable in the realm of C1 chemistry, as it enables the selective activation of CO_2, carbonate, and carbonyl species, ultimately paving the way for advancements in catalytic applications.

$$Cu^0 + Ce^{4+} = Cu^+ + Ce^{3+} \qquad \text{Eq. 4-1}$$

However, this charge transfer phenomenon has never been observed directly from an experimental perspective, this is because that the electron movement is usually in extremely fast speed and normal characterization techniques do not have the suitable time resolution for that. Recently, ultrafast characterization was developed to help researchers observe the dynamics of transient state of materials in in-situ or even *operando* conditions[15,16]. In the meantime, x-ray spectroscopy from synchrotron facilities with its element selective and generous testing conditions are becoming more and more indispensable in the examination of catalysts, particularly in understanding the local environments and changes in electronic structures during catalytic reactions[17,18]. The newest generation light source with x-ray free electron laser (XFEL) shows crucial potential to capture the ultrafast transient state of materials elementally. Based on the use of this technique, we can directly observe the electron migration between the metal and support and analyse its dynamics. In this research, we use fs-XAS from Puhang Accelerator Laboratory XFEL investigating the photo-induced electron migration between Cu and Ce to show the experimentally evidence of charge transfer in metal support interaction.

4.3 Results and discussion

4.3.1 Steady-state redox behaviour of Cu and Ce

2wt% Cu was loaded on CeO_2 synthesised by a microemulsion method according to previous research[19], which has the highest catalysis performance for water-gas shift (WGS) reaction. The redox ability of Cu was investigated by this research showing that Cu species was very sensitive to the reaction environment leading to a more active stie for reactants adsorption and reaction. However, the redox behaviour of Ce has not been studied, which is also important because of the metal-support interaction affecting the catalysis properties. Here we use in-situ near edge x-ray fine structure spectroscopy (NEXAFS) to study the redox behaviour for both Cu and Ce. Highly sensitive Cu species can be seen on the surface of such materials as Cu^+ identified by the feature at 935 eV can be seen even at room temperature in both 30 mbar CO and UHV. With

temperature increasing, Cu^{2+} reduced to Cu^{+} gradually which can be seen in the grey part highlighted in Figure 4-1 a&b. UHV as a more reductive atmosphere under which Cu^{2+} was reduced entirely at 150 °C. As a comparison, the reduction of Cu^{2+} completed at 200 °C in 30 mbar CO. However, the reduction behaviour of surface Ce is not consistent with Cu. The shoulder peaks located in the range from 882 eV to 883 eV indicating the Ce^{3+} species. As shown in figure 4-1 e&f, little Ce was reduced at room temperature and the reduction of Ce showed a general delay compared to Cu. This is because of the electron transfer between Cu and Ce: the movement of electrons is observed as they transfer from carbon monoxide to copper (Cu), and subsequently proceed to cerium, demonstrating a dynamic flow of charge carriers between these elements[14]. More interestingly, under UHV where Cu was much easier to be reduced, it was not until the temperature rises to 150 °C that Ce begins to reduce. But in 30 mbar CO, Ce has already been reduced at 100 °C. This may because that in UHV, surface Cu could not get electron directly from outside. The reduction of Cu is caused by the re-movement of bonded O. What's more important is that these O atoms also bonded with Ce, the charge transfer blocked because of the transfer bridge was broken making Ce was more difficult to be reduced comparing with which in 30 mbar CO. After UHV reduction at high temperature, 1 bar CO_2 was introduced into the camber for adsorption. After that, re-vacuuming to UHV was induced for investigating the decomposition of adsorbed CO_2 on surface. The results were shown in figure 4-1 c&g. It can be seen that both Cu and Ce was re-oxidized by CO2, and getting reduced with temperature rising.

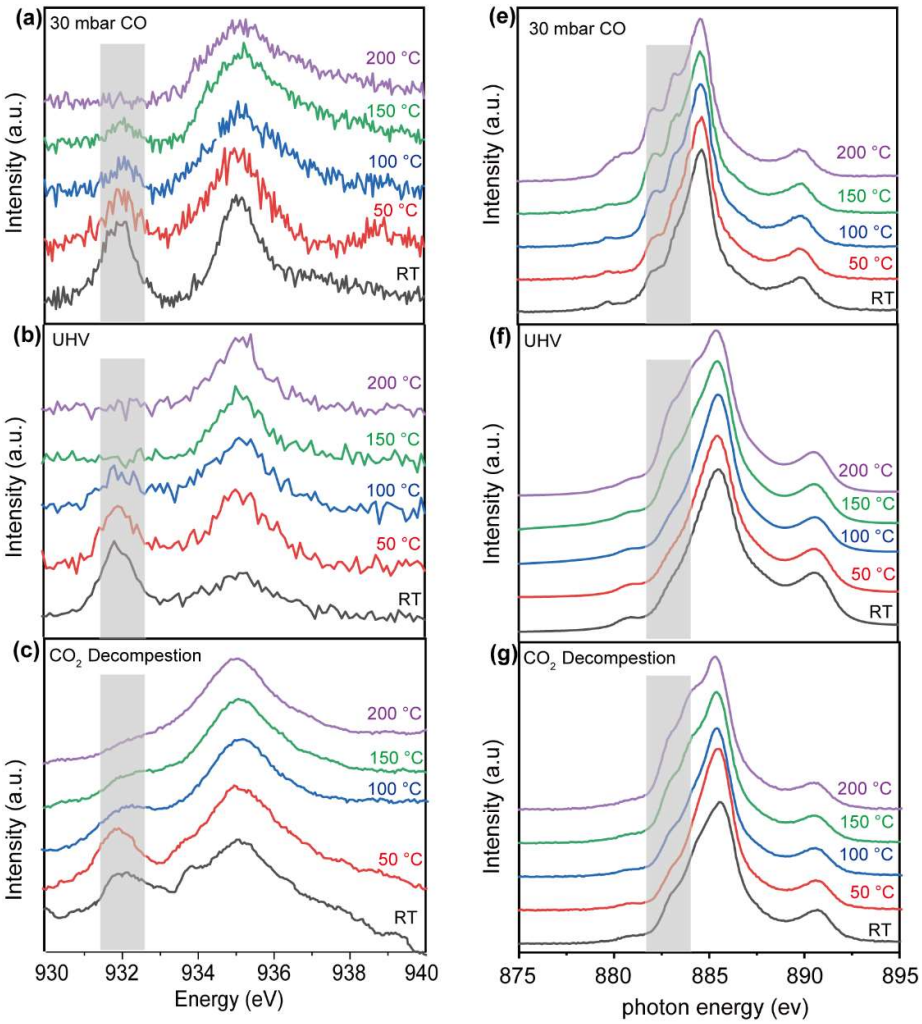

Figure 4-1. Steady state NEXAFS. a). Cu L3-edge NEXAFS in 30 mbar 100 vol% CO with increasing temperature. **b).** Cu L3-edge NEXAFS in UHV with increasing temperature. **c).** Cu L3-edge NEXAFS in UHV after adsorption in 1 bar 100 vol% CO_2. **d).** Ce M5-edge NEXAFS in 30 mbar 100 vol% CO with increasing temperature. **e).** Ce M5-edge NEXAFS in UHV with increasing temperature. **f).** Ce M5-edge NEXAFS in UHV after adsorption in 1 bar 100 vol% CO_2.

4.3.2 XAS with XFEL

To study the charge transfer between metal and support, fs XAS with XFEL was used to achieve the ultra-high time resolution and elementary investigation. The schematic of measurement set-up is shown in figure 4-2. 30Hz 267nm optical laser was used to excite the sample, and with certain time delay(Δt), 60Hz XFEL will measure the ground state (before laser) and the excited state (after laser). The beam size for optical laser is larger than XFEL to make sure the measurement can fully cover the excited samples. Since the high repetition of optical laser and XFEL, the sample under double focused may explore. A raster scan set-up was built to make sure that each pump probe should be at fresh samples. We set the position at the top of new column (supplementary Figure

4-1a), then changed the monochromator energy to 929eV (pre-peak). 30Hz 267nm optical laser was used to excite the sample, and with certain time delay(Δt), 60Hz XFEL will measure the ground state (before laser) and the excited state (after laser) at pre-set energy position. After one pump-probe finished, the beam focus will move dawn sample position by 400um vertically to reach the fresh sample and run the measure again. 100 measurements were performed by changing the sample position and the intensity was averaged.

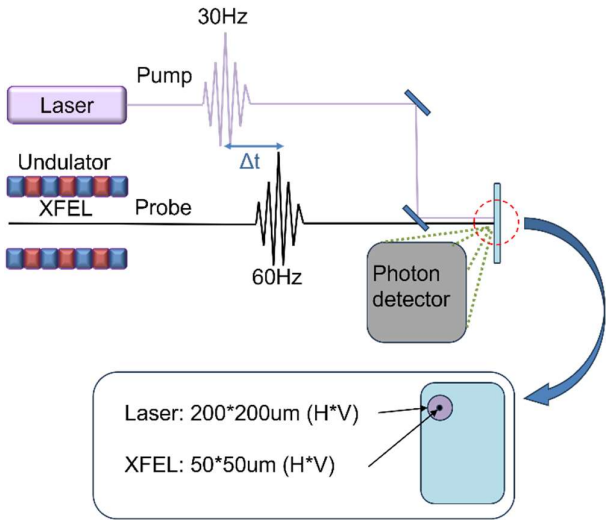

Figure 4-2. Schematic of XFEL set up for raster scan XAS measurement.

4.3.3 Dynamics of Cu^{2+} reduction under UHV.

Cu L3-edge XAS was firstly measured. The Cu L3 XAS spectra after exposure to optical laser with 266nm wavelength and 25 mJ/cm2 power was shown in Supplementary Fig.5-1b. With the increased exposure time, intensity of Cu^{2+} decreased while intensity of Cu^{+} increased showing the solid evidence of the reduction of Cu^{2+} by 267nm laser. And with higher power laser exposure, the more Cu^{2+} can be reduced with single shot (Supplementary Fig.4-1c). To verify the feasibility of detecting dynamics of Cu reduction, 6 energy position were chosen to have the relative complete Cu^{2+} feature peak from 927 eV to 932 eV. And the comparison before and after one single laser exposure is shown in Fig.4-3a. With 0.5ps delay, the intensity at 930 eV decreased showing the reduction of Cu^{2+}. With fixed XFEL energy with 930 eV, the normalized intensity changes with different delay time between optical laser and XFEL pulses is shown in Fig. 4-3b and c. The intensity change is 0 when measuring the ground state before laser exposure, and the duration of the reduction of Cu^{2+} can be estimated by tracking the change of -ΔXAS. As Fig. 4-3b shows, 50 ps after exposure to optical laser, the intensity of 930 eV were relatively stable indicating that there was no reoxidation of Cu^{+} in UHV. The magnified view for the first 3 ps after laser exposure is shown in

Fig. 4-3c. There is a sharp decrease of 930eV intensity after the laser exposure and tends towards constant after 2ps, which indicating that the reduction of Cu^{2+} to Cu^{+} was completed within 2ps. Since the 267 nm laser cannot directly excite the electron from valence band to conduction band, the reduction of Cu can either caused by heating by laser or electron transfer from coordinated elements. And the laser-induced heat transfer is generally slow[20]. So, the main reason for Cu reduction after 267 nm laser irradiation should be the electron transfer from Ce. To verify this, Ce M5-edge XAS needed to be measured.

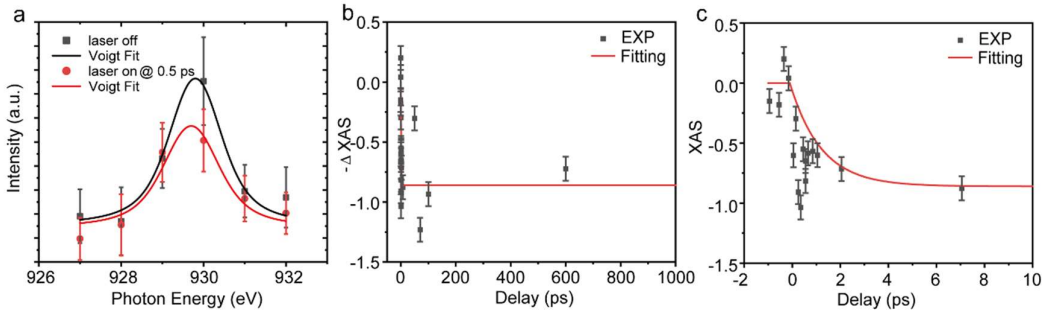

Figure 4-3. XAS spectra of Cu L3-edge by XFEL. a). Overview of the Cu L3-edge XAS spectra for ground state (black) and 0.5 ps after 267 nm laser irradiation (red). **b).** Temporal profile for intensity changing at 930 eV. **c).** -2 to 10 ps magnified view for temporal profile for intensity changing at 930 eV.

4.3.4 Dynamics of laser-induced Ce reduction

Similarly, we measured Ce M5-edge XAS with XFEL under same condition as Cu L3-edge. There are two main features in Ce M5-edge XAS: the shoulder peak at 994 eV representing the electron transition of $3d^{10}\,4f^{1} \rightarrow 3d^{9}\,4f^{2}$ which can only be observed in Ce^{3+}, and main peak at 996.8 eV representing $3d^{10}\,4f^{0} + 3d^{10}\,\underline{L}4f^{1} \rightarrow 3d^{9}\,4f^{1} + 3d^{9}\,\underline{L}4f^{2}$ transition[21]. It can be seen that after 0.2 ps laser irradiation, the shoulder peak at 994 eV increased, and went back to ground state after 3 ps, indicating that there is a small amount of Ce was reduced to Ce^{3+}: more density of $3d^{10}\,4f^{1}$ generated. But this part of reduced Ce^{3+} is not stable and went back to $3d^{10}\,4f^{2}$ representing Ce^{4+} after 3 ps. And for the main peak at 996.8 eV, the intensity first dropped and then gradually returned. This is caused by that the 267 nm pump excites the electrons from CeO_2 valence band to the conduction band increasing the density of $4f^{1}$ and $\underline{L}4f^{2}$.

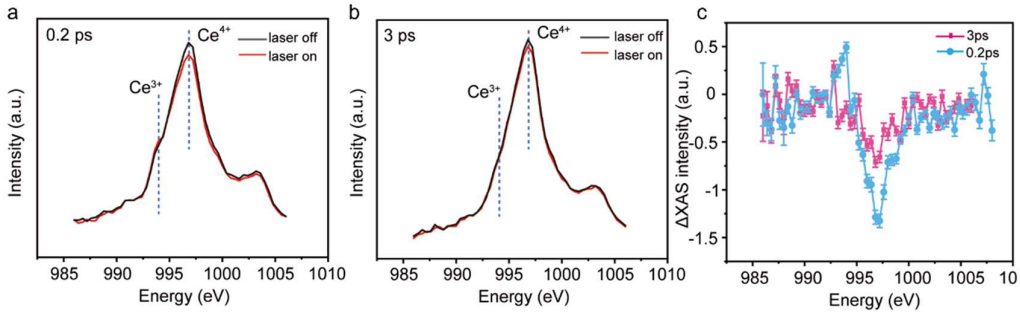

Figure 4-4. XAS spectra of Ce M5-edge by XFEL. a). Overview of the Ce M5-edge XAS spectra for ground state (black) and 0.2 ps after 267 nm laser irradiation (red). **b).** Overview of the Ce M5-edge XAS spectra for ground state (black) and 3 ps after 267 nm laser irradiation (red). c). Transient spectra of Ce M5-edge XAS for 0.2 ps and 3 ps after 267 nm laser irradiation.

The temporal profile for intensity changing at 994 eV and 996.8 eV is shown in Figure 4-5. The intensity of shoulder peak at 994 eV reached highest position in 145 fs, which indicating the increasing of $4f^1$ could not go further after with 267 nm laser irradiation. After this, the density of $4f^1$ went back to $4f^0$ in 1.42 ps. This phenomenon observed involves the common occurrence of intrabond excitation where electrons move from the valence band to the conduction band. Nevertheless, the rise in $\underline{L}4f^2$ lasting 270fs due to intrabond excitation does not promptly return to the ground state. This observation leads to the conclusion that some of the excited electrons in the conduction band relocate to Cu through the co-bonded Oxygen. Consequently, the dynamics of transient state play a crucial role in understanding the migration of electrons within the material.

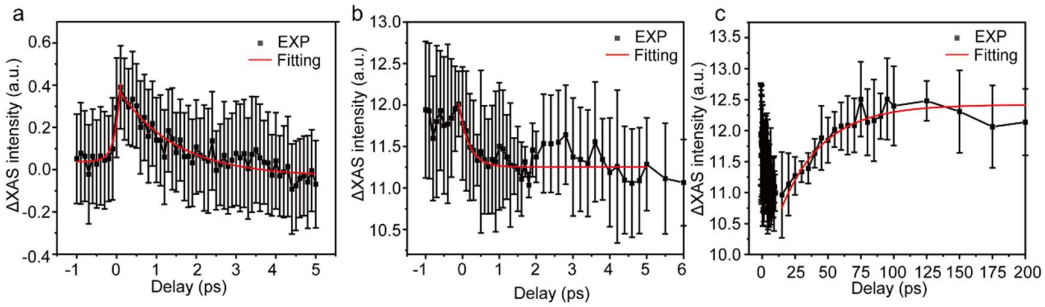

Figure 4-5. **a).** Temporal profile for intensity changing at 994 eV for Ce M5-edge XAS. **b).** -2 to 6 ps magnified view for temporal profile for intensity changing at 996.8 eV. **c).** Temporal profile for intensity changing at 996.8 eV for Ce M5-edge XAS.

4.3.5 discussion

Comparing the dynamics of the transient state observed in Cu L3-edge XAS with that of Ce M5-edge XAS allows for a comprehensive illustration of the entire electron

transfer process. Following the exposure to 267nm laser irradiation, the process of electron excitation originating from the Ce valence band and transitioning to the conduction band occurs within a remarkably short timeframe ranging from 150 fs to 270 fs. Subsequently, the majority of these excited electrons undergo a transition back to the valence band, leading to the decay of this transient state within a mere 1.42 ps, a phenomenon clearly depicted in the temporal profile showcasing intensity variations at 994 eV of Ce M5-edge XAS. Interestingly, a minor fraction of the excited electrons proceeds to migrate towards the Cu element through the co-bonded O, resulting in the reduction of Cu^{2+} to Cu^{+}, a transformation supported by the observed decrease in intensity at 930 eV of Cu L3-edge XAS. This reduction is further corroborated by the persistent presence of the transient electronic state of Cu2+ and the $\underline{L}4f^{1}$of Ce. Remarkably, the entire electron transfer process from Ce to Cu unfolds swiftly, taking a mere 1.5 ps to complete its course.

4.4 Conclusion

Charge transfer represents a crucial aspect of the primary metal support interactions that significantly influence the catalytic characteristics of rational catalysts. The verification and elucidation of this phenomenon have been subjects of extensive research efforts. However, the direct observation and in-depth dynamics study stand as the ultimate components required to complete the puzzle of comprehending this pivotal concept and delving into the foundational aspects of elementary reactions and surface catalysis. Utilizing the soft XFEL available at the Pohang Accelerator Laboratory, researchers engage in the application of ultra-fast XAS techniques focused on the Cu L3-edge and Ce M5-edge. These methods enable the monitoring of variations in the electronic structure attributed to the photo-induced electron migration between Ce and Cu through the Ce-O-Cu bond. The timescale associated with this charge transfer process approximately ranges between 1 to 2 ps. When juxtaposed with the dynamics of intraband excitation, which spans from 150 to 270 fs, it becomes evident that only a fraction of the excited electrons undergo migration towards Cu. Nevertheless, even this minute transfer of electrons leads to a significant transformation in the transient electronic configuration of the surface-dispersed Cu. Consequently, such alterations provide an additional catalytic boost to the surface reactants that are adsorbed at the Cu sites.

4.5 Methods

2 wt% Cu-CeO2 nanosphere synthesis

In 500 mL 2-neck flask, a mixture of n-heptane 200 mL, butanol 8 mL, and Triton X-100 8.87 g was conducted sonication for 10 min. and stirred for another 30 min. at room temperature. 2 mL of 0.5 M $Ce(NO_3)_3{\cdot}6H_2O$ ($Ce(NO_3)_3{\cdot}6H_2O$ 0.432 g + H_2O 2 mL) was slowly added to the mixture solution and 2 mL of 25% TMAH

(Trimethrylphenylammonium hydroxide solution) was also slowly added. After the mixture solution was stirred for another 24h, the formed yellow precipitate was collected by removing the solvent and the precipitate was washed with MeOH for several times. The residual solvent was removed by centrifugation (4000 rpm, 10min.). The precipitate was washed again with MeOH using centrifugation (4000 rpm, 10min.) for three times. The precipitate was dried in oven at 100℃ for overnight. (The yellow precipitate was changed to dark brown color). The dark brown precipitate was baked at 500℃ for 2h in the furnace. The dark brown precipitate was changed to yellow color again.

CeO_2 0.4 g was added to DI water 10 mL containing beaker and the CeO_2 was dispersed by sonication for 30 min. $Cu(NO_3)_2 \cdot 2.5\ H_2O$ 31.8 mg was added in the CeO_2 dispersed solution and stirred for 10 min. Na_2CO_3 250 mg was added to another DI water 5 mL containing beaker and the solution was sonicated for 30 min. Solution from previous steps were mixed and the mixed solution was stirred for 2h. And the solution was removed by centrifugation (4000 rpm, 10min.) and washed with DI water using centrifugation (4000rpm, 10min.) for three times. The precipitate was washed again with hot DI water by using reduced pressure filtration. In addition, the solid powder was dried in oven at 60℃ for overnight. The solid powder was reduced by H_2 and Ar mixture gas (H_2 ratio : 5%) at 250℃ for 1h using furnace system.

NAP-NEXAFS

In-situ NAP-NEXAFS analysis was performed at beamline B07C situated within the esteemed Diamond Light Source facility. The investigation of CO temperature-programmed reduction (TPR) for CZ samples was executed at the same B07C beamline. The X-ray beam utilized in this study encompasses an energy spectrum ranging from 110 to 2800 electron volts, thus falling under the category of soft X-rays, and boasts an impressive photon flux of 1 x 1010 photons per second. Within the experimental configuration, there is a fixed interface flange that is specifically designed to accommodate the entry cone of the ambient-pressure electron energy analyzer, known as the SPECS Phoibos NAP-150 model. The sample under scrutiny was meticulously deposited onto an Au-coated silicon wafer utilizing the well-established drop-casting technique, ensuring optimal sample preparation. Employing the ambient NEXAFS setup facilitated the maintenance of a gas atmosphere of up to 30 millibars within the measurement chamber, with the temperature meticulously regulated through the utilization of a K-type thermocouple and a PID controller. Comprehensive measurements were conducted for both the Auger electron yield (AEY) and the total electron yield (TEY) concerning the Ce M-edge (ranging from 870 electron volts to 930 electron volts) and the Cu L-edge (spanning from 920 electron volts to 960 electron

volts), providing a detailed insight into the electron behaviour and interactions within the samples at hand.

Fs-XAS with XFEL

Fs-XAS was performed in beam line SSS, Pohang Accelerator Laboratory XFEL facility. Samples were loaded on rectangular Si wafers (2.4 cm × 20 cm) uniformly. The sample was dispersed in pure D.I. water using sonication. (2g/1000ml). Si wafer is loaded on the four rod tip (1cm height) in the plastic chamber, which is equipped a small stopper on the bottom. Very slowly pour the dispersed solution into the chamber (not direct on the Si wafer, using the wall). The dispersed solution in the chamber is very slowly removed by using opening the stopper. It took a day (24h) to remove the solution. Then, the sample is very gently loaded on the Si wafer. And drying the sample in the dark chamber (slowly evaporate the water to prevent the crack). The measurement set-up is shown in Figure 5-2. 30 Hz 267nm laser with 120 fs duration was used as the pump while 60 Hz XFEL was used to measure the ground state and excited state of samples before and after the laser pump. The beam size for optical laser was 200 × 200 μm (H × V), and for XFEL was 50 × 50 μm (H × V) to make the probing fully cover the explored aera of samples. A specialized raster scan configuration was meticulously constructed with the primary objective of ensuring that every pump probe would be directed towards newly prepared samples. Once a pump-probe cycle was completed, the focal point of the beam would be systematically shifted downwards by 400 μm along the vertical axis to access a pristine sample, facilitating the commencement of a new measurement cycle. In the course of this experimental procedure, a total of 100 measurements were meticulously carried out by systematically altering the sample's position, followed by the subsequent computation of the average intensity recorded during these measurements. Several optical power density was chosen to investigate the intensity dependency for photo-induced reduction of Cu. The dynamics for both Cu L3-edge and Ce M5-edge were measured by 32.1 mJ/cm^2 power density of 267 nm laser, which is within the single photo-excitation region and have enough excitation for observation. Auger-electron yield was measured for both Cu L3-edge and Ce M5-edge NEXAFS under 10^{-8} torr at room temperature by electron energy analyser (Scienta, R3000) [22]. Precise synchronization between the X-ray and pump laser was achieved by using a pump probe experiment on a YAG crystal[23] or a 500-nm-thick Si_3N_4 film on Si[24]. The detailed of timing calibration can be seen in reference 22[22].

4.7 Reference

1 Tauster, S., Fung, S. & Garten, R. L. Strong metal-support interactions. Group 8 noble metals supported on titanium dioxide. *Journal of the American Chemical Society* **100**, 170-175 (1978).

2 Tauster, S. Strong metal-support interactions. *Accounts of Chemical Research* **20**, 389-394 (1987).

3 Tauster, S., Fung, S., Baker, R. & Horsley, J. Strong interactions in supported-metal catalysts. *Science* **211**, 1121-1125 (1981).

4 Luo, Z., Zhao, G., Pan, H. & Sun, W. Strong metal–support interaction in heterogeneous catalysts. *Advanced Energy Materials* **12**, 2201395 (2022).

5 van Deelen, T. W., Hernández Mejía, C. & de Jong, K. P. Control of metal-support interactions in heterogeneous catalysts to enhance activity and selectivity. *Nature Catalysis* **2**, 955-970 (2019).

6 Lou, Y. *et al.* Metal-support interaction for heterogeneous catalysis: from nanoparticles to single atoms. *Materials Today Nano* **12**, 100093 (2020).

7 Zecevic, J., Vanbutsele, G., de Jong, K. P. & Martens, J. A. Nanoscale intimacy in bifunctional catalysts for selective conversion of hydrocarbons. *Nature* **528**, 245-248 (2015).

8 Ahmadi, M., Mistry, H. & Roldan Cuenya, B. Tailoring the catalytic properties of metal nanoparticles via support interactions. *The Journal of Physical Chemistry Letters* **7**, 3519-3533 (2016).

9 Pacchioni, G. & Freund, H.-J. Controlling the charge state of supported nanoparticles in catalysis: lessons from model systems. *Chemical Society Reviews* **47**, 8474-8502 (2018).

10 Chen, M. & Goodman, D. The structure of catalytically active gold on titania. *science* **306**, 252-255 (2004).

11 Goodman, D. Model catalysts: from imagining to imaging a working surface. *Journal of Catalysis* **216**, 213-222 (2003).

12 Yu, W.-Z. *et al.* Construction of Active Site in a Sintered Copper–Ceria Nanorod Catalyst. *Journal of the American Chemical Society* **141**, 17548-17557 (2019). https://doi.org:10.1021/jacs.9b05419

13 Kang, L. *et al.* Adsorption and activation of molecular oxygen over atomic copper (I/II) site on ceria. *Nature communications* **11**, 1-11 (2020).

14 Kang, L. *et al.* The Electrophilicity of Surface Carbon Species in the Redox Reactions of CuO-CeO2 Catalysts. *Angewandte Chemie* **133**, 14541-14549 (2021).

15 Nilsson, A. *et al.* Catalysis in real time using X-ray lasers. *Chemical Physics Letters* **675**, 145-173 (2017).

16 Öström, H. *et al.* Probing the transition state region in catalytic CO oxidation on Ru. *Science* **347**, 978-982 (2015).

17 Zimmermann, P. *et al.* Modern X-ray spectroscopy: XAS and XES in the laboratory. *Coordination Chemistry Reviews* **423**, 213466 (2020).

18 Cutsail Iii, G. E. & DeBeer, S. Challenges and Opportunities for Applications of Advanced X-ray Spectroscopy in Catalysis Research. *ACS Catalysis* **12**, 5864-5886 (2022). https://doi.org:10.1021/acscatal.2c01016

19 Yao, S. *et al.* Morphological effects of the nanostructured ceria support on the activity and stability of CuO/CeO 2 catalysts for the water-gas shift reaction. *Physical Chemistry Chemical Physics* **16**, 17183-17195 (2014).

20 Brongersma, M. L., Halas, N. J. & Nordlander, P. Plasmon-induced hot carrier science and technology. *Nature nanotechnology* **10**, 25-34 (2015).

21 Paidi, V. K., Brewe, D. L., Freeland, J. W., Roberts, C. A. & van Lierop, J. Role of Ce 4 f hybridization in the origin of magnetism in nanoceria. *Physical Review B* **99**, 180403 (2019).

22 Park, S. H. *et al.* PAL-XFEL soft X-ray scientific instruments and X-ray optics: First commissioning results. *Review of Scientific Instruments* **89** (2018).

23 Sanchez-Gonzalez, A. *et al.* Coincidence timing of femtosecond optical pulses in an X-ray free electron laser. *Journal of Applied Physics* **122** (2017).

24 Eckert, S. *et al.* Principles of femtosecond X-ray/optical cross-correlation with X-ray induced transient optical reflectivity in solids. *Applied Physics Letters* **106** (2015).

Chapter 5

In Situ XAFS Observation of Transient Ligand-Coordinated Pd0 Complex for Pd nucleation

5.1 Abstract

A mechanistic understanding of metal cation reduction with controlled nanoparticle morphology is crucial in designing high-performance materials for catalysis, energy, optical and medical applications. Alongside the extensive theoretical literature on nanoparticle synthesis, detailed experimental evidence is required to verify and further observe nucleation and growth processes. In particular, the formation of a transient species is often suggested but is rarely experimentally measured. We present a combination of *in situ* X-ray absorption fine structure (XAFS) and *in situ* small angle X-ray scattering (SAXS) data during Pd nanoparticle formation to monitor chemical and physical changes simultaneously and determine intermediate Pd^0 species with a time resolution of 500 milliseconds. Distinct reduction, nucleation, growth, and reoxidation-dominated stages are identified in the growth profile of CTAC-capped porous Pd nanospheres. Chlorine-coordinated Pd^0 (Pd^0-Cl) is identified as the growth species, with peak concentrations of approximately 6.72 mM. When Pd seeds are introduced to the system, the Pd^0-Cl concentration peaks at 5.73 mM without a nucleation stage. The rate of Pd^0-Cl formation was found to be temperature dependent, and the activation energy of Pd nucleation was calculated as 22.59 kJ/mol. Results fit closely to a population-balanced precipitated growth model in which nucleation is continuous and soluble Pd^0 is the growth species. This combination of *in situ* XAFS and SAXS could later be applied to a range of transition metal systems, capturing the growth kinetics of reactants and transient species, as a step towards rational nanoparticle design.

5.2 Introduction

Morphology is a determining factor in the exceptionally high catalytic activity shown by Pd nanoparticles in ORR and organic cross-coupling reactions, among others.[1-6] To control nanocatalyst morphology, substantial empirical research has pinpointed key synthetic parameters which determine shape and size during the precipitated growth.[7-

[14] Controls such as temperature,[7,11] concentration,[15] chemical surface control agents (surfactants),[9,14,16] and seed solutions[17,18] are adjusted via trial-and-error to fine-tune catalytic properties. However, a deeper fundamental understanding of the effect of these synthetic parameters on the growth mechanism is required to eventually reach the goal of rational nanoparticle design.

The reduction of metal precursor solutions in the formation of metal nanoparticles provides a unique system to identify the nucleation species and reduction pathway. Catalytically active Pd nanoparticles, for example, may be hypothetically obtained from a Pd^{2+} precursor *via* either reduction within solution to a soluble Pd^{0} complex, or the formation of $Pd^{2+/1+}$ conjugates before direct reduction to metallic Pd. Theoretical investigations of a range of precipitated Pd nanoparticle growth systems have variously suggested Pd^{1+} coordinated intermediates,[19] zero-valent Pd^{0} monomers and ligand-mediated Pd^{0} as primary building blocks for nanoparticle nucleation and growth.[20-22] The understanding and identification of the key nucleation intermediates is the first step towards developing processes able to rationally control particle morphology. Experimental *in situ* characterization techniques including small-angle X-ray scattering (SAXS), X-ray absorption fine structure (XAFS), transmission electron microscopy (TEM) and ultraviolet-visible spectroscopy (UV-vis), among others, have been successfully combined to observe growth kinetics.[22,23] Pd nanoparticle reduction with ascorbic acid is widely believed to follow the Watzky-Finke two-step 'auto-catalytic' growth.[22,24-26] However, some debate remains about the intermediate stages and growth precursors, and their effect on morphology. The formation of a ligand-coordinated M^{0} growth species is considered most likely, since the presence of isolated atoms is energetically unfavourable.[27]

Capturing time-resolved intermediate growth species is experimentally challenging due to their transient nature and shared properties with either precursor or reaction products. A study of 1 nm Pd nanoparticle growth with a combination of SAXS and XAFS by Karim et al., while giving insight into the role of surfactants in nanoparticle growth,

predicts the formation of ligand coordinated Pd^0 as growth species within the solution; however, these species are not directly measured.[22] Alternatively, the formation of M_{4-6} growth units is possible, as observed in Rh nanocube synthesis where Rh_{4-6} growth species are chlorine coordinated.[23] The concentration of intermediate reduced species, such as soluble Pd^0 species, can also confirm the 'solution reduction' previously reported by Yang et al. with $PdCl_4^{2-}$ precursor, as opposed to 'surface reduction' observed for $PdBr_4^{2-}$.[28]

Here, we present a 500 millisecond resolved *in situ* XAFS and SAXS study of the ascorbic acid (AA) reduction of K_2PdCl_4 under a range of temperatures and seed concentrations. Cetyltrimethylammonium chloride (CTAC), was selected as the surfactant to form single-crystal porous nanoparticles, observe ligand-mediated reaction kinetics and detect growth species.[29] Previous observations of CTAC-capped Pd nanoparticle growth have demonstrated nucleation and autocatalytic growth stages, fitting the Watzky Finke (WF) two-step mechanism.[20,22,26] Applied to this system, the reaction is believed to have four principal stages.

Reduction:	$Pd^{2+} + 2e^- \rightarrow Pd^0$	Eq.5-1
Nucleation:	$nPd^0 \rightarrow (Pd^0)_n$	Eq.5-2
Growth:	$Pd^0 + (Pd^0)_n \rightarrow (Pd^0)_{n+1}$	Eq.5-3
Reoxidation:	$Pd^0 - 2e^- \rightarrow Pd^{2+}$ (solution)	Eq.5-4

First, the reduction of Pd^{2+} to Pd^0 (Equation 5-1), occurs by definition before the formation of Pd-Pd bonds or solid particles. Nucleation (Equation 5-2) follows with the first appearance Pd-Pd bonds, when growth species aggregate and reach a critical size to form 'nuclei'. WF two-step theory combines reduction and nucleation in the first pseudo-elementary step since unbonded Pd^0 does not have an equilibrium.[20,21] During

rapid growth (Equation 5-3) Pd growth species are incorporated onto an existing solid surface either from solution or *via* direct reduction at the surface. The decrease in Pd^0 concentration at long reaction times is attributed to either reoxidative dissolution (Equation 4), reshaping or etching, which are known to occur in systems containing halide ligands, particularly in the synthesis of Cl^- capped palladium nanoparticles with Cl^-/O_2 pair.[29,30]

The reaction setup (Fig. 5-1a) allows continuous spectroscopic measurements (Fig. 5-1b) and uniform automated solution injection to observe growth *in situ*. Five key parameters are experimentally measured during nanoparticle growth to distinguish reaction stages and test a theoretical model, namely Pd^{2+} concentration, Pd^0 concentration, Pd-Cl coordination, Pd-Pd coordination, and nanoparticle radius. SAXS records the growing radius of the nanoparticle, while XAFS results capture temporal changes in oxidation states of palladium (Pd^0 and Pd^{2+}), and Pd coordination (Pd-Pd and Pd-Cl/O).

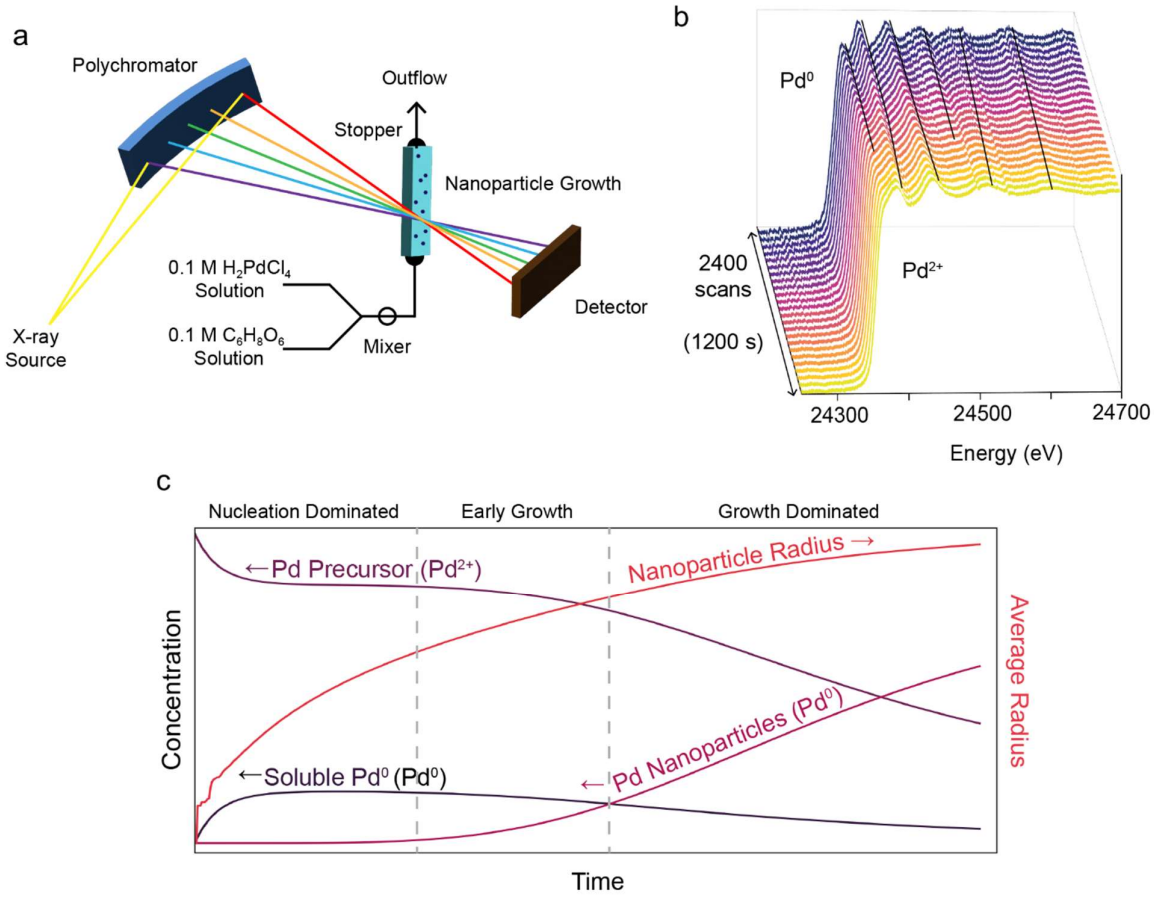

Figure 5-1. a) The experimental setup at the I-20 EDE beamline, showing the X-ray path through a capillary tube containing the reaction solutions. **b)** A sample of the 2400 XAFS spectra collected over 1200 seconds of Pd reduction where changes in the XANES and EXAFS regions are indicated by black lines following peaks. **c)** A model fitting the time-resolved concentrations of Pd^{2+} (purple), metallic Pd^0 (pink) and soluble Pd^0–Cl (black), and the nanoparticle radius (red).

By comparing XANES and EXAFS data, the concentration of a ligand coordinated Pd^0 species in solution could theoretically be calculated. Considering previous literature, it is likely that Pd^0 is Cl-coordinated, due to the presence of ions from CTAC.[31,32] The contribution of fully coordinated Pd-Cl bonds ($Pd\text{-}Cl^{initial}$) in unreduced Pd^{2+} precursor ($Pd^{2+,\,time}/Pd^{2+,\,initial}$) can be subtracted from the measured Pd-Cl coordination number ($Pd\text{-}Cl^{time}$), to give Pd^0-Cl coordination. The rationale for this approach is discussed in detail in Supplementary Note S1 but can be summarised in a single equation.

$$(Pd^0\text{-}Cl)^{time} = (Pd\text{-}Cl)^{time} - \left((Pd\text{-}Cl)^{initial} \times (Pd^{2+})^{time} / (Pd^{2+})^{initial} \right) \qquad \text{Eq. 5-5}$$

This measurement includes Pd^0-Cl species which are severely under-coordinated at the metal surface and assumes a constant total Pd concentration. Since EXAFS cannot reliably distinguish the ligand species, Pd^0 coordinated with O or Cl are both counted under Pd^0-Cl coordination. Observing such a reduced species and its kinetic profile reveals the reaction stages where growth processes dominate over agglomeration and Pd^0-Cl supersaturation drives the formation of new nuclei. Developing a simplified nanoparticle nucleation and growth model enables estimation of the theoretical concentration profile of zero-valent Pd^0–Cl (Figure 5-1c, Note S5-2). The dimensionless population-balanced modelling of reaction species enables an understanding of the kinetic effects of increased temperature and seeded growth, in combination with the formation of a transient Pd^0–Cl species.

The experimental calculation of Pd^0–Cl concentration from *in situ* XAFS is performed for the first time during the AA reduction of CTAC capped K_2PdCl_4. XANES linear combination fitting and EXAFS fitting, are run for 2400 spectra with 500 ms time resolution, Pd^0-Cl concentrations at temperatures of 30°C to 60°C show a peak at 6.72 mM before rapid growth, occurring immediately with pre-nucleated seeds since the nucleation stage is bypassed. Increased temperature and seeded growth lead to lower maximum concentration of 5.73 mM Pd^0-Cl and dictate the morphology of nanoparticles formed. A simple precipitated growth model fits with the experimental calculation of Pd^0-Cl concentration, to understand the balance of Pd species. Time-resolved SAXS and TEM results follow the transition from spherical nuclei to CTAC-controlled dendritic Pd nanoparticles. Thus, the combination of *in situ* characterization tools successfully records both growth kinetics and M^0-Cl species and could be applied to study a wide range of nanoparticle growth systems, as a step towards rational design of nanoparticle morphology.

5.3 Results and discussion

5.3.1 Nanoparticle Growth Observation

TEM images captured at different growth time of a 50°C reduction show the key morphological changes in the nanoparticles (Figure 5-2a-j). First, the formation of spherical particles with an average diameter of 5.75 ± 1.30 nm, is observed at 60 s reaction time (Figure 5-2a, Table S5-1). After 120 s, increased anisotropy and aggregation occur, leading to the first structured nanoparticles (Figure 5-2b). The nanoparticles continue to grow from 360 until 480 s, where fully sized particles are formed (Figure 5-2c, d). The shape, size and crystal structures of nanoparticles continue to adjust as the reaction time continues to 1200 s, likely driven by halide etching and reoxidation (Figure 5-2e).

Porous spherical Pd nanoparticles with an average radius of 76.97 ± 19.63 nm were achieved at the baseline condition of unseeded 60°C growth measured for 1200 seconds (Figure S5-1, S5-2), like those obtained at 50°C. The structure of individual nanoparticles is flowerlike, with a solid core from which nano-dendritic arms extend. XRD results show that nanoparticles formed are highly crystalline, with a preferential (111) lattice (Figure S5-3). This is confirmed by Pd(111) and Pd(100) crystal lattices observed in transmission electron microscopy (TEM) imaging (Figure S5-4). The nanoparticle morphology formed has a high surface area, where dendritic structure and size are controlled by CTAC.

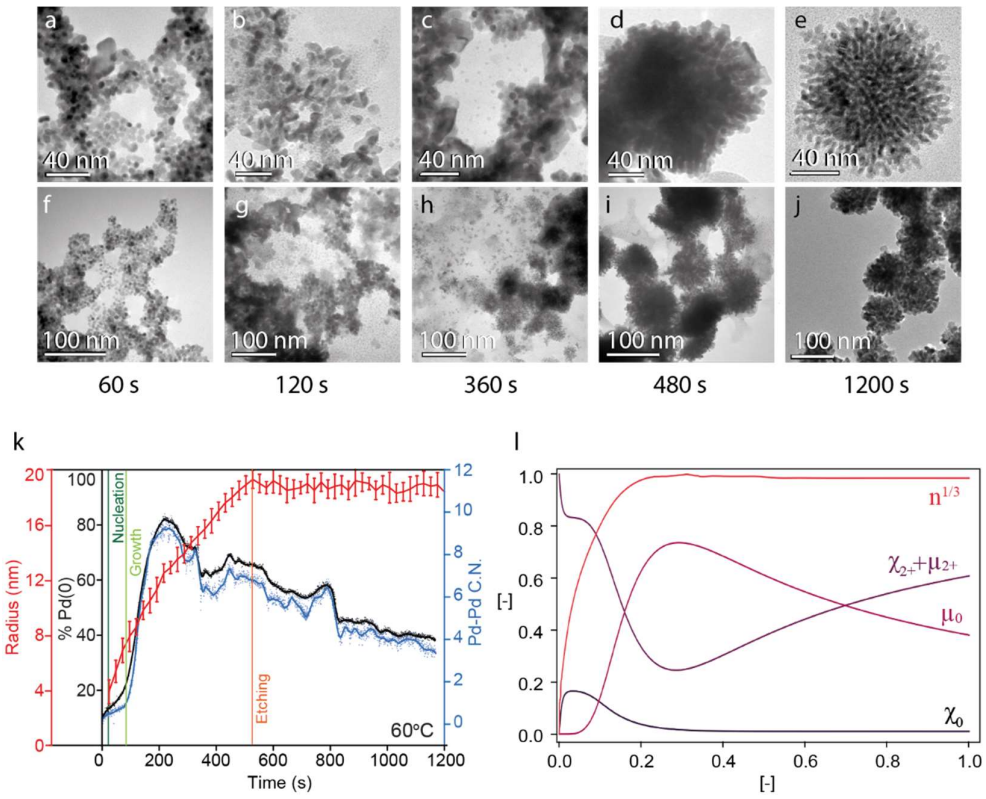

Figure 5-2. a-j), Representative images of nanoparticles formed at 50°C reaction times of 60 s, 120 s, 360 s, 480 s and 1200 s, from left to right with scale bars of 40 nm (a-e) and 100 nm (f-j). **k),** Experimental reaction profile of Pd reduction at 60°C measured by XAFS and SAXS, showing the change in concentration of Pd^0 (black), Pd-Pd coordination (blue) and nanoparticle radius (red). The expected reaction stages are indicated after rapid reduction as nucleation, growth and etching, where Pd^{2+} is oxidatively dissolved into the solution. l)**,** Corresponding dimensionless concentration results modelled for soluble Pd^0 (χ_0, black), Pd^{2+} ($\chi_{2+}+\mu_{2+}$, purple), and total Pd^0 (μ_0, pink), alongside the nanoparticle radius ($n^{1/3}$, red).

The molar ratio of reactants was modified from a previously described ascorbic acid reduction of CTAC-capped K_2PdCl_4 to enable *in situ* XAFS characterization.[29] The combined visualization of *in situ* XANES, EXAFS and SAXS results during a 60°C reduction provides a typical experimental growth profile to reveal reaction stages of reduction, nucleation, growth and reoxidation (Figure 5-2k). SAXS monitoring of nanoparticle radius shows a steady increase before plateauing, likely caused by surfactant induced size limitation. In contrast, linear combination fitting of the XANES region (Note S5-3, Figure S5-5, Table S5-2) initially shows a sigmoidal shape during the chemical reduction of Pd^{2+} to Pd^0 (%Pd(0), Figure 5-2k). The deviation from

sigmoid within the first seconds of reaction is attributed to rapid chemical reduction prior to nucleation (Figure S5-6). EXAFS fitting of Pd coordination number (Pd-Pd C.N., Table S5-3) shows a similar trend to oxidation state change, although the initial rates differ during reduction and nucleation stages. The negative reaction rate observed after the sigmoidal growth profile is caused by the reoxidation of the precipitated nanoparticles.

Precipitated growth model results (Figure 5-2l, Figure S5-7 and S5-8) corroborate experimentally observed changes in the same parameters of Pd^{2+} ($\chi_{2+}+\mu_{2+}$) and Pd^0-Cl concentration (χ_0), Pd-Pd C.N. (μ_0) and nanoparticle radius ($n^{1/3}$). The initial reduction stage is included as a sudden decrease in $\chi_{2+}+\mu_{2+}$ and χ_0 concentration decreases during rapid growth. Nucleation is continuous but the reaction is growth dominated once a critical radius is achieved. Reoxidation competes with growth and dominates at the later reaction stages, where Pd^{2+} concentration is low. The rate and duration of nucleation depend on reaction conditions such as concentration, temperature and pre-existing solid species within the solution.

5.3.2 Pd^0-Cl in Temperature-Controlled Growth

Every reaction stage is accelerated by increased temperature (Figure 5-3 a-d, Figure S5-9, Note S5-2), according to the experimental observation of a temperature series. Extended nucleation and slow growth are observed at 30ºC and 40ºC. Increasing reaction temperature shortens nucleation stages to 800 s and <100 s at 50ºC and 60ºC, respectively. The results are more reproducible at lower temperatures (Figure S5-10), attributed to the rapid growth at increased temperatures causing higher degree of irregularity in the system.

Modelled soluble Pd^0 values show a strong resemblance with experimental results. The fit of the growth stages quantifies the dependence of each reaction stage on temperature (Figure 4-3 e-h) and the corresponding formation of soluble Pd^0 species. The model also captures the effects of competing processes, to understand the consecutive domination of reduction, nucleation, growth and reoxidation stages.

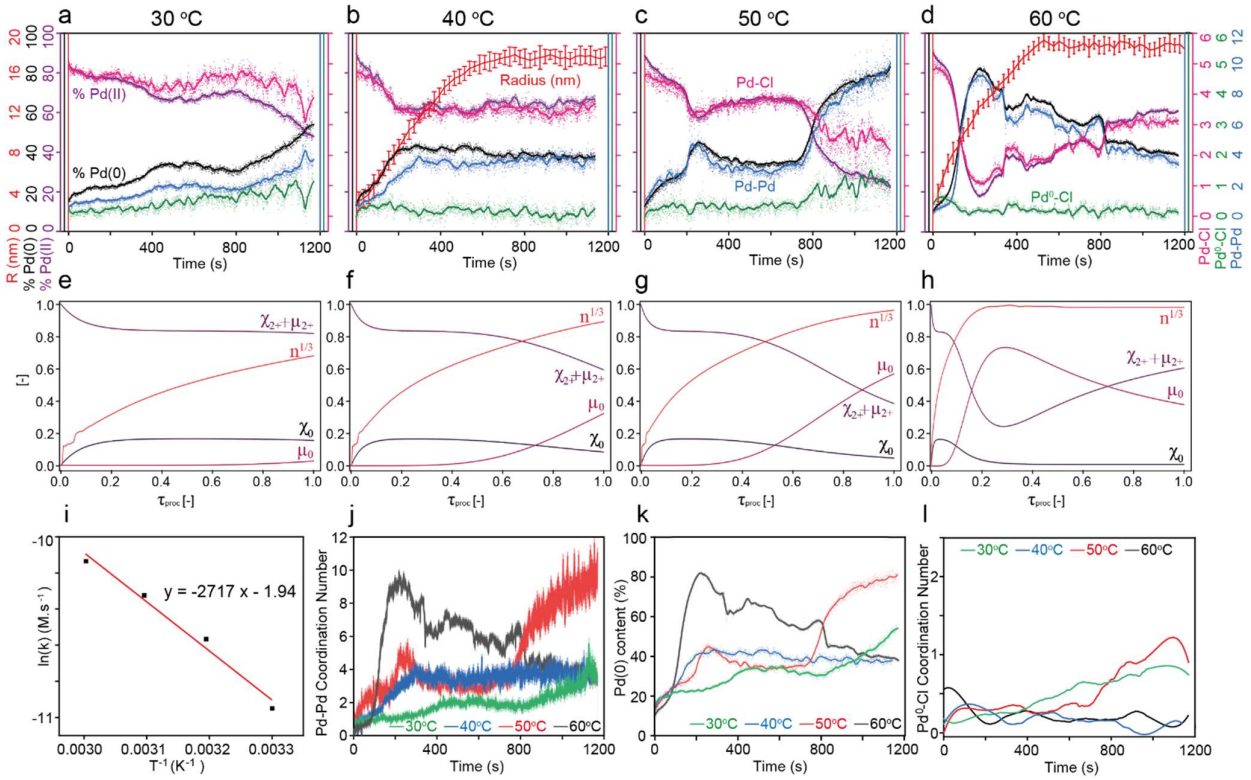

Figure 5-3. a-d), Combined reaction profiles with values of nanoparticle radius (red), Pd^0% concentration (black) and Pd^{2+}% concentration (purple), coordination numbers of Pd-Cl (pink) and Pd-Pd (blue), and the calculated Pd^0-Cl coordination (green) at temperatures of (a) 30°C, (b) 40°C, (c) 50°C and (d) 60°C. **e-h),** Corresponding dimensionless concentration modelled for Pd^0–Cl (χ_0, black), Pd^{2+} ($\chi_{2+}+\mu_{2+}$, purple), solid Pd^0 (μ_0, pink), and nanoparticle radius ($n^{1/3}$, red). **i),** Arrhenius plot from which a slope of -2717 is measured. **j),** Collected results of Pd-Pd coordination at each temperature and **k),** Corresponding Pd(0)% content. **l),** The calculated Pd^0-Cl coordination numbers at temperatures of 30°C (green), 40°C (blue), 50°C (red) and 60°C (grey).

Nucleation rates of -16.22 ± 0.38, -20.66 ± 0.45, -26.65 ± 0.39 and -38.50 ± 0.89 $\mu mol.L^{-1}.s^{-1}$ are measured at 30ºC, 40ºC, 50ºC and 60ºC, respectively (Figure S5-11). The steady increase in rate with temperature gives an Arrhenius plot with an activation energy of 22.59 kJ/mol (gas constant = 8.314 $J.mol^{-1}.K^{-1}$, Figure 4-3i, Note S4-4, Table S4-4). This value is influenced by the interaction of CTAC with Pd at the metal surface and is lower than, but within a reasonable range of previous literature values. The activation energy was calculated to be 37 kJ mol^{-1} for $Pd(OAc)_2$

with trioctylphosphine ligand with hexanol,[32] and 43.4 kJ/mol in the case of ascorbic acid reduction of Pd nanoparticle in the presence of CTAB[28].

Further evidence of the role of CTAC in determining the shape and size of nanoparticles is the uniformity of average radius measured from SAXS (Figure 5-3a-d, Figure S5-12, S5-13, Table S5-5) and electron microscope data under different temperature conditions. Average particle diameters of 105.35 ± 25.96 nm, 82.50 ± 21.01 nm, and 76.97 ± 19.63 nm are measured from TEM images (Figure S5-14, Table S5-1). Diameters from SAXS refinement at the plateaued region show increasing anisotropy with contribution from reoxidative etching, in which nanoparticle shape changes. The trend of the SAXS curve appears to fit closely with the WF two-step mechanism nanoparticle size simulation by Mozaffari et al.[26] Yet the concentration of Pd converted to Pd^0 is only 55.6% (17.57 mM) at 30ºC and 38.5% (12.08 mM) at 40ºC at 1200 s. This can be understood as a lower volume of nanoparticles forming at low temperature reactions.

The collected Pd^0 concentration and average Pd coordination at each temperature show a similar trend (Figure 5-3j, k and Figure S5-15). The 50ºC growth profile also fits well with the MP-AES measurements of solid particle concentration (Figure S5-16). The calculated average Pd^0–Cl coordination for each temperature is given as a concentration (Figure 5-3l, Figure S5-17, Table S5-6). This species' supersaturation seems to occur before the rapid growth stage of the reaction which is consistent with the idea of their consumption during growth. The maximum concentration calculated for Pd^0-Cl species is 6.45 mM at 30ºC, 3.77 mM at 40ºC, 10.31 mM at 50ºC and 6.72 mM at 60ºC. It appears that the concentration of Pd^0-Cl is highest in cases where nucleation is rapid, so we study a case where the introduction of pre-existing seed surfaces replaces the nucleation stage.

5.3.3 Bypassing Nucleation with Seeded Growth

Adding seeds to nanoparticle solutions increases monodispersity and provides a shape template for nanoparticle growth.[33] Pd seed morphology was characterized prior to growth, to understand its effect on the resulting particles. The size of seeds was found

to be uniform as limited by CTAC, and stable after completion. Due to the predicted small size of seeds, a combination of EXAFS (Table S5-7) and SAXS fitting (Figure S5-18, Table S5-1) was used to measure spheres with an average diameter of 3.78 nm. This fits previous reports of 3.4 nm,[34] 5 nm[35] and 3-4 nm[36] seeds and is comparable with the initial nucleated particles observed during unseeded growth (5.75 nm).

SAXS observations show that the shape of the nanoparticles does not change significantly with the introduction of pre-formed seeds, but the average size and dispersity decrease (Figure S5-18). The introduction of seeds shows the reaction profile during controlled heterogeneous nucleation at 50ºC within our system, which bypasses the nucleation stage and immediately follows growth. EXAFS shows the reaction rates at 50ºC for cases where 0 μL, 1 μL, 10 μL and 100 μL of seed solution were added to the reaction mixture (Figure 5-4a-d, Figure S5-19). The reproducibility of seeded growth results was most consistent in high concentration samples, possibly due to reduced accuracy in small-volume measurements (Figure S5-20).

The average diameter of nanoparticles obtained from SAXS fitting with seeded growth is 67.05 nm, compared with non-seeded growth, 54.1 nm (Figure S5-18). The increase in size and monodispersity can be ascribed to the larger number of nucleation sites in the presence of seeds allowing even distribution of growth species. In cases where seeds are absent, continuous nucleation is necessary for continued growth once nanoparticles have reached CTAC-limited size.[21]

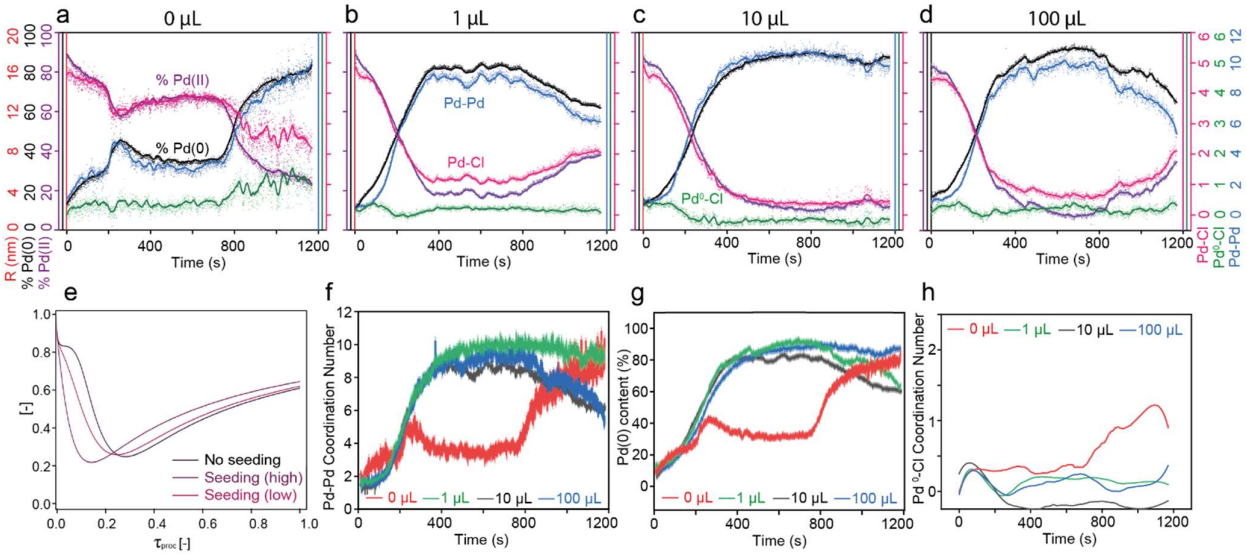

Figure 5-4. a-d), Combined characterization results of nanoparticle radius (red), Pd^{0}% concentration (black) and Pd^{2+}% concentration (purple), coordination numbers of Pd-Cl (pink) and Pd-Pd (blue), and the calculated Pd^{0}-Cl coordination (green) at seed concentrations of (a) 0 µL, (b) 1 µL, (c) 10 µL and (d) 100 µL, as a seeded growth series. **e),** Corresponding modelled fit of growth without seeds, compared to low and high seed concentrations. **f),** Collected Pd K-edge EXAFS fitted Pd-Pd C.N. results for the seeded growth series. **g),** The linear combination Pd K-edge XANES fitting results of Pd0 content, under the same growth series. **h),** Pd^{0}-Cl calculated values for seed concentrations of 0 µL, 1 µL, 10 µL and 100 µL, smoothed for clarity of visualization.

Based on our calculated model (Figure 5-4e), the growth rate depends on the radius of the nuclei, the diffusion coefficient of the growth species, the molar volume of nuclei, and the bulk and surface concentrations. Although the Pd growth rate is expected to be higher when more seeds are introduced, this is contrary to recorded data, indicating that the seed volumes experimentally added always exceeded a 'high concentration' value. In cases where nuclei size is constant and the growth is diffusion controlled, the growth rate should not change significantly, as experimentally observed.

A comparison of all seeded growth conditions for Pd-Pd coordination and Pd^{0} conversion shows that the rates of rapid growth are consistent throughout the series (Figure 5-4f, g, Figure S5-21). This suggests that the growth rate may be diffusion-limited instead of determined by available growth surfaces, and that reduction in solution is occurring simultaneously with the surface reduction. The calculated values

of Pd^0-Cl show a similar trend in all seeded growth conditions, peaking before rapid growth (Figure 5-4h, Figure S5-22). The supersaturation of this Pd^0-Cl species has maximum values of 4.83 mM with 1 μL seeds, 5.73 mM at 10 μL seeds and 4.05 mM at 100 μL seeds. The formation of Pd^0-Cl species within the solution rapidly decreases as the growth species are used for nanoparticle formation directly on the seed templates.

5.3.4 Discussion

The difference in rates of chemical reduction and bond formation indicates the formation of a Pd^0-Cl intermediate during Pd nanoparticle growth. This ligand-capped growth species aligns with the literature which predicts the formation of Pd^0-Cl species in solution.[22] Supersaturation of this species is highest during the nucleation phase, which is consistent with the idea that Pd^0-Cl species are a driving force for continuous nucleation, aggregating to form nuclei. During growth, reduction in solution may occur simultaneously with direct reduction at the bonding surface and it appears that a combination of monomer addition from solution, surface reduction and agglomeration of existing particles contribute to the rapid growth of nanoparticles. The concentration of Pd^0-Cl during nucleation peaks increased at higher temperatures as the reaction was accelerated.

Based on the precipitated growth model fitting, it can be noted that, despite the different chemical and physical processes involved, the rate of reduction, nucleation, rapid growth, and reoxidation, all scale with an increase in temperature. This is contrary to seeded growth, where the rapid growth rate was constant across all concentrations of seed solutions. The effect of seed solutions in obviating the nucleation stage is clearly shown. However, Pd^0-Cl peaks with comparable concentrations suggest that solution reduction may dominate in the early stages. This would result in a rapid growth rate independent of available reduction surfaces, which are increased with higher seed concentration.

In this case of porous Pd nanoparticles, it appears that the growth of initial spherical particles is largely contributed by solution reduced species, while the agglomeration

and surface growth lead to dendritic growth. These findings show that Pd^0-Cl species may influence the morphology of particles formed and elucidate the mechanisms of CTAC-capped Pd growth.

5.4 Conclusion

Through a combination of characterization tools, a ligand coordinated reduced Pd species (Pd^0-Cl) concentration profile is monitored during Pd nanoparticle growth for the first time. This finding confirms the presence of solution reduction, particularly in the nucleation phase. Seeded growth results show that the nucleation stage is removed and that the rapid growth rate is independent of seed concentration. Observations from a temperature series conclude that higher temperatures leads to increased supersaturation of Pd^0-Cl and smaller average nanoparticle size. An activation energy of 22.59 kJ/mol is calculated for the growth of Pd nanoparticles, and we believe that such calculations, directly gathered from the chemical reduction observed are most accurate to be used for further modelling and predictions of growth.

The presented work serves three purposes in the literature of nanoparticle growth. First, experimental evidence corroborates the formation of a soluble Pd^0-Cl intermediate, suggesting reduction in solution rather than directly at a growth surface, which may be applied to a range of transition metal growth systems. Second, such a high time-resolution fitting of XANES and EXAFS data during nanoparticle growth has yet to be published and is versatile in applicability to different materials. The improvement of time-resolution in growth characterization allows more detailed and complete observation of growth kinetics to verify and inform theoretical understanding. Lastly, the model fitting and chemical understanding of the rate and activation energy in this reaction will contribute to the future rational design of Pd nanoparticles, once a large enough dataset is gathered. Rational design to predict the formation of nanoparticles in solution could be invaluable for the future application and developments of Pd catalysts.

5.6 References

1 Xiao, W. *et al.* Optimizing the ORR activity of Pd based nanocatalysts by tuning their strain and particle size. *Journal of Materials Chemistry A* **5**, 9867-9872 (2017). https://doi.org:10.1039/c7ta02479g

2 Wang, M. *et al.* Electrocatalytic Activities of Oxygen Reduction Reaction on Pd/C and Pd–B/C Catalysts. *The Journal of Physical Chemistry C* **121**, 3416-3423 (2017). https://doi.org:10.1021/acs.jpcc.6b12026

3 Wang, T. *et al.* Palladium alloys used as electrocatalysts for the oxygen reduction reaction. *Energy & Environmental Science* **14**, 2639-2669 (2021). https://doi.org:10.1039/d0ee03915b

4 Joudeh, N., Saragliadis, A., Koster, G., Mikheenko, P. & Linke, D. Synthesis methods and applications of palladium nanoparticles: A review. *Frontiers in Nanotechnology* **4** (2022). https://doi.org:10.3389/fnano.2022.1062608

5 Pérez-Lorenzo, M. Palladium Nanoparticles as Efficient Catalysts for Suzuki Cross-Coupling Reactions. *The Journal of Physical Chemistry Letters* **3**, 167-174 (2012). https://doi.org:10.1021/jz2013984

6 Biffis, A., Centomo, P., Del Zotto, A. & Zecca, M. Pd Metal Catalysts for Cross-Couplings and Related Reactions in the 21st Century: A Critical Review. *Chem Rev* **118**, 2249-2295 (2018). https://doi.org:10.1021/acs.chemrev.7b00443

7 Tran, M., DePenning, R., Turner, M. & Padalkar, S. Effect of citrate ratio and temperature on gold nanoparticle size and morphology. *Materials Research Express* **3** (2016). https://doi.org:10.1088/2053-1591/3/10/105027

8 Polavarapu, L., Mourdikoudis, S., Pastoriza-Santos, I. & Pérez-Juste, J. Nanocrystal engineering of noble metals and metal chalcogenides: controlling the morphology, composition and crystallinity. *CrystEngComm* **17**, 3727-3762 (2015). https://doi.org:10.1039/c5ce00112a

9 Alam, M. S., Siddiq, A. M., Narayanan, S. S., Samanta, D. & Das, S. K. Cationic Surfactant (CTAC) Assisted Synthesis of Silver Nanoparticles with Controlled Size: Optical, Morphological and Bactericidal Studies. *Journal of Nanoengineering and Nanomanufacturing* **5**, 124-131 (2015). https://doi.org:10.1166/jnan.2015.1238

10 Zhang, L., Lee, K. & Zhang, J. The effect of heat treatment on nanoparticle size and ORR activity for carbon-supported Pd–Co alloy electrocatalysts. *Electrochimica Acta* **52**, 3088-3094 (2007). https://doi.org:10.1016/j.electacta.2006.09.051

11 Abbas, G., Kumar, N., Kumar, D. & Pandey, G. Effect of Reaction Temperature on Shape Evolution of Palladium Nanoparticles and Their Cytotoxicity against A-549 Lung Cancer Cells. *ACS Omega* **4**, 21839-21847 (2019). https://doi.org:10.1021/acsomega.9b02776

12 Lee, S., Cho, H., Kim, H. J., Hong, J. W. & Lee, Y. W. Shape- and Size-Controlled Palladium Nanocrystals and Their Electrocatalytic Properties in the Oxidation of Ethanol. *Materials (Basel)* **14** (2021). https://doi.org:10.3390/ma14112970

13 An, K. & Somorjai, G. A. Size and Shape Control of Metal Nanoparticles for Reaction Selectivity in Catalysis. *ChemCatChem* **4**, 1512-1524 (2012). https://doi.org:10.1002/cctc.201200229

14 Wen, X. *et al.* Synthesis of Palladium Nanodendrites Using a Mixture of Cationic and Anionic Surfactants. *Langmuir* **36**, 1745-1753 (2020). https://doi.org:10.1021/acs.langmuir.9b03804

15 N, A., Ang, B. C., M.A, A. & Bong, C. W. Influence of Precursor Concentration and Temperature on the Formation of Nanosilver in Chemical Reduction Method. *Sains Malaysiana* **47**, 157-168 (2018). https://doi.org:10.17576/jsm-2018-4701-19

16 Song, Y., Zhang, M., Fang, H. & Xia, H. Shape transformation of gold nanoparticles in aqueous CTAB/CTAC solution to generate high-index facets for electrocatalysis and SERS activity. *ChemPhysMater* (2022). https://doi.org:10.1016/j.chphma.2022.04.006

17 Niu, W., Zhang, L. & Xu, G. Seed-mediated growth method for high-quality noble metal nanocrystals. *Science China Chemistry* **55**, 2311-2317 (2012). https://doi.org:10.1007/s11426-012-4681-z

18 Hornberger, E. *et al.* Seed-Mediated Synthesis and Catalytic ORR Reactivity of Facet-Stable, Monodisperse Platinum Nano-Octahedra. *ACS Applied Energy Materials* **4**, 9542-9552 (2021). https://doi.org:10.1021/acsaem.1c01696

19 Michaelis, M. & Henglein, A. Reduction of palladium (II) in aqueous solution: stabilization and reactions of an intermediate cluster and palladium colloid formation. *The Journal of Physical Chemistry* **96**, 4719-4724 (1992). https://doi.org:10.1021/j100190a105

20 Watzky, M. A. & Finke, R. G. Transition Metal Nanocluster Formation Kinetic and Mechanistic Studies. A New Mechanism When Hydrogen Is the Reductant: Slow, Continuous Nucleation and Fast Autocatalytic Surface Growth. *Journal of the American Chemical Society* **119**, 10382-10400 (1997). https://doi.org:10.1021/ja9705102

21 Mozaffari, S. *et al.* Ligand-Mediated Nucleation and Growth of Palladium Metal Nanoparticles. *J Vis Exp* (2018). https://doi.org:10.3791/57667

22 Karim, A. M. *et al.* Synthesis of 1 nm Pd Nanoparticles in a Microfluidic Reactor: Insights from in Situ X-ray Absorption Fine Structure Spectroscopy and Small-Angle X-ray Scattering. *The Journal of Physical Chemistry C* **119**, 13257-13267 (2015). https://doi.org:10.1021/acs.jpcc.5b01681

23 Yao, S. *et al.* Insights into the Formation Mechanism of Rhodium Nanocubes. *The Journal of Physical Chemistry C* **116**, 15076-15086 (2012). https://doi.org:10.1021/jp302471p

24 Wojnicki, M., Fitzner, K. & Luty-Blocho, M. Kinetic studies of nucleation and growth of palladium nanoparticles. *J Colloid Interface Sci* **465**, 190-199 (2016). https://doi.org:10.1016/j.jcis.2015.11.066

25 Saeki, M. *et al.* In Situ Time-Resolved XAFS Studies on Laser-Induced Particle Formation of Palladium Metal in an Aqueous/EtOH Solution. *The Journal of Physical Chemistry C* **123**, 817-824 (2018). https://doi.org:10.1021/acs.jpcc.8b09532

26 Mozaffari, S. *et al.* Colloidal nanoparticle size control: experimental and kinetic modeling investigation of the ligand-metal binding role in controlling the nucleation and growth kinetics. *Nanoscale* **9**, 13772-13785 (2017). https://doi.org:10.1039/c7nr04101b

27 Finney, E. E. & Finke, R. G. Nanocluster nucleation and growth kinetic and mechanistic studies: a review emphasizing transition-metal nanoclusters. *J Colloid Interface Sci* **317**, 351-374 (2008). https://doi.org:10.1016/j.jcis.2007.05.092

28 Yang, T. H. *et al.* Toward a Quantitative Understanding of the Reduction Pathways of a Salt Precursor in the Synthesis of Metal Nanocrystals. *Nano Lett* **17**, 334-340 (2017). https://doi.org:10.1021/acs.nanolett.6b04151

29 Wang, F. *et al.* Porous single-crystalline palladium nanoparticles with high catalytic activities. *Angew Chem Int Ed Engl* **51**, 4872-4876 (2012). https://doi.org:10.1002/anie.201107376

30 Zheng, Y., Zeng, J., Ruditskiy, A., Liu, M. & Xia, Y. Oxidative Etching and Its Role in Manipulating the Nucleation and Growth of Noble-Metal Nanocrystals. *Chemistry of Materials* **26**, 22-33 (2013). https://doi.org:10.1021/cm402023g

31 Xie, M. *et al.* A Quantitative Analysis of the Reduction Kinetics Involved in the Synthesis of Au@Pd Concave Nanocubes. *Chemistry* **25**, 16397-16404 (2019). https://doi.org:10.1002/chem.201904074

32 Mozaffari, S. *et al.* The role of nanoparticle size and ligand coverage in size focusing of colloidal metal nanoparticles. *Nanoscale Adv* **1**, 4052-4066 (2019). https://doi.org:10.1039/c9na00348g

33 Kim, S.-W. *et al.* Synthesis of Monodisperse Palladium Nanoparticles. *Nano Letters* **3**, 1289-1291 (2003). https://doi.org:10.1021/nl0343405

34 Liu, J., He, F., Gunn, T. M., Zhao, D. & Roberts, C. B. Precise Seed-Mediated Growth and Size-Controlled Synthesis of Palladium Nanoparticles Using a Green Chemistry Approach. *Langmuir* **25**, 7116-7128 (2009). https://doi.org:10.1021/la900228d

35 Zhang, L., Wang, L., Jiang, Z. & Xie, Z. Synthesis of size-controlled monodisperse Pd nanoparticles via a non-aqueous seed-mediated growth. *Nanoscale Research Letters* **7**, 312 (2012). https://doi.org:10.1186/1556-276X-7-312

36 Niu, W. *et al.* Seed-Mediated Growth of Nearly Monodisperse Palladium Nanocubes with Controllable Sizes. *Crystal Growth & Design* **8**, 4440-4444 (2008). https://doi.org:10.1021/cg8002433

37 Collette, A. Python and HDF5. *O'Reilly* (2013).

38 Newville, M. Larch: An Analysis Package for XAFS and Related Spectroscopies. *Journal of Physics: Conference Series* **430**, 012007 (2013). https://doi.org:10.1088/1742-6596/430/1/012007

39 Newville, M., Stensitzki, T., Allen, D. B. & Ingargiola, A. *LMFIT: Non-Linear Least-Square Minimization and Curve-Fitting for Python*. (2014).

40 Ankudinov, A. L., Ravel, B., Rehr, J. J. & Conradson, S. D. Real-space multiple-scattering calculation and interpretation of x-ray-absorption near-edge structure. *Physical Review B* **58**, 7565-7576 (1998). https://doi.org:10.1103/PhysRevB.58.7565

Chapter 6

Conclusion and Future Perspectives

6.1 Conclusion

Based on the X-ray absorption spectroscopy, various experimental methods have been showcased to achieve distinct temporal resolutions: one being Energy Dispersive X-ray Fine Structure Spectroscopy (EDE) which offers resolution in the range of seconds to milliseconds, while another technique involves X-ray Free Electron Laser pump probe experiments providing resolutions in the picoseconds to femtoseconds range. These methodologies not only cater to the necessary time scales for measurements but also foster investigations into different aspects of physical chemistry processes such as thermodynamics, kinetics, and photo-induced electron excitation and migration, opening up avenues for further exploration and understanding in these areas. The PhD projects used time-resolved XAS to investigate three common phenomena in catalysis and catalysts synthesis: 1) rate determined half reactions kinetics study, 2) intermediates during nanoparticles nucleation and growth, and 3) dynamics of charge transfer in metal support interaction.

The kinetics investigation focusing on the determination of the rate for partial reactions in catalysis based on the Mar-van Krevelen mechanism has been infrequently acknowledged in the extensive body of kinetics research. Through the utilization of Energy Dispersive EXAFS, it becomes feasible to observe and track the kinetics associated with the release and storage of lattice oxygen. When juxtaposed with the complete CO oxidation reaction catalysed by CZ catalysts, it has been conclusively established that the step determining the rate is indeed the process of lattice oxygen release. Furthermore, in comparison to pristine CZ samples, it has been observed that CZ catalysts loaded with metals exhibit a noteworthy enhancement in both their catalytic properties and dynamic performance. The incorporation of metals into CZ catalysts has proven to be instrumental in augmenting their efficiency and effectiveness in catalytic reactions, thereby underscoring the significance of this approach in advancing the field of catalysis research. The enhanced catalytic performance and dynamic behaviour of metal-loaded CZ catalysts underscore the potential for further advancements in catalysis research through the strategic manipulation of catalyst composition and structure.

With the implementation of ultra-fast X-ray Absorption Spectroscopy (XAS) in X-ray Free Electron Lasers (XFEL), researchers are able to investigate the intricate dynamics of charge transfer occurring in metal support interactions. The time frame for the completion of the charge transfer process typically falls within the range of 200-300 femtoseconds, following the initial intraband excitation phase that lasts approximately 1-2 picoseconds. This rapid process leads to a slight migration of excited electrons towards the Copper (Cu) atoms located on the surface, causing a modification in the

electronic configuration and ultimately boosting the catalytic performance of the associated reactants.

These researches contribute significant fundamental insights regarding the critical importance of conducting a dynamics study on elementary reactions, thereby stimulating further and more thorough contemplation and discourse on the practical application and advantages of utilizing time-resolved X-ray spectroscopy in research endeavors.

Nanoparticles' crystallization and growth play a crucial role in the synthesis of metal catalysts. By utilizing time-resolved X-ray Absorption Spectroscopy (XAS), it is possible to observe and analyse the entire progression starting from the reduction of precursors, through nucleation, and finally to the growth phase. Within this process, an intermediate stage involving Pd^0-Cl was successfully identified and documented. Interestingly, the addition of Pd seeds into the system brought about significant changes in the growth dynamics, resulting in a peak concentration of Pd^0-Cl reaching 5.73 millimolar, all without a distinct nucleation phase being observed. This alteration in growth behavior also exhibited varying rates of formation based on temperature conditions, with a calculated activation energy of 22.59 kilojoules per mole for the nucleation of Pd within a model that emphasizes a balanced distribution of the population involved in the precipitated growth process.

6.2 Future perspectives

6.2.1 Challenges

During my four years work at synchrotron facilities, I am realising more and more that every single means of characterization has its limitations. For example: Energy Dispersive EXAFS has its advent in quick data acquisition, but since the beam is with a range of energy, the size for the beam is not even exposure to the sample, which needs the sample to be highly homogeneous. This is okay for liquid system, but will be a big challenges for solids. Even we used a rotating reactor to try to have a relatively homogeneous condition of samples, but the quality of the spectra was still not ideal especially for the EXAFS part. This is one of the challenges we are facing with. With Q-XAS by the movement of the monochromator quickly, higher quality of spectra can be achieved. But the time resolution may not be that high. So, there is no perfect techniques can solve problems once for all. Different characterization techniques should cross check the results and correlate with each other for a conclusion.

However, another challenge is that the reaction conditions for each characterization techniques are difficult to maintain exactly the same with each other. This is because of the measurement condition usually has some requirements for samples especially for in-situ or even *operando* conditions. In our research, to meet the highly consistent conditionality requirements, we did component analysis of gases we used and temperature calibration for all conditions and all reactors. However, lots of surprises can still happen when measuring. Well design of the experimental set-up should be carefully considered as well as the communication with technicians and beam line scientists.

For XFEL study, that in itself is a huge challenge for us. Generally speaking, the liquid system is much more easier for XFEL pump probe measurements. The solid materials are very difficult to loaded on the holders like SI wafer homogeneously, even we thought it was homogeneous, but it's actually not. Which reduced signal-to-noise ratio of the spectrum as well as the dynamics analysis. Secondly, laser induced pump probe experiments is more a physical process than chemistry. To connect this two is a challenge for us. Since the measurement condition require UHV, having a in-situ measurement condition is nearly impossible so far. The pre-measurement operations should be done carefully if certain conditions should be meet. Thirdly, the optical laser power density affects the dynamics directly. The power density dependence research must be done before move to temporal profile measurement. However, this is a time consuming operation, which makes the limited beam time become more pressing.

6.2.2 Future works on time-resolved X-ray spectroscopy for heterogenous catalysis

Start with the challenges mentioned before, more work should be done to refine the previous projects and expend to new projects in the future.

1. The study of kinetics concerning the process of O releasing can also be interpreted as the phenomenon of O vacancy creation. Through techniques like EDE or Q-XAS, a novel approach can be suggested to quantify the presence of O vacancies and assess the rate at which they are generated. A detailed case study has already been conducted on catalysts based on cerium; it is imperative to apply the same methodology to analyze additional catalysts in order to validate the proposed method. Furthermore, it is essential to enhance the resolution of EXAFS for the purpose of tracking the alterations in local structure that occur during the generation of O vacancies. While some studies have delved into the changes in local structure, the kinetics or dynamics of these alterations remain largely unexplored. Utilizing cerium-based catalysts as a focal point for research serves as a promising starting point, supplementing the existing body of knowledge.

2. XFEL is still a advanced area for heterogenous catalysis. With the challenges of harsh test conditions and high demands on samples, in-situ XFEL pump probe is still a world problem for researchers and engineers. Before that, pre-test operation can be conduced to get a similar in-situ conditions. Based on our XFEL study on dynamics of charge transfer between Cu and Ce, the catalytic properties will be checked with water gas shift reactions. Different materials will be measured with pump probe experiments to connect the performance with charge transfer dynamics. This will be the first time to bring the ultra-fast physical process to heterogeneous catalysis.
3. Optical laser-induced pump probe experiments is perfect to study the light sensitive materials especially for photocatalysis and semiconductor materials. The n-type TiO_2 semiconductor is a widely used photocatalyst for water splitting, CO_2 and N_2 reduction, but suffers from the low absorption in the visible range. To enable visible-light-driven photocatalysis, we have designed an Au@TiO_2 core@shell structure with tailorable absorption wavelengths from the visible to near-infrared region. This visible light absorption efficiently converts N_2 to NH_3, achieving an apparent quantum efficiency (AQE) of 0.82% at 550 nm. Two possible reaction mechanisms are proposed: 1) Excitation of the Au plasmonic nanoparticles generates hot electrons that pass across the interface Schottky barrier to the conduction band (CB) of TiO_2 (Fig. 1a), resulting to electrons on the TiO_2 CB and holes in Au. This process can be explained in terms of direct or indirect electron ejection. 2) Excitation of the Au plasmon resonance enhances the two-photon absorption from TiO_2 VB to CB (Fig. 1b, 2 photons at 550 nm), forming holes at TiO_2 VB and electrons at CB. To further improve the catalytic performance, it is important to understand dynamics and contribution of hot electron injection. In our recent beamtime at SACLA, we have determined the rise TiO_2 excited states around 5 ps in Ti K-edge fs-XAS, correlating well with the 4.2 ps decay time of Au in the fs-TAS (Fig. 1c), suggesting hot electron injection from Au to TiO_2 is the dominant contributing mechanism. To verify this claim, It is essential to simultaneously measure the Au L3-edge XAS and Ti Kα XES and determining their dynamics with fs resolution.

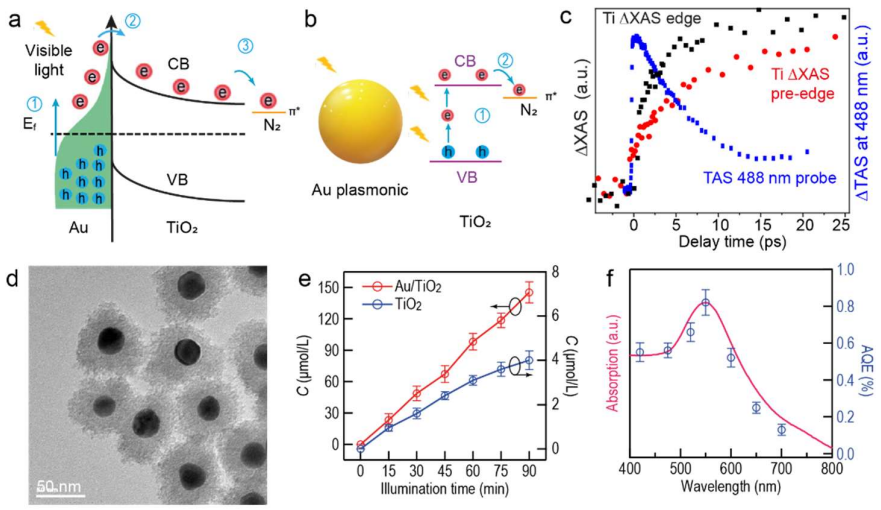

Figure 6-1. a,b the energy diagram of hot electron injection and plasmon enhanced two photon absorption, respectively. **c**, ΔXAS at 4966 (pre-edge) and 4977 eV (edge) and ΔTAS at 488 nm with 550 nm pump as the function of pump-probe delay time. **d**, TEM image of Au@TiO2 particles. **e**, Concentration of NH3 as the function of time. **f,** The adsorption of Au@TiO2 and dependence of AQE as a function of incident wavelength.

Appendix

For Chapter 3

3. 1 Supplementary Note

Note 1. Relative content for Ce^{3+} and Ce^{4+} in catalysts undergoing redox processes

It is difficult to find the standard with pure Ce^{3+} and similar coordination environment to CeO2. And also, in nature, there is no pure Ce^{4+} CeO2. These makes it impossible to do linear combination fitting by pure Ce^{3+} and Ce^{4+} standards. What we did is: 1) getting the relative content of Ce^{3+} and Ce^{4+} for most reduced and oxidated spectra at each condition by curve-fitting of Ce L3-edge XANES. 2) using the most reduced and oxidated spectra at each condition as the standards to do the linear combination fitting for all the spectrum at same condition. Although the error can be relatively larger than the LCF with pure Ce^{3+} and Ce^{4+}, this method is the only way to get the relative content of Ce in catalysts undergoing redox processes, and, the changing trends of Ce redox is accurate as well as the slope of the changing trends.

Note 2. Curve-fitting of Ce L3 edge XANES

The relative fractions of Ce in the most oxidated and reduced condition were calculated according to Equation. 3-5, where Ce^{3+} and Ce^{4+} are the sums of the integrated peak area contributed by the Ce^{3+} and Ce^{4+} respectively from the peak fitting results (supplementary figure. S3-10).

$$[Ce^{3+}] = Ce^{3+}/(Ce^{3+} + Ce^{4+}) \qquad \text{Eq. 3-5}$$

Note 3. Linear combination fitting

To obtain the relative content of Ce^{3+} and Ce^{4+} in catalysts undergoing redox processes, linear combination fitting was conduced by using the most oxidated spectra and most reduced spectra as the standard. The relative fractions of Ce in most oxidated spectra and most reduced spectra were obtained as Note 2. described.

3. 2 Supplementary Figures

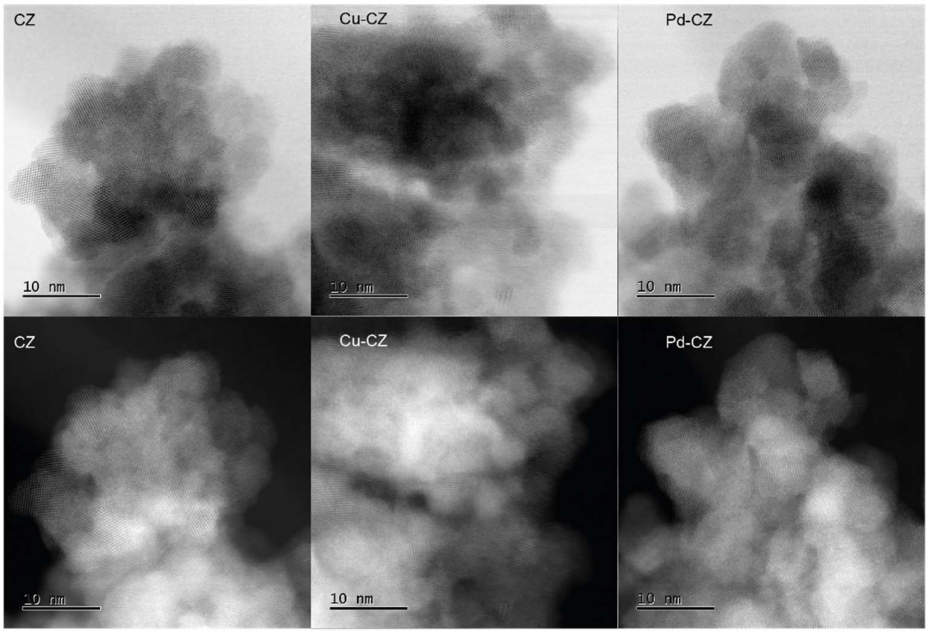

Supplementary Figure S3-1. BF-STEM and HAADF-STEM image for fresh CZ; Cu-CZ and Pd-CZ.

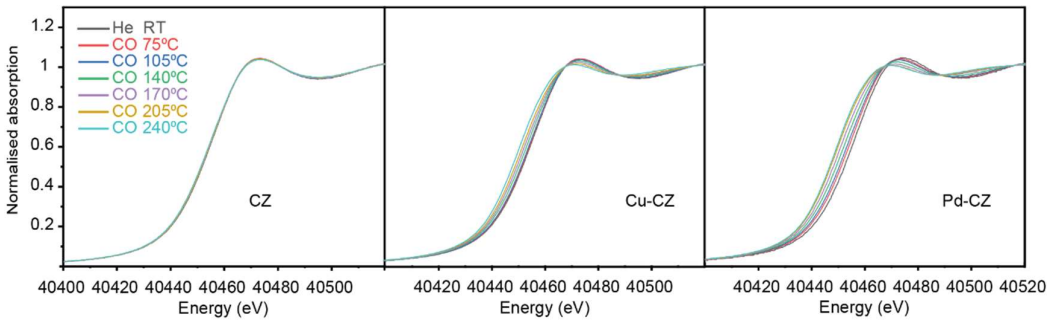

Supplementary Figure S3-2. Ce K-edge of CO TPR (75ºC to 240ºC, 40sccm 10%CO and 160sccm 100% He) for CZ; Cu-CZ and Pd-CZ samples.

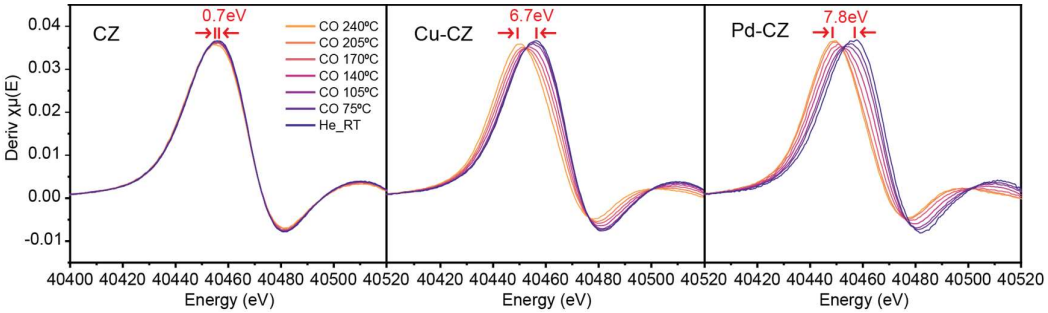

Supplementary Figure S3-3. First derivative of Ce K-edge XANES varies with temperature for pure CZ; Cu-CZ and Pd-CZ.

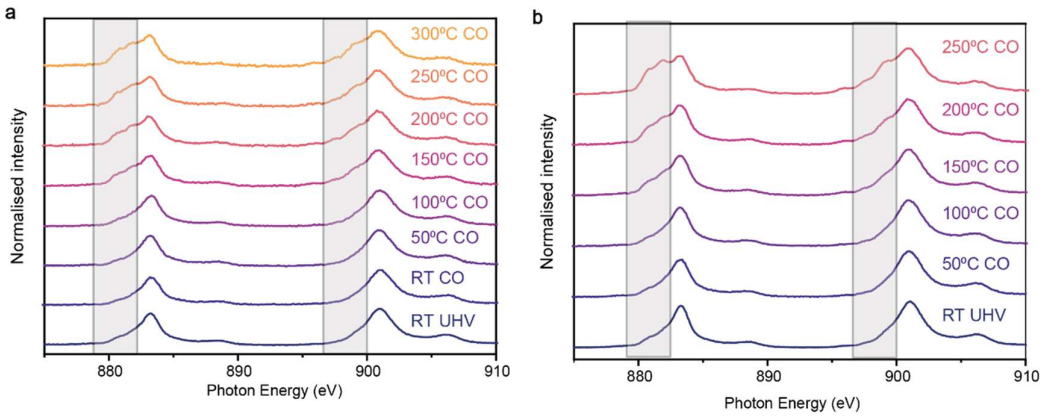

Supplementary Figure S3-4. Ce M4,M5-edge NEXAFS. **a.** CO TPR(5 mbar 100vol% CO, RT to 300ºC) for pure CZ. **b.** CO TPR(5 mbar 100vol% CO, RT to 250ºC) for Pd-CZ.

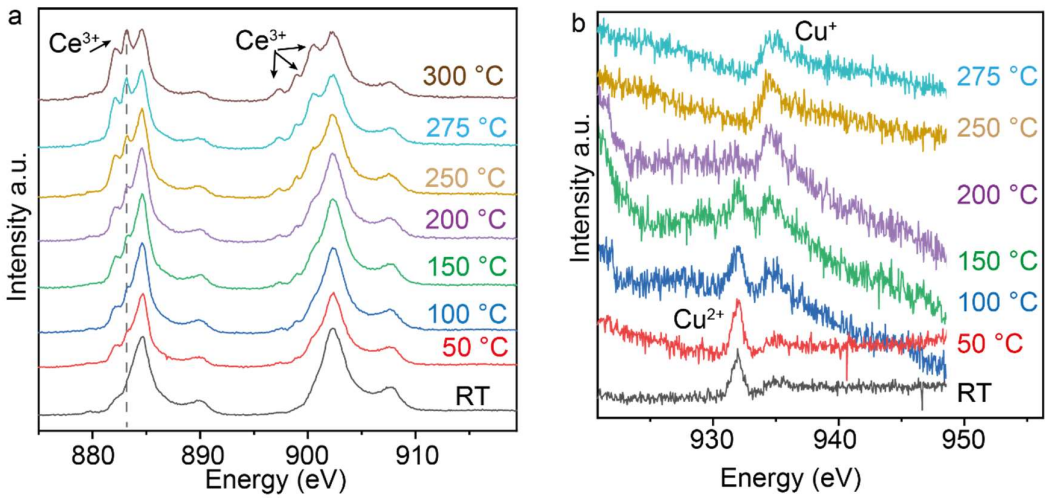

Supplementary Figure S3-5. a. Ce M4,M5-edge NEXAFS for Cu-CZ in CO TPR (5 mbar 100vol% CO, RT to 300ºC) . **b.** Cu L3-edge NEXAFS for Cu-CZ in CO TPR (5 mbar 100vol% CO, RT to 250ºC).

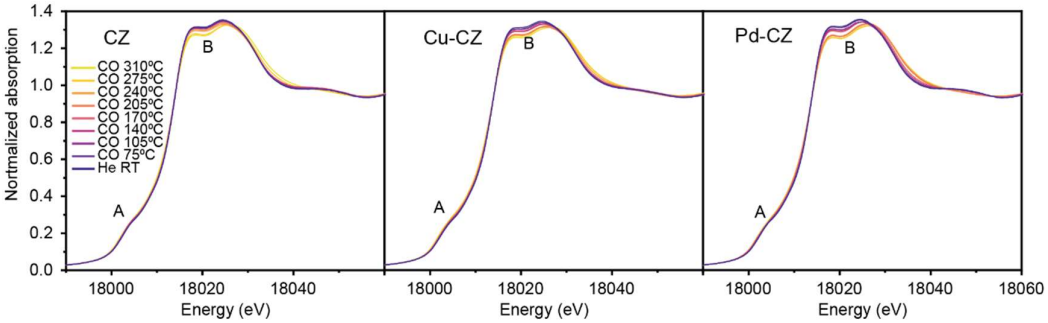

Supplementary Figure S3-6. Zr K-edge of CO TPR (75ºC to 310ºC, 40sccm 10%CO and 160sccm 100% He) for CZ; Cu-CZ and Pd-CZ samples.

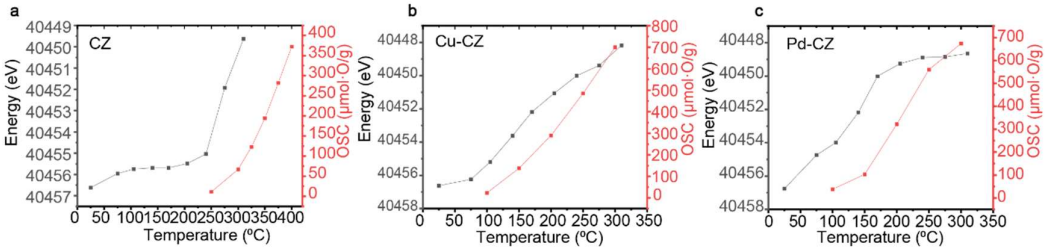

Supplementary Figure S3-7. Ce K-edge XANES absorption edge shift (left black y-axis) and oxygen storage capacity(right red y-axis) for CZ; Cu-CZ and Pd-CZ samples.

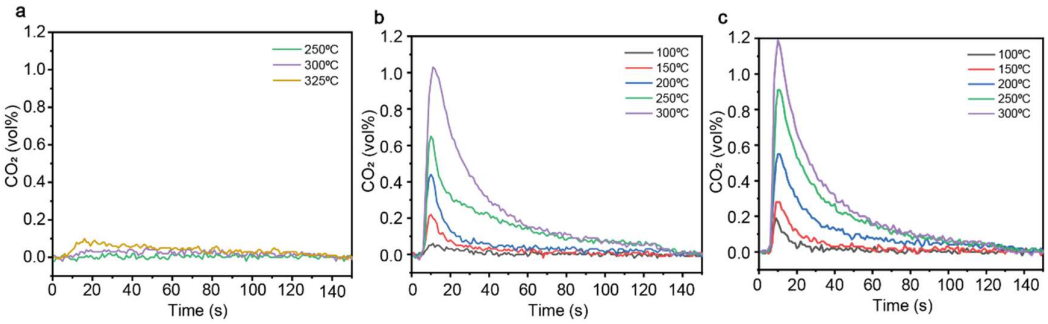

Supplementary Figure S3-8. Oxygen storage capacity measurement for **a.** pure CZ, **b.** Cu-CZ and **c.** Pd-CZ (merged with 10 cycles of gas switch between CO and O_2)

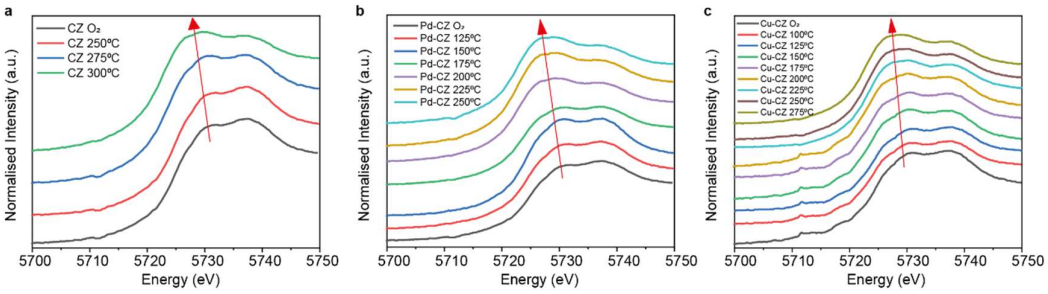

Supplementary Figure S3-9. The most oxidized (in 2vol% O2) and the most reduced in 2vol% CO at each temperature Ce L3-edge XANES from EDE. **a.** for pure CZ. **b.** for Pd-CZ. and **c.** for Cu-CZ.

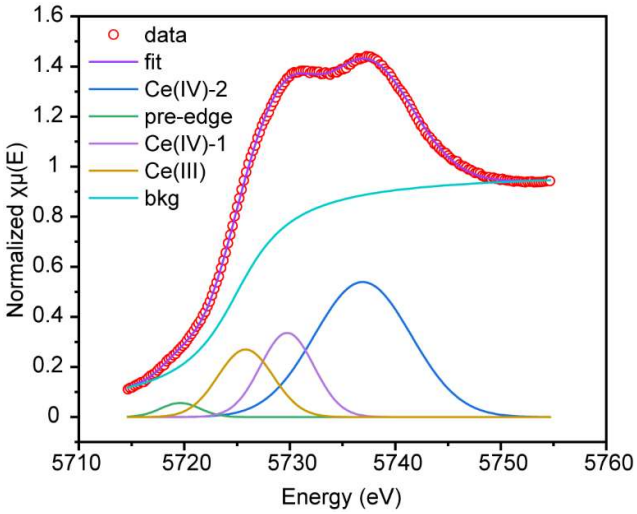

Supplementary Figure S3-10. Ce L3-edge XANES spectrum and fitting peaks of Cu-CZ at 250℃.

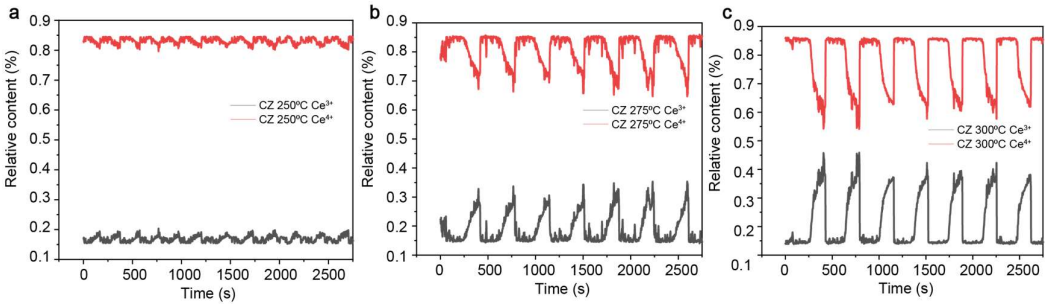

Supplementary Figure S3-11. LCF results from Ce L3-edge XANES for CZ. Relative content of Ce(III) and Ce(IV) during 10 repetitions of gas switching for pure CZ at **a.** 250ºC.**b.** 275ºC. **c.**300ºC

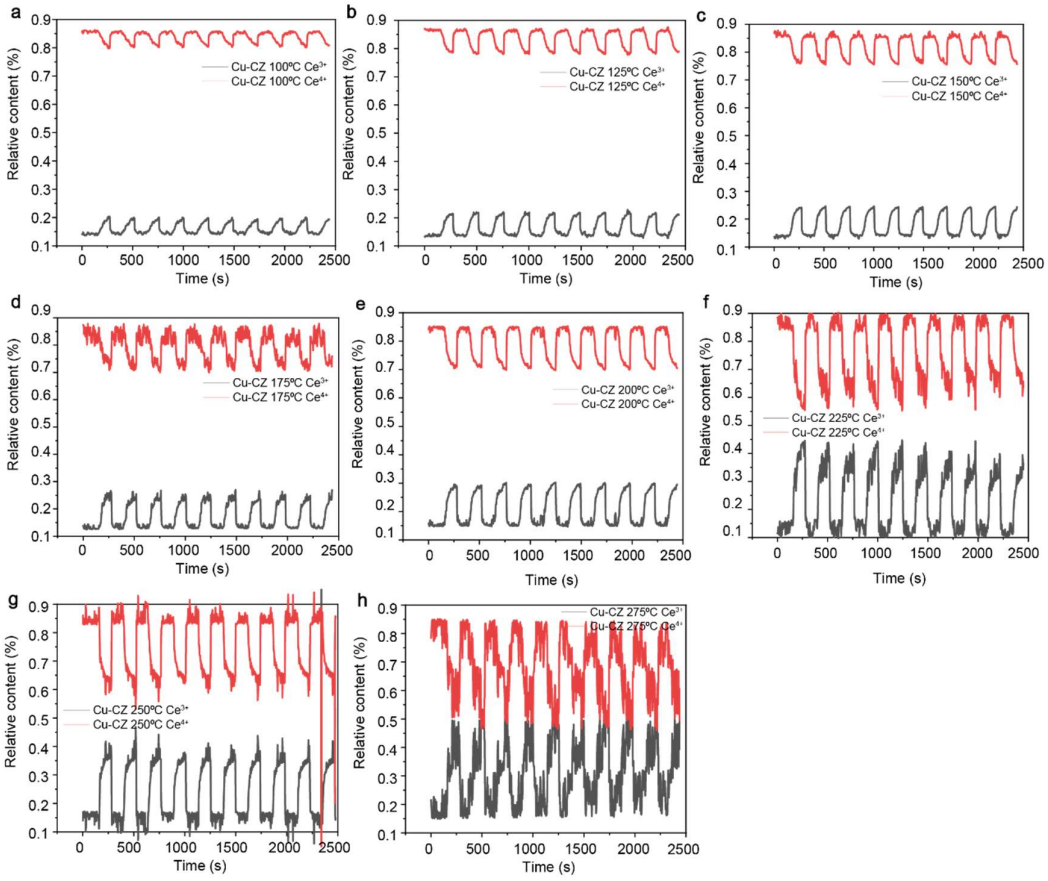

Supplementary Figure S3-12. LCF results from Ce L3-edge XANES for Cu-CZ. Relative content of Ce(III) and Ce(IV) during 10 repetitions of gas switching for Cu-CZ at **a.** 100ºC. **b.** 125ºC. **c.**150ºC. **d.**175ºC. **e.** 200ºC. **f.** 225ºC. **g.** 250ºC. **h.** 275ºC.

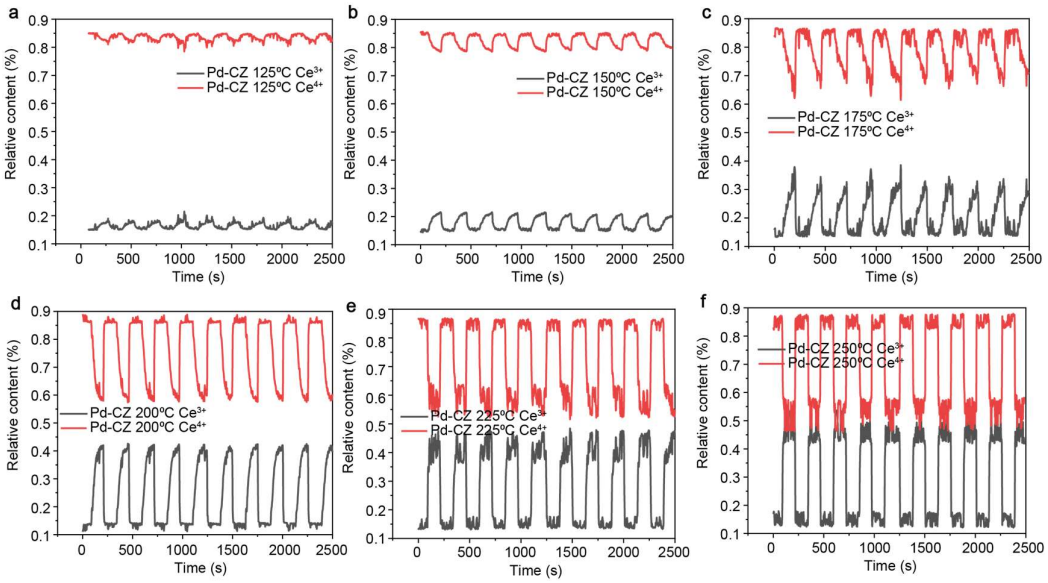

Supplementary Figure S3-13. LCF results from Ce L3-edge XANES for Pd-CZ. Relative content of Ce(III) and Ce(IV) during 10 repetitions of gas switching for Pd-CZ at **a.** 125ºC.**b.** 150ºC. **c.**175ºC. **d.**200ºC. **e.** 225ºC. **f.** 250ºC.

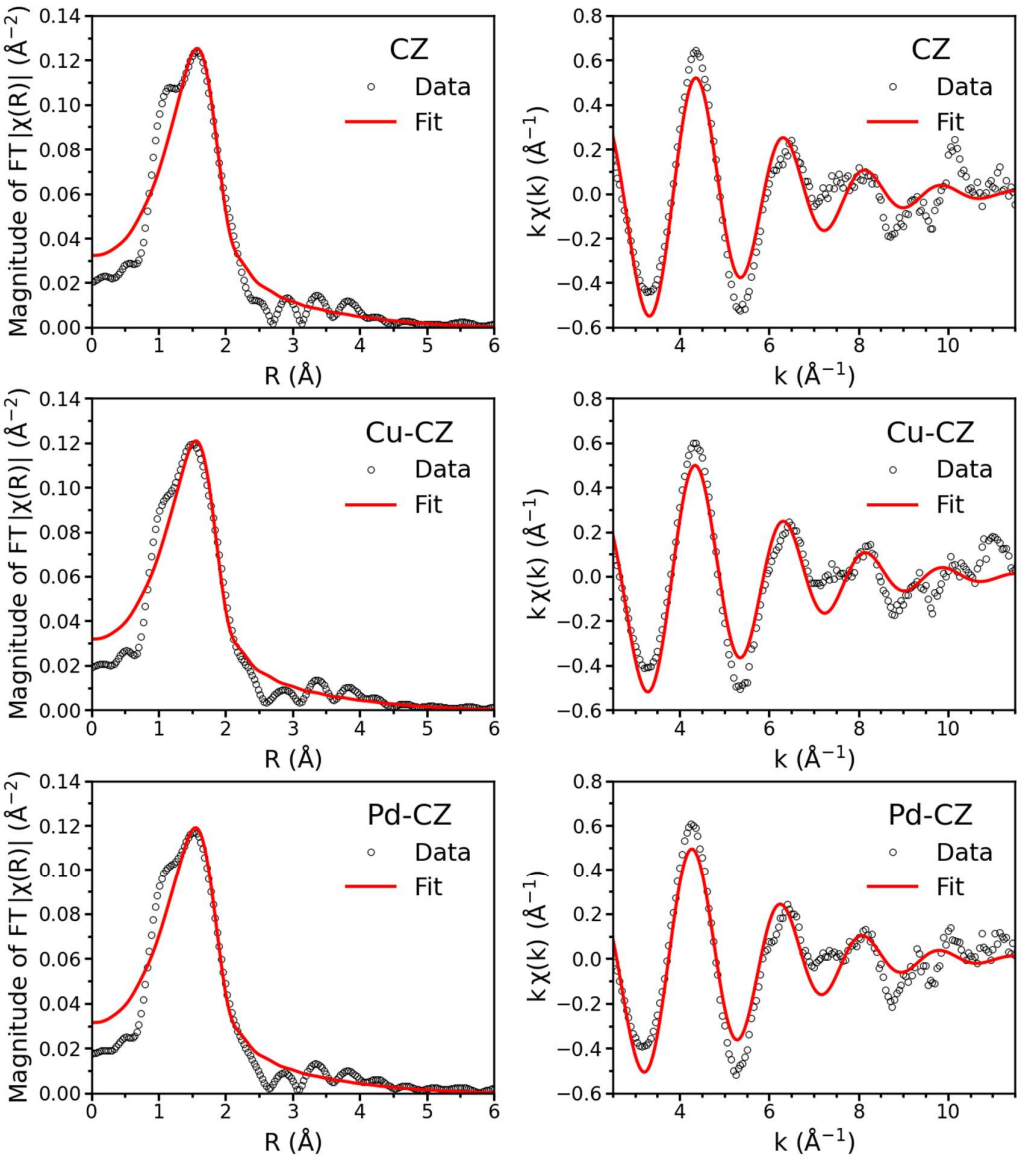

Supplementary Figure S3-13. Ce K-edge EXAFS fitting results for the CZ samples under O_2. The Fourier transform of EXAFS (without phase correction) and k-space (k-weight = 1) of data along with fitted model of the first coordination shell equivalent to the Ce-O bond

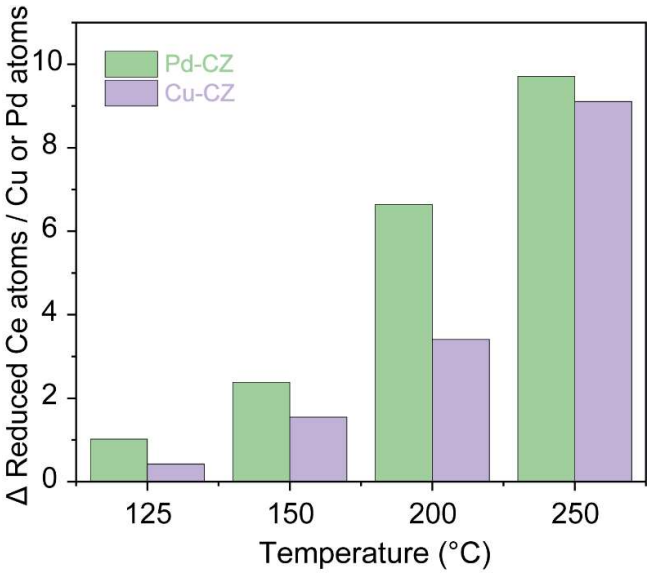

Supplementary Figure S3-14. The amount of reduced Ce atoms promoted by single Cu atom and Pd atom.

3.3 Supplementary Table

Supplementary Table S3-1. Ex-situ EXAFS fitting results of CZ samples.

Sample	Scattering	C.N.	d (Å)	σ^2	E_0 (eV)
CeO2 STD	Ce-O	8	2.35 ± 0.01	0.007 ± 0.002	-1.8 ± 1.1
CZ	Ce-O	8.0 ± 1.4	2.28 ± 0.02	0.015 ± 0.003	-2.5 ± 1.9
Cu-CZ	Ce-O	7.6 ± 1.2	2.26 ± 0.02	0.014 ± 0.003	-4.2 ± 1.7
Pd-CZ	Ce-O	7.8 ± 1.2	2.27 ± 0.03	0.011 ± 0.001	-3.2 ± 1.5

For Chapter 4

4.1 Supplementary figures

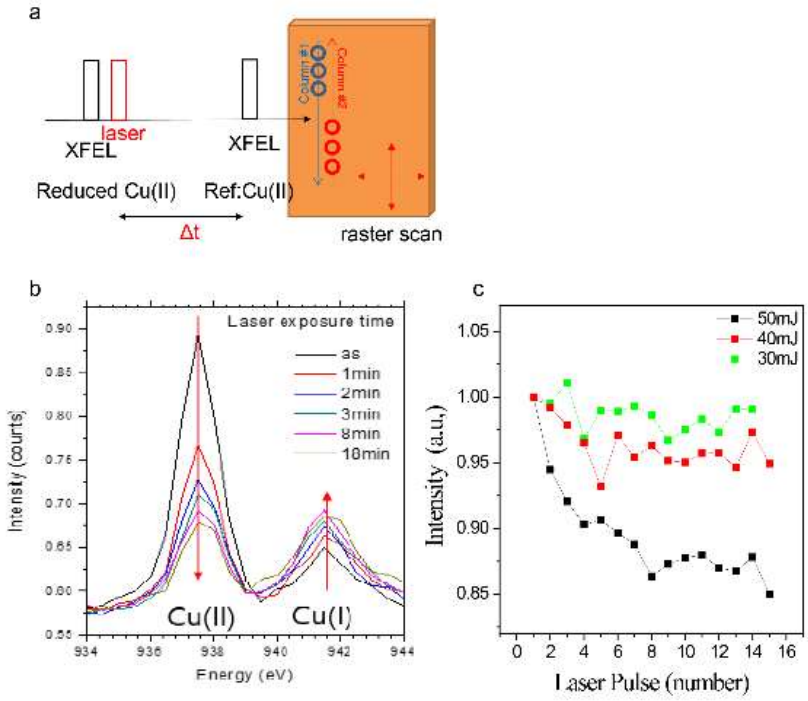

Figure S4-1. a. scheme of raster scan set up. **b.** The change of XAS spectra after exposure to laser with 266 nm wavelength and 25 mJ/cm^2 power with various exposure times. **C.** The change of Cu(II) peak intensity after each single shot exposure of the laser at various powers.

For Chapter 5

5.1 Materials and Method

Nanoparticle Growth

Aqueous 0.1M K_2PdCl_4 (Solution A) was reacted with Solution B (surfactant, ascorbic acid) in a 1:3 ratio for 20 minutes under set reaction conditions of temperature, concentration, capping agent and presence of seeds. Standard reaction conditions were 333.15K with 80mM CTAC and no seed solution. To vary temperatures around the standard 303.15, 313.15, 323.15 and 333.15 K with 80mM ascorbic acid were selected. The effects of seeds at a range of concentrations was tested with 1µL, 10µL, 100µL and 1000µL, of a Pd seed solution directly mixed into solution B.

Seed Solution Preparation

Seed solution was prepared by mixing 250 µL of 0.01 M H_2PdCl_4 solution with 9.5 mL of 0.1 M CTAC and lastly 600 µL of cold 0.01 M $NaBH_4$ solution. The mixture was shaken and left for 2-4hours before use.

TEM imaging

After reacting the two nanoparticle solutions (A and B), at temperature, the reaction could be stopped at different times and nanoparticles removed, to view the reaction progress. To allow separation without agglomeration, formed nanoparticles were centrifuged for 3 minutes at 11000 rpm (xxx g, Fisher Scientific). Solid residue was washed with ethanol thrice before redispersion for loading on a TEM grid. JEOL 2100 TEM 200kV was operated at UCL.

XAFS measurement

In situ XAFS was carried out using the SFM-3000 stop flow cell operated at the I20-EDE beamline, Diamond Light Source. Cell reservoirs were filled with reaction

solutions A and B, as well as water and HCl for washing. The dead volume of the cell was approximately 40 µL, so 400 µL of reactants were injected per trial. Acid and water wash were carried out after each trial. Temperature of the cell and reservoirs were maintained with a Lauda hot water flow, and sample temperature was calibrated before the experiment with a thermostat at the XAFS measurement position.

The r-space and k-space were refined using Dawn software which allows the mass processing of large data sets. Principal Component Analysis was run to see the changes in the oxidation state in the XANES region of the curve. Selected points were then processed further using Artemis (Demeter Suite Software) to resolve the bonds present in the sample and estimate the Pd-Pd coordination at different reaction times.

The presence of chloride and oxide bonds is observed but cannot be reliably resolved as the bond lengths are similar. One way to test between the two is to look at changes to the k-space after different weightings.

XAFS Batch Analysis

The Energy Dispersive EXAFS (EDE) data were processed using inhouse developed python scripts. The raw XAFS data as well as the metadata obtained from I20-EDE beamline at Diamond Light Source (UK) were saved in nexus format and were first imported using the h5py package.[37] To analyse the imported XAFS spectra, the XANES part before 24015 eV and the EXAFS part after 25563 eV were truncated, and then each individual XAFS spectra was smoothed by the Savitzky-Golay filter using the scipy package. The further data processing including pre-edge subtraction, post-edge normalisation, background determination and Fourier Transform were performed using xraylarch (version 0.9.58).[38]

The normalisation was performed using E_0 value of 24357 eV, with background subtraction between -200 and -75 eV (relative to the edge), normalisation range of 150 to 1000 eV (relative to edge) and normalisation order of 2. R-space background removal

(rbkg) was set to 1 Å. For the k-space transformation, a weighting of 2 was selected along with a Hanning window between 3.0 to 12.5 $Å^{-1}$.

In addition to the *in situ* experiment, XAFS of K_2PdCl_4 solution and Pd metal foil were measured as reference spectra and were used for the Linear Combination Fitting (LCF). The linear combination fitting was performed using the non-linear least-square fitting method built in the lmfit package.[39] The LCF energy range was set to 24,300 eV to 24,420 eV (160 data points in total) for all XANES spectra, and the sum of two components ($PdCl_2$(aq) and Pd metal) were fixed to be 100%.

To fit the R-space EXAFS spectra, two single scattering paths: Pd-Cl from $PdCl_2$ structure and Pd-Pd from Pd metal were first generated using the FEFF8L package.[40] The two scattering paths were imported as the fitting model. The EXAFS spectra ($1.0 < k < 12.0$, $1.0 < R < 3.0$) were then fitted using the non-linear least-square fitting method built in the lmfit package.[39]

To accelerate the processing of the large amount of XAFS results produced from the beamline in EDE mode (1 second/spectra, in total more than 200,000 spectra), the LCF and EXAFS fitting were parallelly processed by the joblib tool using 16 CPU cores (32 threads).

SAXS Measurement and Analysis

SAXS was performed at the I-22 beamline, Diamond light source (session SM29090-1). Solutions were placed at temperature in the beam path using the same stop-flow cell used for XAFS measurements, allowing comparable reaction conditions.

SAXS data analysis was performed using SAXSGUI (v5.05) using Indirect Fourier transformation (IFT) analysis. SAXS spectra obtained during this work were fitted following this model in the q-range between 0.01 to 0.18 nm^{-1}. IFT of the scattering data allowed the pair distance distribution *P(r)* calculation. The scattering intensity *I(q)* is related to *P(r)* following Equation s5-1.

$$I(q) = 4\pi \int_0^\infty P(r) \frac{\sin qr}{qr} dr \qquad \text{Eq.s5-1}$$

Where q is the absolute value of the scattering vector. This methodology allows the calculation of basic structural parameters of the system such as nanoparticle shape or size following an absolutely model-free approach. Thus, P(r) function provides accurate structural information about the maximum dimension (D_{max}) and the radius of gyration (R_g) of the nanoparticle. Moreover, the shape of the P(r) function can also be directly related to the overall shape of the nanoparticles, such as spherical vs. elongated particles or whether the nanoparticle contains multiple domains.

MP-AES readings

Agilent MP-AES 4200 was used to compare metal content remaining in solution versus that in formed metallic Pd nanoparticles, at two minute intervals during the reaction. Pd standard solution was acquired from Sigma Aldrich (1000 ppm) and diluted between 1 ppm and 50 ppm for calibration before each use, with a maximum error of 7% and total dissolved solids were below 2%. Reactants centrifuged at 30,000 rpm (Eppendorf) were separated solid from liquid. 1mL nitric acid (70%, Sigma Aldrich) was added to both solid and liquid samples for a similar matrix solution, before dilution to ~10 ppm for measurements. CTAC was included in the matrix background measurement as nanoparticles were not washed.

5.2 Supplementary Notes

Note S5-1. Calculating concentration of ligand-mediated Pd^0 growth species (Pd^0-Cl)

First, the assumption is made that the total number of Pd atoms in the measured system (N) is a constant, as this is a closed system. This could have potential errors as we only see the Pd atoms which are in the beam path, but we do not observe a trend of change in Pd concentration, as particle movement seems to be random. To this value closer to reality, we use the edge jump as a measure of the trend of changes of Pd concentration in the system, as low Pd concentration leads to less absorption and smaller edge jump.

$$\mathrm{N} = \mathrm{NPd^{2+}\text{-}Cl} + \mathrm{NPd^{0}\text{-}Cl} + \mathrm{NPd^{0}\text{-}Pd} \qquad \text{eq.s5-2}$$

The fraction of Pd^0 and Pd^{2+} is given by χ,

$$\chi\mathrm{Pd^{2+}} = \frac{\mathrm{NPd^{2+}\text{-}Cl}}{\mathrm{N}} \qquad \text{eq.s5-3}$$

And

$$\chi\mathrm{Pd^{0}} = \frac{(\mathrm{NPd^{0}\text{-}Cl} + \mathrm{NPd^{0}\text{-}Pd})}{\mathrm{N}} \qquad \text{eq.s5-4}$$

Therefore

$$\chi\mathrm{Pd^{2+}} + \chi\mathrm{Pd^{0}} = 1 \qquad \text{eq.s5-5}$$

The second assumption is that coordination number is constant. Pd atoms are always bonded or interacting with close neighbour atoms, whether another Pd atom, Cl or O from aqueous solution. We do not assume that it is always (or ever) fully coordinated, but that 'aqueous Pd0' may still have Pd-Cl or Pd-O interactions visible in EXAFS. Our finding is that Pd-O bonds are not in present or are included in the Pd-Cl bond fitting and cannot be distinguished. This can be made more precise by plotting the total coordination number of Pd in the system over time.

The fraction of coordination to each element from the Pd is given by:

$$\mathrm{CN} = (2 \times [\mathrm{Pd\text{-}Cl}]) + [\mathrm{Pd\text{-}Pd}] \qquad \text{eq.s5-6}$$

$$\varphi_{\mathrm{Pd\text{-}Cl}} = \frac{[\mathrm{Pd\text{-}Cl}]}{[\mathrm{Pd\text{-}Cl}]_{\mathrm{initial}}} \qquad \text{eq.s5-7}$$

$$\varphi_{\mathrm{Pd\text{-}Pd}} = \frac{[\mathrm{Pd\text{-}Pd}]}{[\mathrm{Pd\text{-}Pd}]_{\mathrm{final}}} \qquad \text{eq.s5-8}$$

$$\varphi_{\mathrm{Pd\text{-}Cl}} + \varphi_{\mathrm{Pd\text{-}Pd}} \qquad \text{eq.s5-9}$$

The third assumption is that the breaking and formation of chemical bonds is faster than the recorded (millisecond) timescale. We do not observe intermediate states of bond formation.

At the initial stage of the reaction, when no nanoparticles are present, $Pd^0 = 0$, the XANES normalised average number of Pd with 2+ oxidation state is 100%

$$\chi Pd^{2+}{}_{initial} = 1, \quad \chi Pd^{0}{}_{initial} = 0 \qquad \text{eq.s5-10}$$

The initial total coordination fractions are given by

$$\varphi_{Pd\text{-}Cl} = 1, \ \varphi_{Pd\text{-}Pd} = 0 \qquad \text{eq.s5-11}$$

In the reduction stage,

$$\chi Pd^{2+} = \frac{\{Pd^{2+}\text{-}Cl\}}{\{Pd^{0}+Pd^{2+}\}} \qquad \text{eq.s5-12}$$

And

$$\chi Pd^{0} = \frac{\{Pd^{0}\text{-}Cl\}+\{Pd^{0}\text{-}Pd\}}{\{Pd^{0}+P^{2+}\}} \qquad \text{eq.s5-13}$$

$$\varphi_{Pd-C} = \frac{[Pd\text{-}Cl]}{[Pd\text{-}Cl]_{initial}} \qquad \text{eq.s5-14}$$

$$\varphi_{Pd^{0}\text{-}Cl} = \varphi_{Pd\text{-}Cl} - \chi Pd^{2+} \qquad \text{eq.s5-15}$$

$$[Pd^{0}\text{-}Cl] = [Pd\text{-}Cl] - \chi Pd^{2+}[Pd\text{-}Cl]_{initial} \qquad \text{eq.s5-16}$$

If we calculate the Pd-Pd bonding,

$$\varphi_{Pd\text{-}Pd} = \frac{[Pd\text{-}Pd]}{[Pd\text{-}Pd]_{final}} \qquad \text{eq.s5-17}$$

$$\varphi_{Pd^{0}\text{-}Pd} = \chi Pd^{0} - \varphi_{Pd\text{-}Pd} \qquad \text{eq.s5-18}$$

$$[Pd^{0}\text{-}Pd] = \chi Pd^{0}[Pd\text{-}Pd]_{final} - [Pd\text{-}Pd] \qquad \text{eq.s5-19}$$

$$[Pd^{0}\text{-}Pd] = [Pd\text{-}Pd] - [Pd^{0}\text{-}Cl] \qquad \text{eq.s5-20}$$

Thus, using parameters that we can measure with XANES and EXAFS, the Pd0 in solution can, based on this theory, be quantified.

Experimental Pd Concentration:

100mM Pd was added in the ratio 160 μL:350 μL with the reduction solution. The initial concentration of the Pd in the solution is 0.0314M or 31.4mM. Assuming that the Pd is always in the beam path, this value does not change.

Pd^0-Cl Concentration:

Using total Pd concentration, the maximum concentration of Pd^0-Cl could be calculated. The % of Pd-Cl bonds which are Pd^0-Cl and then use that to estimate the minimum possible concentration, assuming the case where the Pd^0-Cl has the same average number of Pd-Cl bonds.

Note S5-2. Modelling Nanoparticle Growth

I. Precipitation Model

Palladium nanoparticle precipitation can be described by a three-step mechanism involving: i. reduction of the Pd precursor, ii. nucleation, and iii. growth of the Pd nanoparticles (NPs). The dynamic evolution of the chemical species involved in the process can be described by coupling the material balance of Pd2+/Pd0 in solution with a population balance describing the nucleation and growth of NPs. The population balance reads:

$$\frac{\delta f}{\delta t} + \frac{\delta(\upsilon f)}{\delta \tilde{n}} = 0 \qquad \text{eq.s5-21}$$

With boundary conditions

$$n(0,t) = \frac{J}{\upsilon} \qquad \text{eq.s5-22}$$

where n is the number density of NPs, t is time, ñ is number of atoms in a Pd cluster, v is the growth rate, J is the nucleation rate, and S is supersaturation. The material balances of the chemical species involved in the process can be described by the following differential material balances:

$$\frac{dC^{aq}_{Pd^{2+}}}{dt} = -k^{+}\, C^{aq}_{Pd^{2+}}\, C^{aq}_{AA} + k^{-} C^{aq}_{Pd^{0}} \qquad \text{eq.s5-23}$$

$$\frac{dC^{aq}_{Pd^{0}}}{dt} = k^{+}\, C^{aq}_{Pd^{2+}}\, C^{aq}_{AA} - k^{-} C^{aq}_{Pd^{0}} - \frac{1}{N_A}\int_0^{\infty} v\tilde{n}^{2/3}\, f d\tilde{n} \qquad \text{eq.s5-24}$$

$$\frac{dC^{aq}_{AA}}{dt} = -k^{+}\, C^{aq}_{Pd^{2+}}\, C^{aq}_{AA} \qquad \text{eq.s5-25}$$

Where $C^{aq}_{Pd^{2+}}$, $C^{aq}_{Pd^{0}}$ and C^{aq}_{AA}, are the aqueous concentrations of Pd^{2+}, Pd^{0}, and ascorbic acid (AA), respectively, and k^+, k^- are the forward and backward reaction constants for Pd^{2+} reduction.

Dimensionless formulation

The material and population balances can be recast in dimensionless form by defining dimensionless time $\tau = t/t_{ref}$ and concentrations $\chi_i = C_i/C_{ref}$. The reference time t_{ref} and concentration C_{ref} were defined as:

$$t_{ref} = 1$$

$$t_{ref} = \frac{1}{k^+ C_{AA(0)}} C_{ref} = C^{aq}_{Pd^{2+}}(0) \qquad \text{eq.s5-26}$$

This choice of t_{ref} allows to formulate the characteristic times of all the processes at play, relative to the characteristic frequency of the reduction process. The differential material balances for Pd^{2+}, Pd^{0}, and AA thus become:

$$\frac{\chi_{2+}}{d\tau} = -\chi_{2+}\xi_{AA} + \kappa\chi_0 \qquad \text{eq.s5-27}$$

$$\frac{\chi_0}{d\tau} = \chi_{2+}\xi_{AA} - \kappa\chi_0 - \int_0^\infty \nu\tilde{n}^{2/3}\, F d\tilde{n} \qquad \text{eq.s5-28}$$

$$\frac{d\xi_{AA}}{d\tau} = -\frac{1}{\varepsilon_{AA}}\chi_{2+}\xi_{AA} \qquad \text{eq.s5-29}$$

Where the variable $\xi_{AA} = \frac{C_{AA}}{C^0_{AA}}$ represents the conversion of ascorbic acid, while the parameter $\varepsilon_{AA} = \frac{C_{AA(0)}}{C_{Pd^{2+}(0)}}$ is the excess of ascorbic acid, and $F = f/N_A C^{aq}_{Pd^{2+}}(0)$ is the dimensionless particle number density. The parameter $\kappa = \frac{k^-}{k^+ C_{AA(0)}}$ is the dimensionless kinetic constant of the oxidation reaction, and represents the characteristic rate of the oxidation reaction relative to the rate of reduction. Adopting consistent reference time and concentration, the population balance in dimensionless form becomes:

$$\frac{\delta F}{\delta \tau} + \frac{\delta(\upsilon F)}{\delta \tilde{n}} = 0 \qquad \text{eq.s5-30}$$

with boundary conditions:

$$F(0,\tau) = \frac{\varphi}{\nu} \qquad \text{eq.s5-31}$$

Where $\nu = \frac{\upsilon}{k^{+}C_{AA}(0)}$ is the dimensionless growth rate, and $\varphi = \frac{J}{N_A\, k^{+} C^{aq}_{Pd^{2+}}(0)\, C_{AA}(0)}$ is the dimensionless nucleation rate. The dynamics of the process can thus be represented by the evolution of the dimensionless concentrations χ_0 and χ_{2+}, together with the evolution of the particles number density $F(\tilde{n})$. The relevant timescales at play are captured by the parameters κ, ν and φ. Governing the rate of oxidation, nucleation, and growth relative to the reduction process. In addition to the relevant timescales the dynamics of this system depends on the excess of reducing agent (ε_{AA}). For large excesses of ascorbic acid, the system simplifies further, i.e. $\lim_{\varepsilon_{AA}\to\infty} \frac{\delta\xi_{AA}}{dt} = 0$.

II. Precipitation and Leaching Model

Leaching can be modelled as a process of re-oxidation of Pd^0, which can in a first instance modelled with a first order dependence on the total surface of the NPs, which leads to the formation of Pd^{2+} in the NPs. This process can be modelled by introducing an expression for μ_{2+}, the dimensionless mass of Pd^{2+} in the NPs, which reads:

$$\frac{d\mu_{2+}}{d\tau} = \lambda \mu_0^{2/3} \qquad \text{eq.s5-32}$$

where λ is a characteristic dimensionless rate of reoxidation of the Pd^0 in the NPs, and $\mu_0^{2/3}$ is the dimensionless total surface of the Pd NPs. The total dimensionless mass of Pd^0 in the NPs is described as:

$$\frac{d\mu_0}{d\tau} = -\lambda \mu_0^{\frac{2}{3}} + \int_0^{\infty} \nu \tilde{n}^{2/3}\, F d\tilde{n} \qquad \text{eq.s5-33}$$

III. Dependence of φ, and ν on Supersaturation.

The dependence on supersaturation of the nucleation, growth and leaching characteristic dimensionless rates is key to couple the population balance defining the NP size distribution and the material balances of Pd in solution. Here we define as S_0 the supersaturation of the solution environment with respect to Pd^0 aq, and S_{2+} the supersaturation of the solution with respect to Pd^{2+}. The characteristic dimensionless rates of nucleation φ and growth ν are expressed as functions of S_0 as:

$$\nu = (S_0 - 1)\nu_0 \qquad \text{eq.s5-34}$$

And:

$$\varphi = S_0 \varphi_0 e^{-\frac{\varphi_1}{(\ln\ o)^2}} \qquad \text{eq.s5-35}$$

Note S5-3. Fitting LCF Athena

Linear combination fittings were performed using Pd foil and PdO as standards to represent Pd(0) and Pd(II). The XANES regions were fitted to the data, within a range of -20 eV to 30 eV from E_0. Sum of all weights was set to 1, so that the composition of the given oxidation states is obtained as a % of the total.

Note S5-4. Calculating activation energy

The activation energy of the reaction could be calculated from the slope of the LCF. The Pd^{2+}% was used to calculate the mM conversion and therefore the activation energy, which is given in kJ/mol. The Pd^{2+} content was converted to molar from starting concentration of 31.4mM, to calculate reaction rate.

According to the Arrhenius Equation, $k = Ae^{\frac{-E_a}{RT}}$

Activation energy (Ea) is calculated by multiplying the gas constant (R = 8.314 $J.mol^{-1}.K^{-1}$) with the slope from a plot of the natural log of reaction rate (k) and inverse temperature (T) in Kelvin. The pre-exponential factor (A) is not included. This was repeated with different ranges to calculate errors in the system, with values varying from 19.8 kJ/mol to 24.7 kJ/mol.

4.3 Supplementary Figures

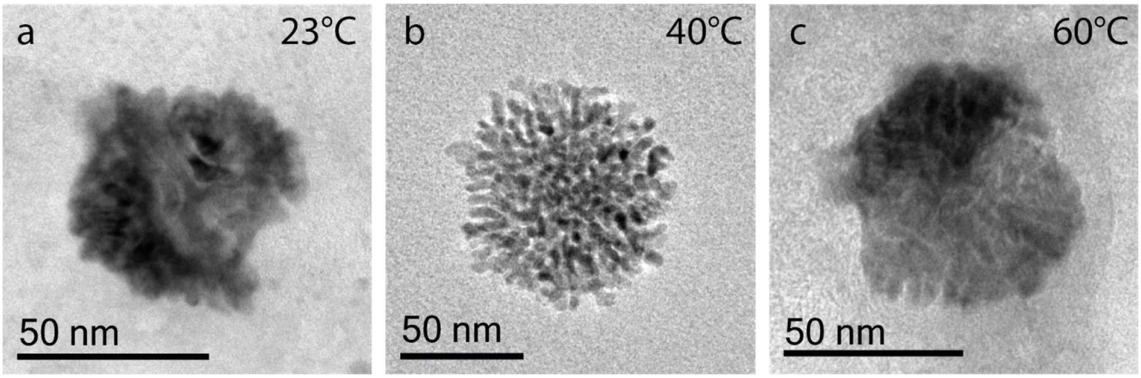

Figure S5-1. Nanoparticles formed at different temperatures. TEM images show the shape and size of particles formed at (a) 23ºC, (b) 40ºC and (c) 60ºC.

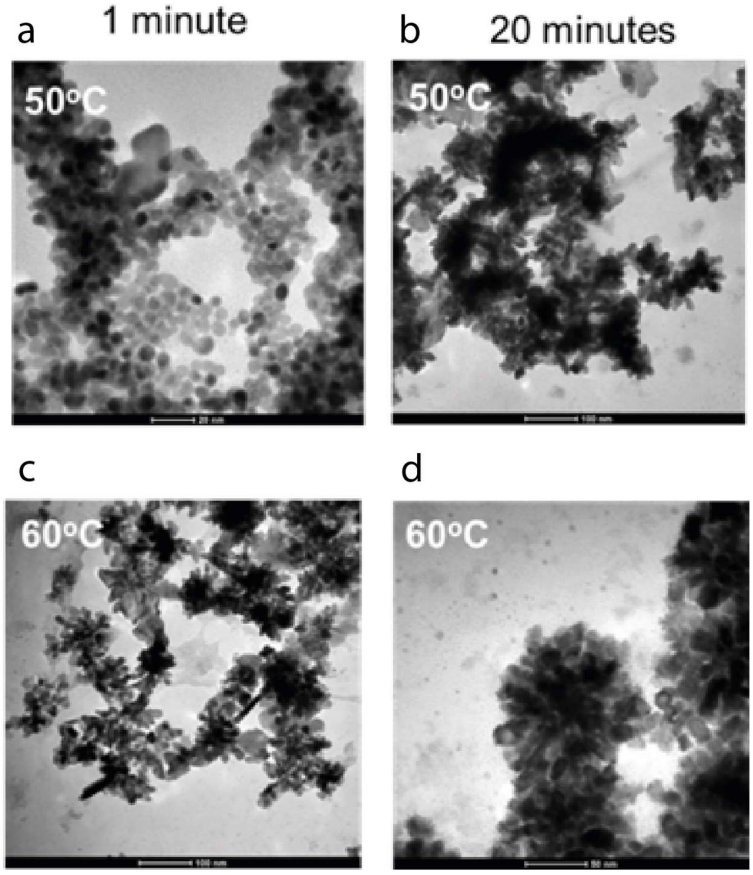

Figure S5-2. Morphology time series. TEM images show the morphology of nanoparticles formed at 50ºC (a, b) and 60ºC (c, d) after 1 (left) and 20 minutes (right) of reaction.

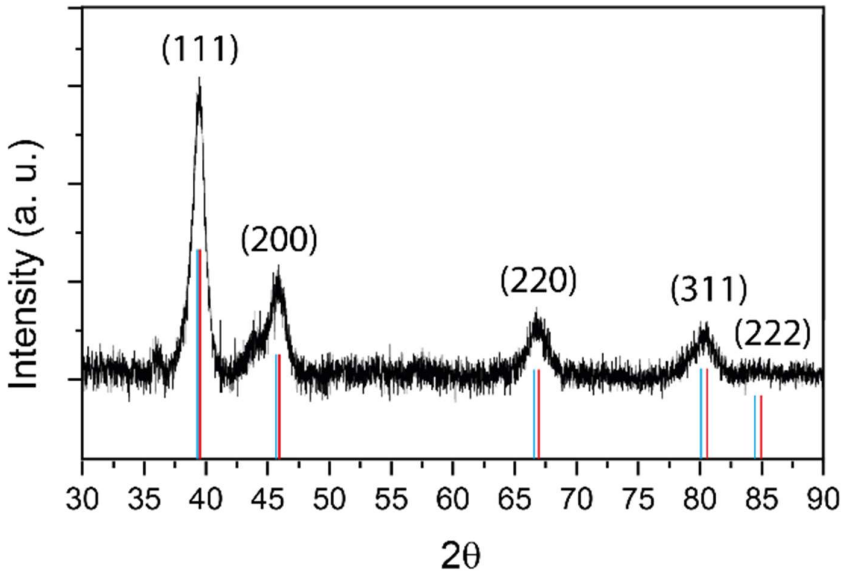

Figure S5-3. XRD results of CTAC-capped Pd nanoparticles grown for 20 minutes. Literature 2θ values for Pd (red lines) are shown for Miller indices of (111), (200), (220), (311) and (222). FCC crystal structure is present with lattice constants, a, calculated as 3.96 ± 0.006 Å. All peaks were detected within the sample, with sharp (111) peak.

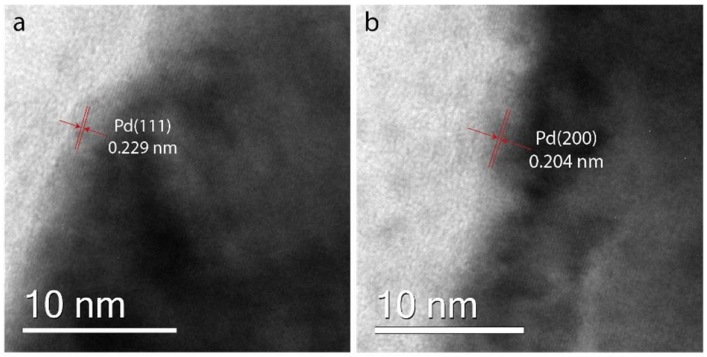

Figure S5-4. Lattice spacing in crystalline Pd nanoparticles. (a) Pd(111) and (b) Pd(200) facets were read from lattice spacings of 0.229 nm and 0.204 nm, respectively. Nanoparticles were grown at 60ºC.

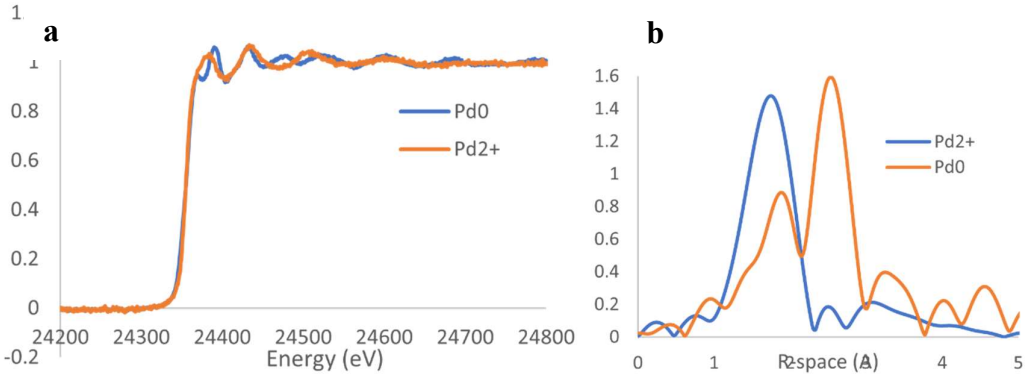

Figure S5-5. (a) Pd K-edge XANES and (b) Pd K-edge EXAFS of Pd^0 (blue) and Pd^{2+} (orange) standards for LCF and kLCF fitting.

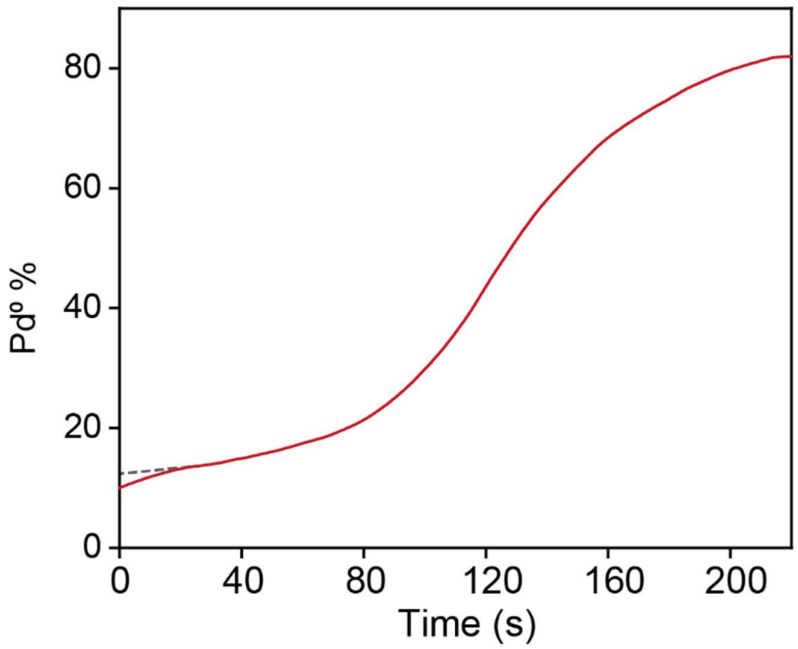

Figure S5-6. A closer view of the reduction phase from 0-20s reaction time, before the typical sigmoidal curve of Pd^{0}% content calculated from Pd K-edge XANES.

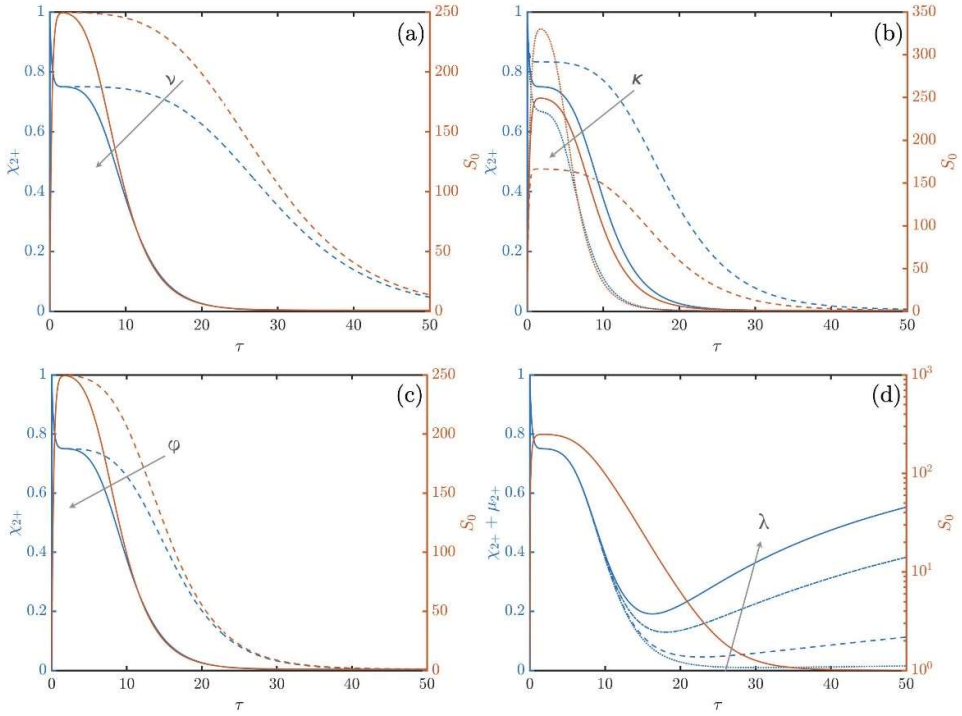

Figure S5-7. Modelling the growth parameters, Dependence of the χ^{2+} profile in dimensionless time τ on (a) the growth rate ν, (b) the oxidation rate κ, (c) the nucleation rate φ, and (d) the leaching rate λ.

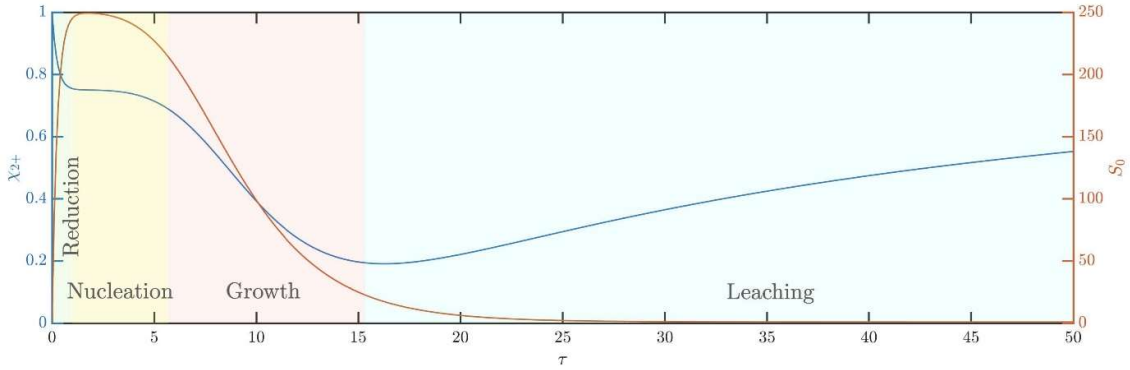

Figure S5-8. A typical evolution of the dimensionless concentration of Pd^{2+}, χ^{2+}, on which the synthesis process is broken down in four different phases: (i) Reduction - where the dominating process withdraws Pd^{2+} from solution, (ii) Nucleation, (iii) Growth, and finally (iv) Leaching, that produces Pd^{2+}.

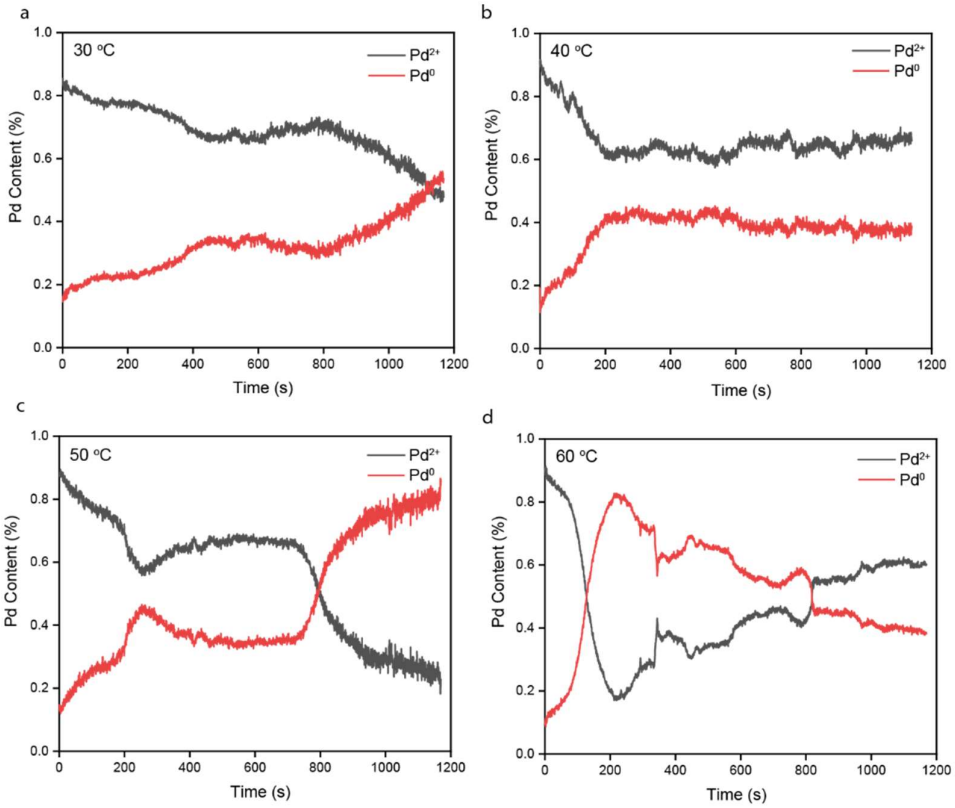

Figure S5-9. Linear combination fitting of the Pd K-edge XANES regions for Pd reduction at temperatures of (a) 30ºC, (b) 40ºC, (c) 50ºC and (d) 60ºC with Pd^{2+} in black and Pd^{0} in red. Standards for Pd^{2+} and Pd^{0} were fresh H_2PdCl_4 solution in water and Pd foil, respectively.

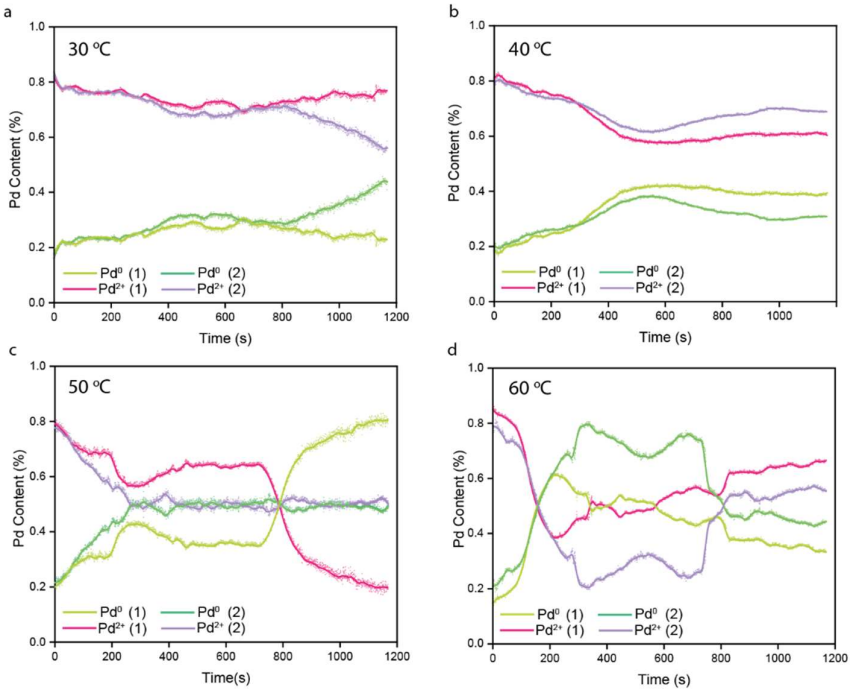

Figure S5-10. Linear combination fitting of the Pd K-edge XANES versus linear combination fitting of the k-space (EXAFS region, 0 to 10 $Å^{-1}$) for temperatures of (a) 30ºC, (b) 40ºC, (c) 50ºC and (d) 60ºC.

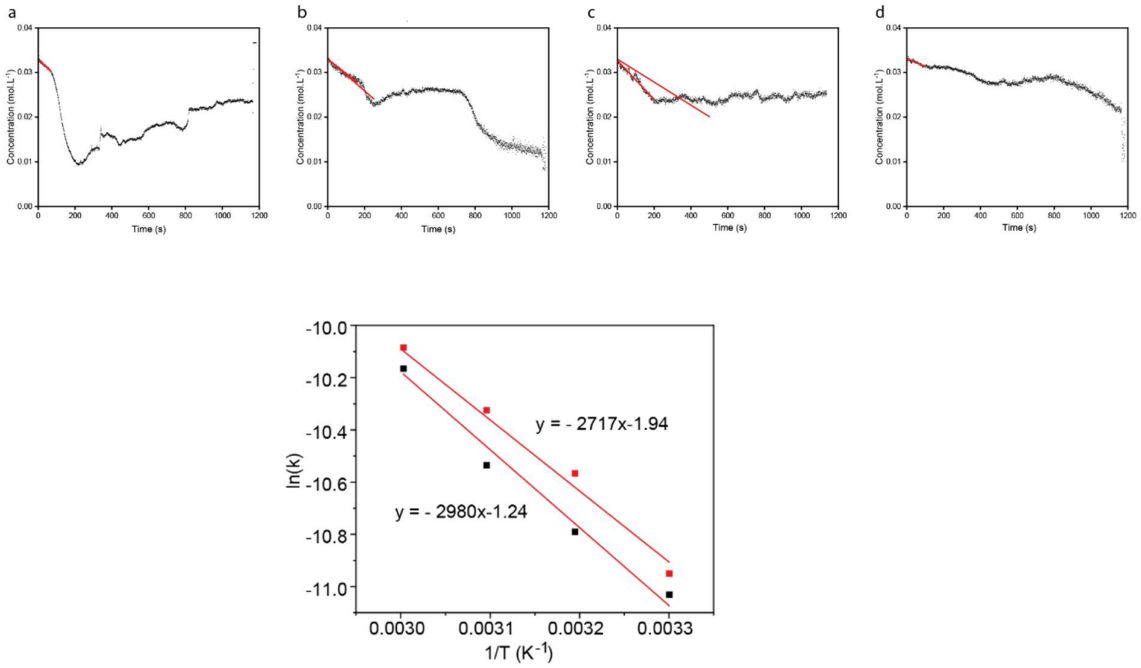

Figure S5-11. Arrhenius plot. Red marked initial region of linear combination fitting of the Pd K-edge XANES at temperatures of (a) 60ºC, (b) 50ºC, (c) 40ºC and (d) 30ºC, alongside (e) an Arrhenius plot from the nucleation range.

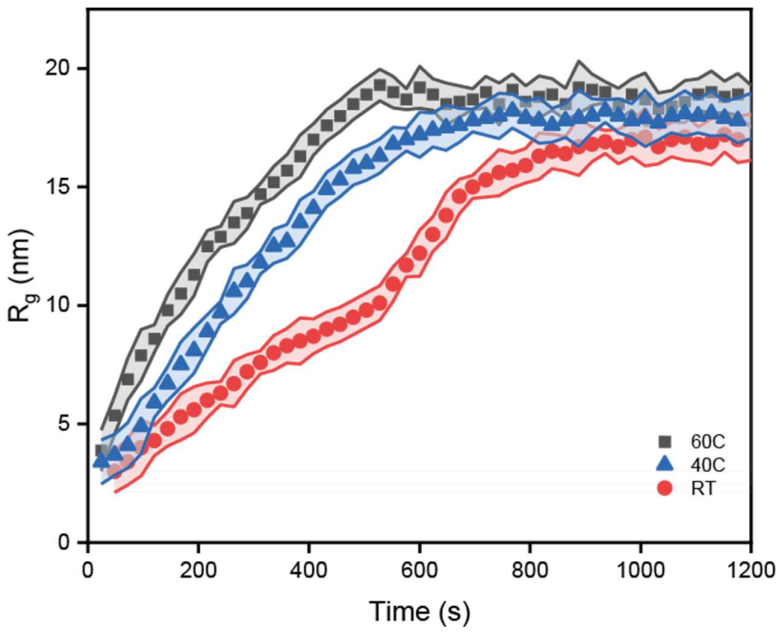

Figure S5-12. Comparison of SAXS curves measured at 22°C (red, circles), 40°C (blue, triangles) and 60°C (grey, squares) shows the change in rate of change in nanoparticle radius.

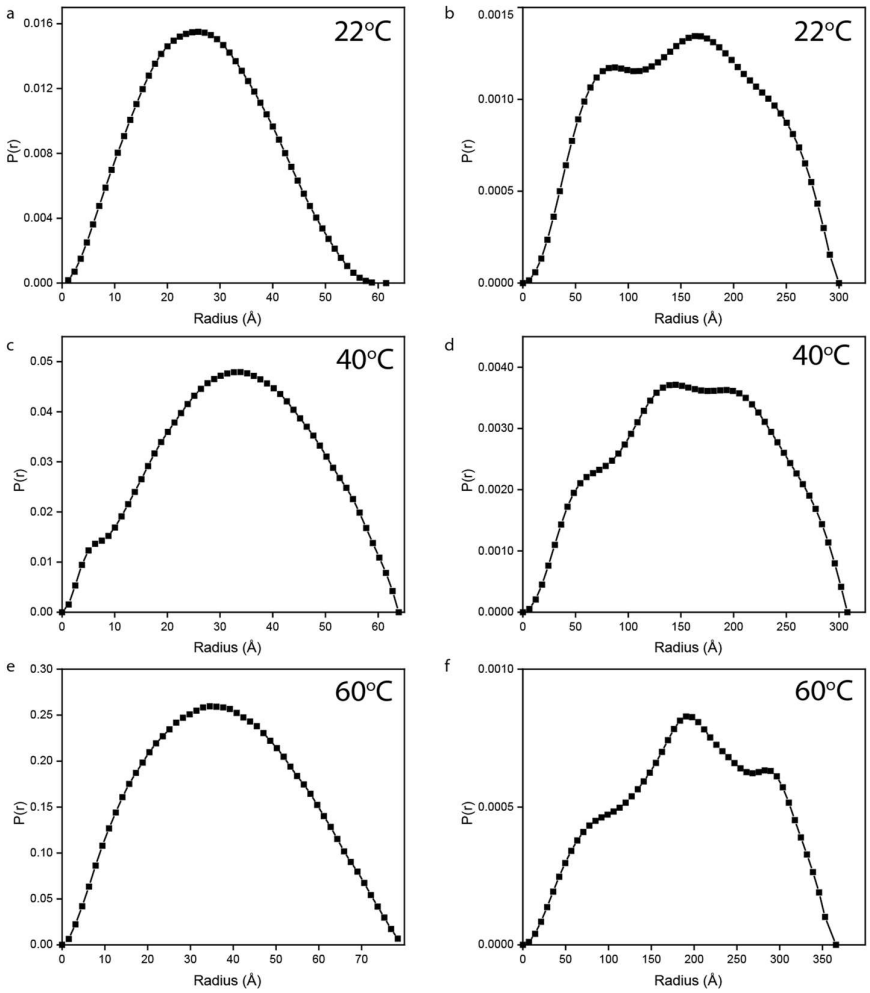

Figure S5-13. SAXS curves show reduced symmetry with increased reaction time, as shown for (a, b) 22ºC, (c, d) 40ºC and (e, f) 60ºC reactions at times of 5 seconds (left) and 1100 seconds (right). The decrease in symmetry may indicate an increase in anisotropy of the particles.

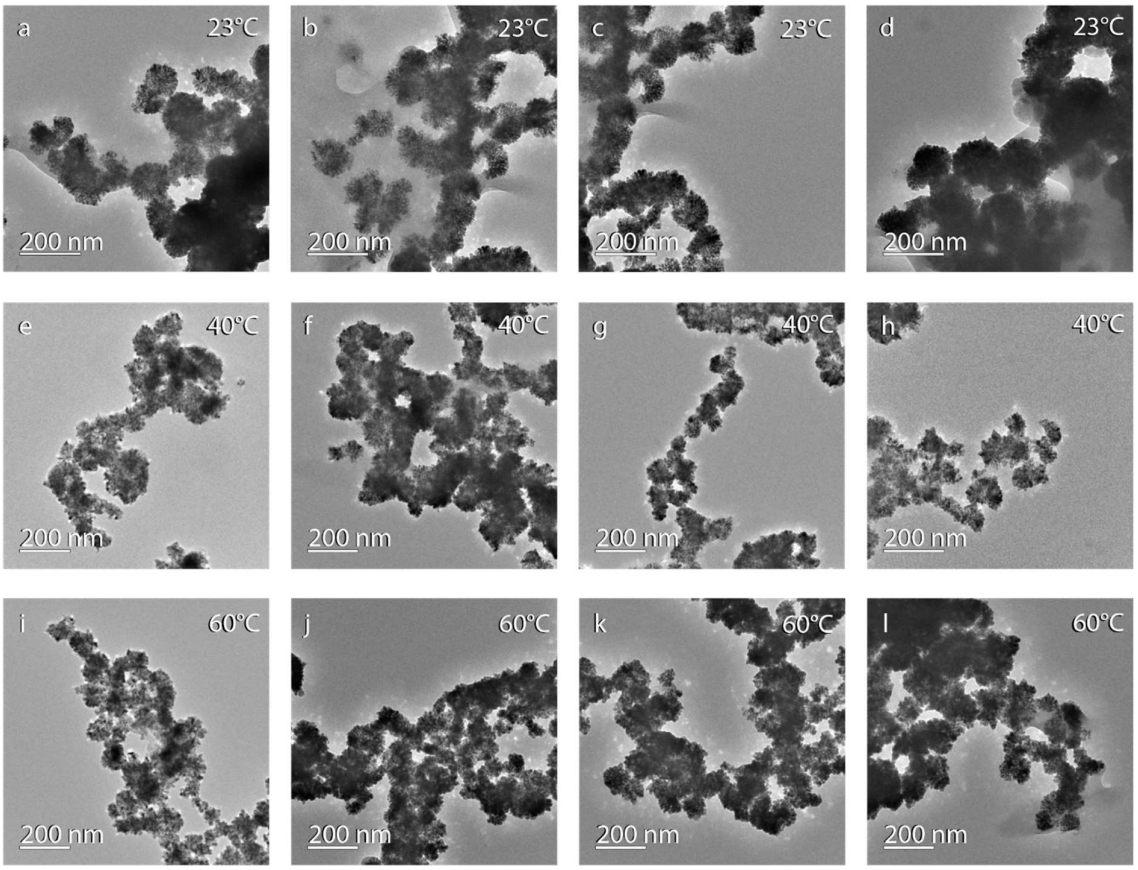

Figure S5-14. Sample of TEM images used to test the shapes and sizes, showing the nanoparticles formed at temperatures of (a) 23°C, (b) 40°C and (c) 60°C. Scalebar for all images measure 200 nm.

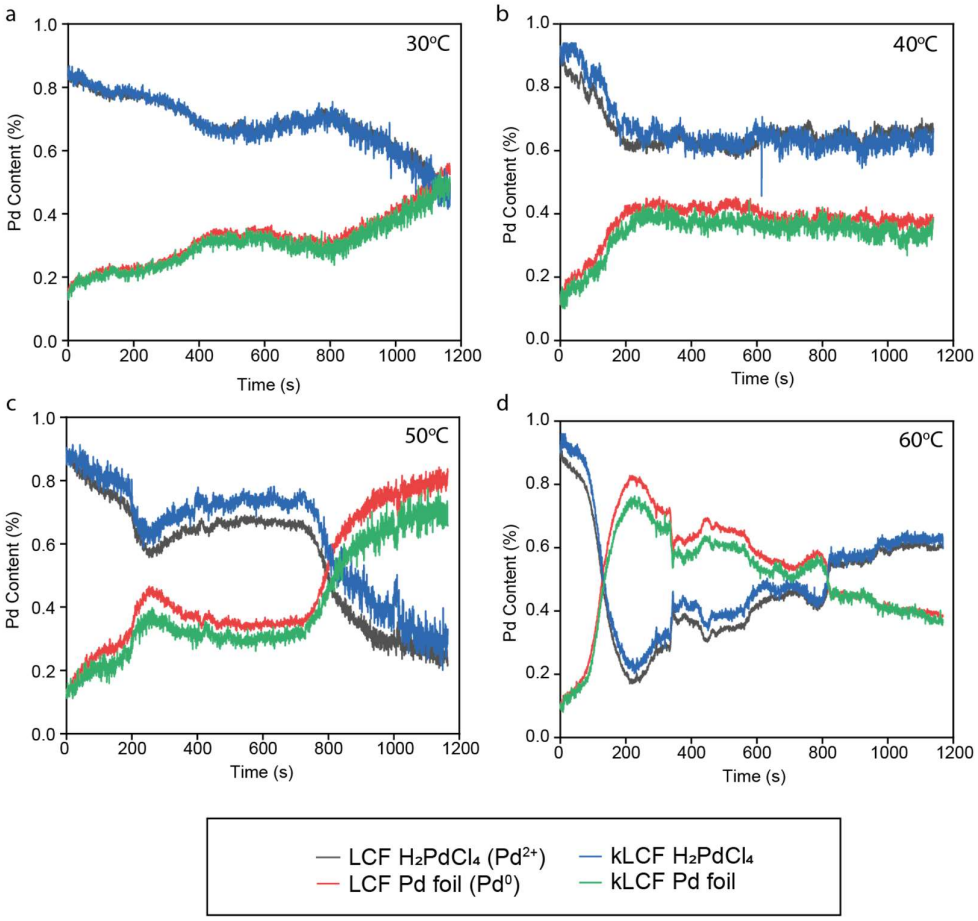

Figure S5-15. Linear combination fitting of the Pd K-edge XANES showing Pd^{2+} in grey and Pd^{0} in red versus linear combination fitting of the k-space (EXAFS region, 0 to 10 $Å^{-1}$) showing Pd^{2+} in blue and Pd^{0} in green for temperatures of (a) 30ºC, (b) 40ºC, (c) 50ºC and (d) 60ºC.

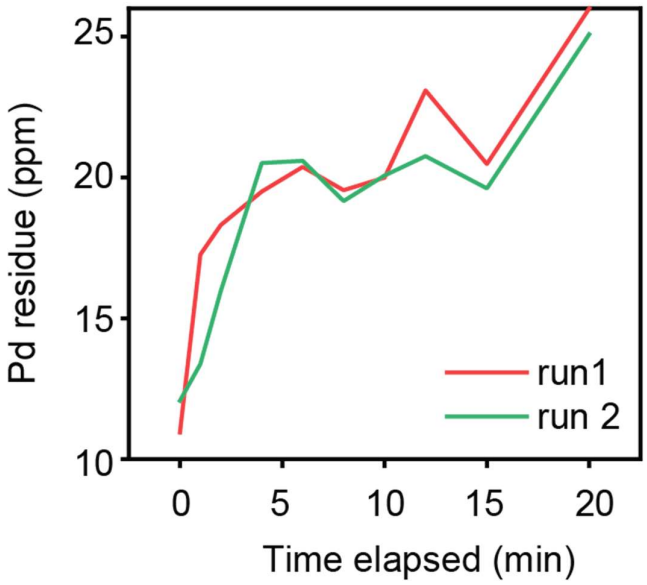

Figure S5-16. MP-AES readings of a time series measuring the solidified Pd0 residue at two minute intervals during Pd reduction at 50°C, matches the shape of the profile observed in oxidation state changes from XANES.

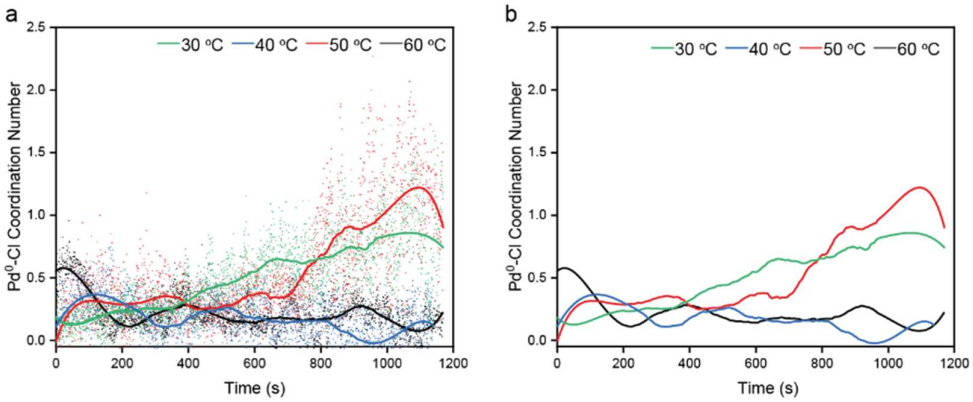

Figure S5-17. Calculated Pd^0-Cl coordination numbers calculated at 30ºC (green), 40ºC (blue), 50ºC (red) and 60ºC (grey), with (a) full data and best fit and (b) only best fit lines for improved visualisation.

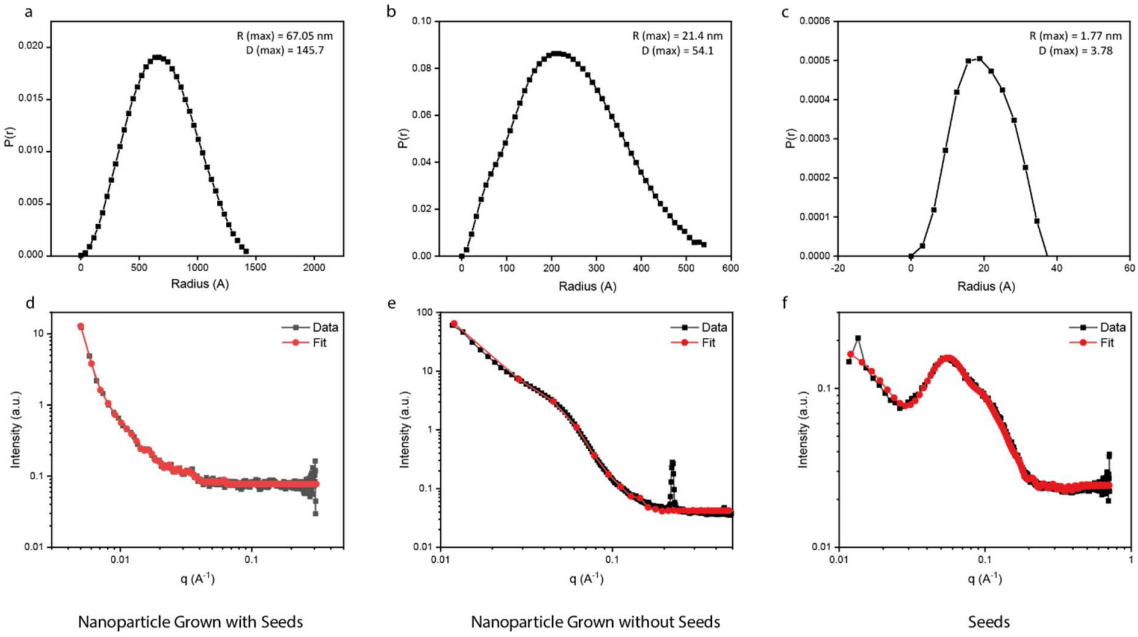

Figure S5-18. SAXS fitting results (red) alongside recorded data (black) of solutions containing (a, d) nanoparticles grown with seeds having a maximum diameter of 145.7 nm, (b, e) nanoparticles grown without seeds with a maximum diameter of 54.1 nm and (c, f) seed solution with maximum diameter of 3.78 nm.

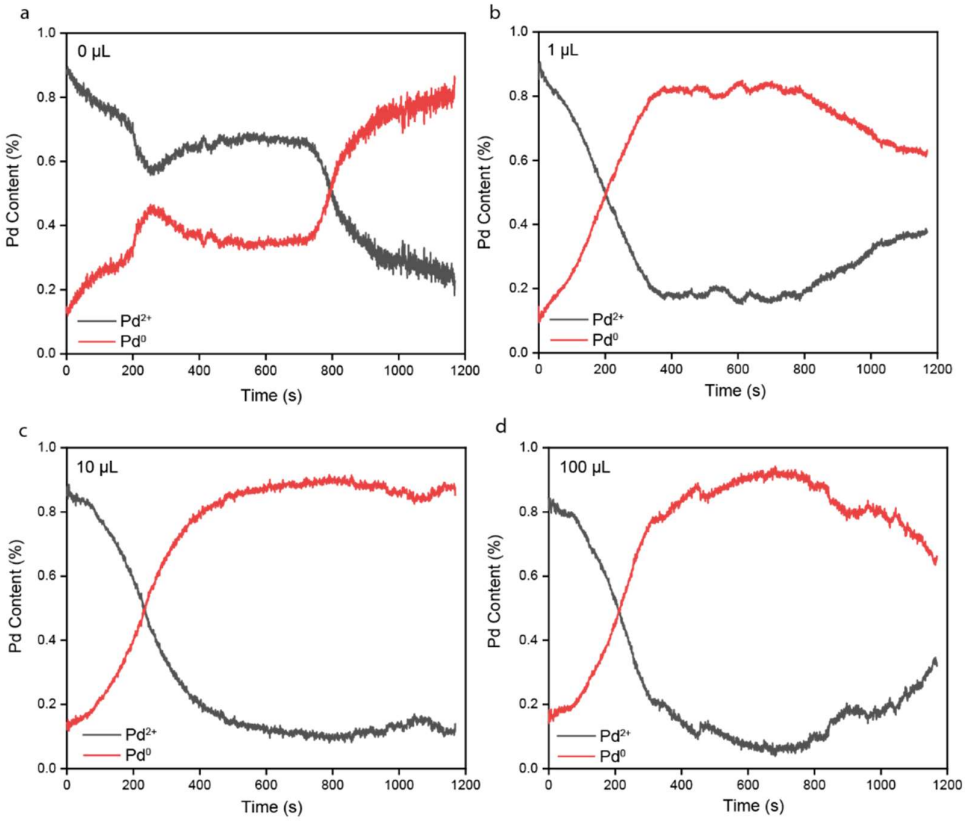

Figure S5-19. Linear combination fitting of the Pd K-edge XANES (LCF) with Pd^{2+} content shown in grey and Pd^{0} content in red, for seeded solutions with seed concentrations of (a) 0 µL, (b) 1 µL, (c) 10 µL and (d) 100 µL at 50ºC. Standards for Pd^{2+} and Pd^{0} were fresh H_2PdCl_4 solution in water and Pd foil, respectively.

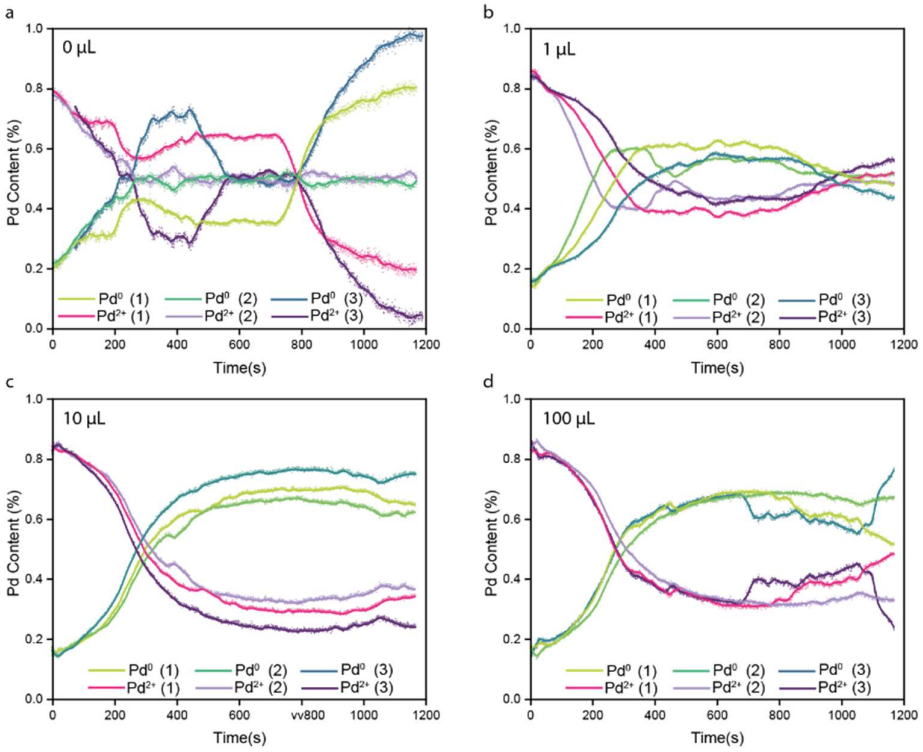

Figure S5-20. Linear combination fitting of the XANES (LCF) reproduced for three trials for seeded solutions with seed concentrations of (a) 0 µL, (b) 1 µL, (c) 10 µL and (d) 100 µL at 50ºC.

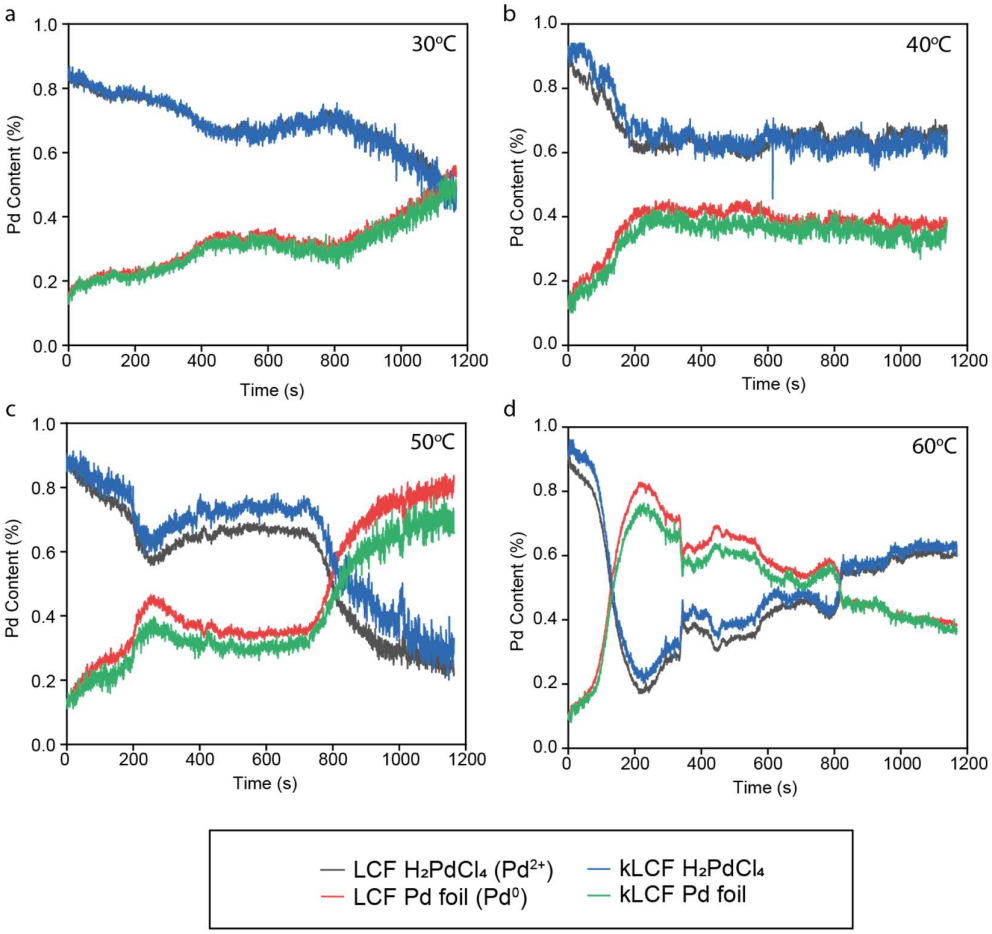

Figure S5-21. Linear combination fitting of the Pd K-edge XANES (LCF) versus linear combination fitting of the k-space of EXAFS region, 0 to 10 $Å^{-1}$ (kLCF) for seeded solutions with seed concentrations of (a) 0 µL, (b) 1 µL, (c) 10 µL and (d) 100 µL at 50ºC.

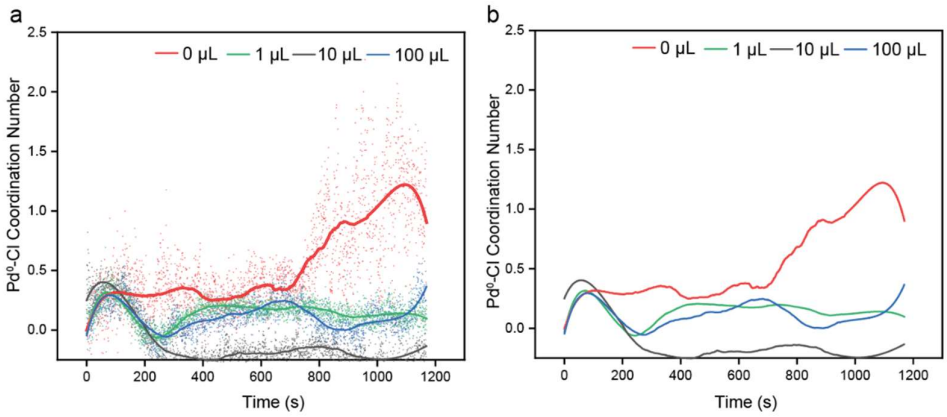

Figure S4-22. Calculated Pd^0-Cl coordination numbers calculated for 0 µL (green), 1 µL (blue), 10 µL (red) and 100 µL (grey), with (a) full data and best fit and (b) only best fit lines for improved visualisation.

5.5.4 Supplementary Tables

Table S5-1. Nanoparticles size measured from TEM images using ImageJ, for at least 140 particles, with measured diameter and radius in nanometers (nm).

Condition	Particles Measured	Diameter (nm)	Standard Deviation (nm)	Radius (nm)	Standard Deviation (nm)
50ºC, 1 min	2215	5.747	1.299	2.874	0.650
20ºC, 20 min	144	105.353	25.957	52.677	12.979
40ºC, 20 min	553	82.505	21.019	41.252	10.509
60ºC, 20min	444	76.970	19.627	38.485	9.814

Table S5-2. Fitting results Pd K-edge LCF fittings performed in Athena, using H_2PdCl_4 solution as Pd^{2+} standard and Pd foil as Pd^0 standard for the series of temperature conditions.

Temperature Condition (ºC)	Reaction Time (s)	R-factor	Weight Pd^{2+}	Pd^{2+} Error	Weight Pd^0	Pd^0 Error
30	5	0.0014	0.734	0.020	0.265	0.020
	100	0.0020	0.670	0.024	0.329	0.024
	600	0.0009	0.614	0.016	0.385	0.016
	1100	0.0005	0.559	0.012	0.440	0.013
40	0	0.0110	0.746	0.059	0.254	0.059
	100	0.0138	0.689	0.066	0.311	0.066
	600	0.0134	0.595	0.064	0.405	0.064
	1100	0.0169	0.677	0.073	0.323	0.073
50	0	0.0040	0.737	0.034	0.262	0.049
	135	0.0117	0.666	0.060	0.333	0.070
	455	0.0045	0.612	0.036	0.387	0.051

	725	0.0042	0.603	0.035	0.396	0.050
	755	0.0050	0.541	0.038	0.458	0.052
	795	0.0083	0.421	0.048	0.578	0.060
	870	0.0124	0.266	0.058	0.733	0.068
	920	0.0117	0.241	0.056	0.758	0.066
60	5	0.0023	0.255	0.026	0.744	0.026
	55	0.0015	0.278	0.021	0.721	0.021
	95	0.0006	0.323	0.014	0.676	0.014
	145	0.0017	0.475	0.021	0.524	0.021
	185	0.0020	0.571	0.022	0.428	0.022
	230	0.0022	0.601	0.023	0.398	0.023
	400	0.0011	0.533	0.017	0.466	0.017
	700	0.0004	0.472	0.011	0.527	0.012
	1100	0.0010	0.391	0.018	0.608	0.017

Table S5-3. Fitting results of Pd K-edge LCF Artemis, where amplitude reduction factor is set at 0.667. Common values of σ^2 were used, calculated as σ^2(Cl) is 0.002, σ^2(Pd) is 0.0037 and σ^2(O) is 0.002.

ºC	Time (s)	E_0	Pd-Pd CN	Pd-Cl CN	Pd-O CN	ΔR Pd-Pd	ΔR Pd-Cl	ΔR Pd-O
30ºC	5	4.47	0.62	4.01	1.39	-0.013	0.003	0.012
	Error	*2.74*	*0.57*	*0.69*	*1.20*	-	*0.020*	-
	100	3.68	0.99	3.88	1.18	-0.013	-0.001	0.013
	Error	*2.07*	*0.38*	*0.51*	*0.92*	-	*0.015*	-
	600	0.77	2.07	3.17	0.76	-0.013	-0.014	-0.049
	Error	*1.31*	*0.39*	*0.35*	*0.63*	-	*0.021*	-
	1100	0.49	3.84	2.39	1.10	-0.008	-0.008	-0.061
	Error	*0.65*	*0.40*	*0.30*	*0.42*	-	*0.008*	-
40ºC	0	0.47	0.83	3.26	2.40	-0.04	0.02	0.04
	Error	*1.76*	*0.41*	*0.44*	*0.79*	*0.04*	*0.01*	*0.04*
	100	-2.11	1.25	3.19	1.88	-0.01	100	-2.11
	Error	*1.78*	*0.33*	*0.45*	*0.84*	-	*0.01*	-
	600	1.96	3.46	2.92	0.83	0.00	-0.02	-0.02
	Error	*0.82*	*0.34*	*0.27*	*0.48*	*0.004*	*0.007*	-
	1100	1.96	3.32	2.70	1.27	-0.001	-0.02	-0.007
	Error	*1.41*	*0.52*	*0.45*	*0.83*	-	*0.013*	-
50ºC	0	5.16	1.25	2.76	2.18	-0.013	0.001	0.013
	Error	*1.36*	*0.40*	*0.31*	*0.51*	-	*0.011*	-
	135	4.10	1.97	3.16	1.80	-0.013	-0.023	0.013
	Error	*2.13*	*0.45*	*0.53*	*0.90*	-	*0.016*	-
	455	3.10	3.14	2.96	1.29	-0.013	-0.028	0.013
	Error	*1.27*	*1.07*	*0.43*	*0.72*	-	*0.010*	-
	725	1.87	3.16	2.98	0.85	-0.013	-0.033	0.013

	Error	*0.99*	*0.89*	*0.31*	*0.52*	-	*0.008*	-
	755	0.14	3.95	3.02	0.96	-0.013	-0.031	0.013
	Error	*1.08*	*0.44*	*0.38*	*0.67*	-	*0.009*	-
	795	2.18	5.54	2.23	1.49	-0.013	-0.036	0.013
	Error	*1.4*	*2.06*	*0.67*	*1.06*	-	*0.018*	-
	870	3.70	6.52	1.51	1.86	-0.013	-0.024	0.013
	Error	*2.02*	*0.73*	*0.57*	*0.98*	-	*0.028*	-
	920	2.54	7.10	1.45	1.81	-0.013	-0.025	0.013
	Error	*1.97*	*0.84*	*0.61*	*1.04*	-	*0.031*	-
60ºC	5	2.22	0.26	4.73	-	-0.043	-0.015	-
	Error	*1.62*	*0.41*	*0.30*	-	*0.086*	*0.010*	-
	55	1.61	0.78	4.54	-	-0.015	-0.017	-
	Error	*1.39*	*0.37*	*0.26*	-	*0.027*	*0.009*	-
	95	1.06	1.67	3.97	-	-0.014	-0.024	-
	Error	*1.36*	*0.34*	*0.24*	-	*0.014*	*0.009*	-
	145	-1.91	4.88	2.16	-	-0.019	-0.052	-
	Error	*1.57*	*0.42*	*0.31*	-	*0.009*	*0.016*	-
	185	-2.40	8.26	1.35	-	-0.019	-0.061	-
	Error	*1.33*	*1.64*	*0.37*	-	*0.008*	*0.023*	-
	230	-1.41	6.51	1.44	-	-0.019	-0.060	-
	Error	*1.43*	*0.45*	*0.33*	-	*0.007*	*0.022*	-
	400	-1.75	4.86	2.33	-	-0.017	-0.039	-
	Error	*0.86*	*0.24*	*0.18*	-	*0.005*	*0.008*	-
	700	-1.45	4.69	2.56	-	-0.015	-0.037	-
	Error	*1.20*	*1.04*	*0.27*	-	*0.008*	*0.011*	-
	1100	-0.35	3.41	3.28	-	-0.011	-0.029	-
	Error	*1.33*	*1.06*	*0.28*	-	*0.009*	*0.010*	-

Table S5-4. Activation energy calculation values of inverse temperature and reaction rates for the Arrhenius plot, alongside the error values measured.

Temperature Condition (ºC)	1/T (K^{-1})	Reaction Rate, k ($M^{-1}.s^{-1}$)	k Error
30	0.00330	-16.22	0.38
40	0.00319	-20.66	0.45
50	0.00310	-26.65	0.39
60	0.00300	-38.50	0.89

Table S5-5. SAXS fittings measured radius and diameter of the plateaued region in Figure S12 under different temperature conditions of 22ºC, 40ºC and 60ºC.

Condition	Reaction Time (s)	Diameter (nm)	Standard Deviation (nm)	Radius (nm)	Standard Deviation (nm)
22ºC, 20 min	840	34.4	1.462	17.2	0.731
40ºC, 20 min	696	36.4	1.432	18.2	0.716
60ºC, 20min	480	38.6	1.328	19.3	0.664

Table S5-6. Pd^0-Cl calculated percentage and the minimum concentration values in solution for temperature series and seed concentration series.

Condition	Max. Pd^0-Cl %	Approximated concentration of Pd^0-Cl (mM) [Min.]
60°C	21.39	6.72
50°C	32.84	10.31
40°C	12.00	3.768
30°C	20.54	6.45
1 μL seeds	15.38	4.83
10 μL seeds	18.24	5.73
100 μL seeds	12.89	4.05

Table S5-7. Pd K-edge EXAFS fitting of Pd seeds loaded on carbon after growth. Artemis fitting was performed using amplitude reduction factor of 0.815, as measured for a Pd foil standard. Low Pd-Pd coordination number of 0.35 indicates that the small nanoparticle size is maintained and the Pd-Cl and Pd-O coordination represent the surfaces exposed to Cl ligands and air.

Parameter	Value	Error
E_0	3.64	1.19
Pd-Pd	0.35	0.21
Pd-Cl	2.52	0.14
Pd-O	1.22	0.22
ΔR(Pd)	-0.014	0.034
ΔR(Cl)	-0.003	0.008
ΔR(O)	0.004	0.021
σ^2(Pd)	0.005	
σ^2(Cl)	0.002	
σ^2(O)	0.002	

List of Figures